

ABSTRACT

Title of Document: ENSEMBLE DATA ASSIMILATION AND BREEDING IN THE OCEAN, CHESAPEAKE BAY, AND MARS

Matthew J. Hoffman, Doctor of Philosophy,
2009

Directed By: Professor Eugenia Kalnay
Department of Atmospheric and Oceanic Science
&
Professor James A. Carton
Department of Atmospheric and Oceanic Science

My dissertation focuses on studying instabilities of different time scales using breeding and data assimilation in the oceans, as well as the Martian atmosphere. The breeding method of Toth and Kalnay finds the perturbations that grow naturally in a dynamical system like the atmosphere or the ocean. Here breeding is applied to a global ocean model forced by reanalysis winds in order to identify instabilities on weekly and monthly timescales. The method is extended to show how the energy equations for the bred vectors can be derived with only very minimal approximations and used to assess the physical mechanisms that give rise to the instabilities. Tropical Instability Waves in the tropical Pacific are diagnosed, confirming the existence of bands of both baroclinic and barotropic energy conversions indicated by earlier studies.

For regional prediction of smaller timescale phenomena, an advanced data assimilation system has been developed for the Chesapeake Bay Forecast System, a regional Earth System Prediction model. To accomplish this, the Regional Ocean Modeling System (ROMS) implementation on the Chesapeake Bay has been interfaced with the Local Ensemble Transform Kalman Filter (LETKF). The LETKF is among the most advanced data assimilation methods and is very effective for large, non-linear dynamical systems in both sparse and dense data coverage situations. In perfect model experiments using ChesROMS, the filter converges quickly and reduces the analysis and subsequent forecast errors in the temperature, salinity, and velocity fields. This error reduction has proved fairly robust to sensitivity studies such as reduced data coverage and realistic data coverage experiments. The LETKF also provides a method for error estimation and facilitates the investigation of the spatial distribution of the error. This information has been used to determine areas where more monitoring is needed.

The LETKF framework is also applied here to a global model of the Martian atmosphere. Sensitivity experiments are performed to determine the dependence of the assimilation on observational data. Observations of temperature are simulated at realistic vertical and horizontal levels and LETKF performance is evaluated. Martian instabilities that impact the assimilation are also addressed.

ENSEMBLE DATA ASSIMILATION AND BREEDING IN THE OCEAN,
CHESAPEAKE BAY, AND MARS

By

Matthew J. Hoffman

Dissertation submitted to the Faculty of the Graduate School of the
University of Maryland, College Park, in partial fulfillment
of the requirements for the degree of
Doctor of Philosophy
2009

Advisory Committee:
Professor Eugenia Kalnay, Chair/Co-Advisor
Professor James A. Carton, Co-Advisor
Professor Raghu Murtugudde
Professor Brian Hunt
Assistant Professor Kayo Ide
Professor Michael Evans, Dean's Representative

© Copyright by
Matthew J. Hoffman
2009

Acknowledgements

There are a great many people to whom I owe thanks for their encouragement, support, insight, and much needed distraction along the way. First, I would like to thank the members of my family. I thank my fiancée, Caitlin, for helping keep me sane over the past few years (and especially the past few months). She is always able to make me smile, even after a long day spent shaking my fist at my computer. I thank my parents, Marian and Brent, for all twenty-six plus years of love and support that they have given me and for all the sacrifices that they made to help put me through my seemingly unending schooling. I would be nowhere without them. I would also like to thank my brother Will for always making me laugh with his witty remarks and for his commiserations about graduate school. I would like to dedicate this dissertation to my grandfather, Bernard Rubenstein. He was one of my greatest supporters and nobody would have been more proud of me for writing this document.

I am eternally grateful to my advisors, Professor Eugenia Kalnay and Professor James A. Carton, for affording me the opportunity to do exciting, relevant, and novel research. When I arrived at Maryland I had never taken a course in Atmospheric and Oceanic Science, so for this to be the application area of my dissertation is a testament to the amount I have learned (and continue to learn) from them. I would like to thank Eugenia for always looking after me, always encouraging me, and always sharing her brilliant ideas. I thank Jim for his patience in teaching me oceanography, his constant support, and his insight. I would like to thank Professor Raghu Murtugudde for supporting me on the Chesapeake Bay project and for always pushing me to think independently. Thanks also to Brian Hunt, Kayo Ide, and

Michael Evans for their suggestions as well as for reading my dissertation and serving on my committee.

I would like to thank Ross Hoffman for generously providing LETKF code modified for a coastal ocean model. Thanks to Wen Long, and Jiantao Xu for providing the ChesROMS model and gridded forcing fields. Thanks also to Gyorgyi Gyarmati for preparing the Mars GCM. I would like to acknowledge Shu-Chih Yang, Eric Kostelich, Istvan Szunyogh, Christopher Brown, Chris Danforth, Elana Klein, Takemasa Miyoshi, Steven Greybush, Steven Penny, Hong Li, Ji-Sun Kang, John Wilson, and Junjie Liu for all of their ideas, input, and coding help. I am grateful to Konstantina Trivisa, Alverda McCoy, and David Levermore, in the AMSC program, for guiding me into and through the program. I also acknowledge Anita Dahlms, Haydee Hidalgo, Sonya Junek, and Celeste Regalado for always making sure I was on top of every deadline. Thanks also to James Crawford, Mark Baith, and David Yanuk for their much appreciated technological help.

I thank Russell Halper for being a great roommate and providing support and someone to complain to throughout all the difficulties of research. I also thank Nicholas Long, Jane Long, Juliana Belding, Elizabeth McLaughin, Kevin Wilson, and Emily Becker for their friendship and for providing much needed distractions from graduate school.

I would like to thank Michael Needham and Jeffrey Nelson for helping me stay sane during qualifying exams. I would also like to thank Daniel Barrie, Zahra Chaudry, Mellanie Follette, Megan Linkin, Lisa Murphy, and Edward Nowotnick for

their friendship, lunchtime conversation, and meteorological help. In addition, I wish to thank my Brazilian colleagues, Luciano Pezzi and Dirceu Herdies.

Table of Contents

Acknowledgements.....	ii
List of Tables	vii
List of Figures.....	viii
Chapter 1: Introduction.....	1
Introduction.....	1
The Breeding Method.....	2
Data Assimilation.....	4
Introduction.....	4
The Local Ensemble Transform Kalman Filter	6
Chapter 2: Use of Breeding to Detect and Explain Instabilities in the Global Ocean	15
Abstract.....	15
Motivation.....	15
The MOM2 Model.....	18
Bred Vector Energy Equations	18
Overview.....	18
Derivation of Bred Vector Kinetic Energy Equation.....	20
Derivation of Bred Vector Potential Energy Equation	23
Breeding in the Global Ocean.....	26
Experiment Setup.....	26
Pacific Tropical Instabilities	27
Atlantic Tropical Instabilities	29
South Atlantic Instabilities.....	31
Summary.....	32
Chapter 3: An Advanced Data Assimilation System for the Chesapeake Bay.....	44
Abstract.....	44
Introduction.....	44
The Model.....	49
LETKF Code Setup.....	51
Identical Twin Experiments.....	51
Experiments with 10% Data Coverage.....	51
Dependence on Data Coverage.....	52
Observation Targeting Using Ensemble Spread.....	52
Realistic Observation Distribution and the H Operator.....	56
Realistic Temporal Observation Distribution	59
Summary	62
Chapter 4: An LETKF Based Assimilation System for the Martian Atmosphere.....	86
Abstract.....	86
Introduction.....	86
NASA/NOAA Mars Global Circulation Model	90
Model Verification.....	91
LETKF Code Setup.....	91
Identical Twin Experiments.....	92

Full Coverage Experiments.....	92
Simulated TES Observations	96
Dependence on Localization.....	102
Summary	105
Chapter 5: Conclusion.....	130
Appendix: Global Ocean Data Assimilation.....	136
Introduction.....	136
MOM4 Model	136
Identical Twin Experiments	137
Bibliography	141

List of Tables

4.1 The localization parameters used at each vertical level of the MGCM for the full coverage observation experiment.....	93
4.2 The pressure levels of the TES vertical profiles and closest model levels.....	97
4.3 The localization parameters used at each vertical level of the MGCM for the simulated TES observation experiment.....	99
4.4 The localization parameters used at each vertical level of the MGCM for the simulated TES observation experiment with increased localization radius in the upper atmosphere.....	105

List of Figures

2.1 (a) The SST bred vector [C] on 5 April 1952, a time when there is relatively low activity from tropical instabilities. (b) The SST bred vector [C] on 21 December 1951, when Pacific tropical instabilities are visible.....	35
2.2 (a) Bred vector of zonal velocity on 11 November 1988, a time when the tropical Pacific was in a late developing La Niña with a Southern Oscillation Index of 21.0 and a Nino3.4 Index of -2°C . (b) The corresponding baroclinic energy conversion term. Baroclinic energy conversion contributes to the growth of bred vector kinetic energy along the Pacific equator. Off the coast of South America the baroclinic conversion term acts to convert bred vector kinetic to potential energy. The magnitudes of the fields are somewhat arbitrary due to the rescaling of the bred vectors, but the units are m/s for the velocity and $10^{-6} \text{ kg m}^{-1} \text{ s}^{-3}$ for the baroclinic energy conversion.....	36
2.3 Time-longitude diagram of the SST bred vector at 3.5°N latitude from June 1985 to December 1992.....	37
2.4 (a) The panels show the 30 year averages of the baroclinic (top panel) and barotropic (bottom panel) conversion terms for the month of January, during which barotropic energy has a peak and baroclinic energy is very strong. Positive conversion is shown in red while negative conversion is in blue. Although other months show the bred vector energy conversion occurring in different longitude regions, the January average of the conversion terms is shown here because it is representative of the shape and latitudinal location of the bred vector energy conversion. It is	

important to note that the sign and relative magnitude of the bred vector energy conversion terms indicate the shape, direction, and location of the energy conversion; however, the absolute magnitude of the energy conversion is not determined by this analysis. (b) The time series from June 1986 to December 1992 of the baroclinic (blue) and barotropic (red) conversion terms averaged between 180°W to 120°W longitude, -5°S to 5°N latitude, and between the surface and 150m depth. The energy conversion can be seen to increase in late summer and die off by May of the following year. In the La Niña year of 1988-1989, a significant increase in energy conversion occurs. The vertical axis has units $10^{-7} \text{ kg m}^{-1} \text{ s}^{-3}$38

2.5 Vertical profile of climatological October properties computed from the 30 year monthly average. (a) The baroclinic conversion term (shaded) and temperature (contours) with latitude between 180° to 110°W, and (b) the barotropic conversion term (shaded) and zonal velocity (contours) with longitude at 0.65°N. Both the baroclinic and barotropic terms have units $10^{-6} \text{ kg m}^{-1} \text{ s}^{-3}$. Baroclinic conversion from potential to kinetic bred perturbation energy occurs above the thermocline with maximum at the latitude of coldest SST. This area of coldest SST (top center of (a)) corresponds to the Pacific cold tongue. The maximum barotropic conversion from the background kinetic energy to the bred perturbation occurs along the shear zone between the westward South Equatorial Current and eastward Equatorial Undercurrent. The October average is shown here because it is qualitatively representative of the location and pattern of the relative amplitude of the conversion during fall and winter months.....39

2.6 The vertically averaged baroclinic conversion term (shaded) and vertically averaged current vectors in the equatorial Atlantic from 8°S to 8°N and 45°W to 10°W. All values are $10^{-7} \text{ kg m}^{-1} \text{ s}^{-3}$	40
2.7 a) Vertical profile of the monthly averaged temperature in July from 1951 to 1979 (contour) overlaid on the averaged baroclinic conversion term (contour) in the equatorial Atlantic at 0.65°N and between 50°W to 10°W. The majority of the baroclinic conversion is taking place along the thermocline. (b) Vertical profile of the monthly averaged zonal velocity in July from 1951 to 1979 (contour) overlaid on the averaged barotropic conversion term (shaded) in the same region.....	41
2.8 The vertically averaged barotropic conversion term (shaded) and vertically averaged current vectors in the equatorial Atlantic from 8°S to 8°N and 45°W to 10°W. All values are $10^{-8} \text{ kg m}^{-1} \text{ s}^{-3}$	42
2.9 (a) The surface baroclinic conversion term on 11 November 1988 in the Western South Atlantic Ocean off the coast of South America. (b) The vertical profile of the barotropic conversion term (shaded) [$10^{-9} \text{ kg m}^{-1} \text{ s}^{-3}$] at 40°S on 11 November 1988 overlaid with the zonal velocity [cm/s] (contour) in the same region.....	43
3.1 Model bathymetry in meters along with the names of major rivers.....	65
3.2 Global RMS temperature error [C] from 10 January to 9 February 1999 (a) from an identical twin experiment using 10% observational data coverage and 9% inflation and (b) with varying data coverage in identical twin experiments using 9% inflation and a 16 member ensemble.....	66
3.3 (a) SST ensemble spread on 20 January 1999 during a spike in global temperature RMS error (see Fig. 3.1) caused by an event where surface winds are	

pointing into the Bay and pushing warm water up the mouth of the Bay. (b) Forecast error on 20 January 1999. Note that the error in the lower Bay is captured by the ensemble spread in **Fig. 3.3a**, but the magnitude of the spread is several times smaller than the error.....67

3.4 Comparison of global temperature analysis RMS error during the RMS error spike from 23 January 1999 and 26 January 1999 between an experiment using a single observation taken at the maximum SST spread and one without that extra observation. Both simulations have 0.5% data coverage and 2% inflation used throughout. The analysis is uniformly better in temperature over the entire run, but is particularly improved during the times when the RMS error is spiking due to a response to surface forcing.....68

3.5 Average ensemble spread in SST during January, April, July, and October 1999 for experiments using 2% inflation, a 16 member ensemble, and 0.5% data coverage.....69

3.6 Average ensemble spread in surface salinity during January, April, July, and October 1999 for experiments using 2% inflation, a 16 member ensemble, and 0.5% data coverage.....70

3.7 Number of observations in temperature from CBOS and the CBP during each 6-hour analysis window between 10 January 1999 and 14 February 1999. The same number of CBOS observations is present at every analysis window, so spikes in the number of observations are due to an influx of CBP data.....71

3.8	Locations of CBOS (stars) and CBP (*) observation stations in the Chesapeake Bay are shown in black. The analysis error in SST after the first analysis using only temperature and salinity observations at the surface is shown in the background.....	72
3.9	Global RMS error in (a) temperature from 10 January to 17 January 1999 from an identical twin experiment using simulated observations of temperature and salinity at the surface at real station locations. (b) Global RMS error in salinity from the same experiment.....	73
3.10	Global RMS error in (a) the u current component from 10 January to 17 January 1999 from an identical twin experiment using simulated observations of temperature and salinity at the surface at real station locations. (b) Global RMS error in v current from the same experiment.....	74
3.11	(a) Ensemble spread in SST [C] on 12 February 1999, 32 days into the simulation using a 16 member ensemble, simulated observations at real locations and assimilation times, and 2% inflation. The horizontal localization used was uniformly 20 grid points. The ensemble can be seen to diverge in the open ocean. (b) Ensemble spread in SST [C] on 12 February 1999 from an experiment with the same parameters except for a larger localization. The localization is 60 grid points below the mouth of the Bay, 40 grid points for the rest of the open ocean, and 20 grid points for the rest of the Bay.....	75
3.12	Global RMS error in temperature for the analysis (blue), forecast (red), observations (green), and free run forecast (cyan) for an identical twin experiment using observations simulated at real assimilation times and locations. The experiment uses 12 ensemble members, 2% inflation, and temperature and salinity observations.	

The number of temperature observations is shown in the bar graph, which has the same information as **Fig. 3.7**.....76

3.13 Global RMS error in salinity for the analysis (blue), forecast (red), observations (green), and free run forecast (cyan) for an identical twin experiment using observations simulated at real assimilation times and locations. The experiment uses 12 ensemble members, 2% inflation, and temperature and salinity observations.....77

3.14 Number of observations in salinity from CBOS and the CBP during each 6-hour analysis window between 10 January 1999 and 14 February 1999. The same number of CBOS observations is present at every analysis window, so spikes in the number of observations are due to an influx of CBP data.....78

3.15 Free run forecast error in SST [C] at 1200 hours on 11 January 1999, 1 day into the simulation using observations simulated at real locations and analysis intervals, a 16 member ensemble, and 2% covariance inflation.....79

3.16 Analysis error in SST [C] at 1200 hours on 11 January 1999, 1 day into the simulation using observations simulated at real locations and analysis intervals, a 16 member ensemble, and 2% covariance inflation. The darkest blue areas have not yet been corrected by the LETKF.....80

3.17 Improvement of the analysis over the free run forecast, defined as the absolute value of the free run error minus the absolute value of the analysis error, in SST [C] at 1200 hours on 11 January 1999, 1 day into the simulation using observations simulated at real locations and analysis intervals, a 16 member ensemble, and 2% covariance inflation. Positive values (red) indicate areas where the analysis is

superior while negative values (blue) indicate that the analysis is less accurate than the free run forecast.....	81
3.18 Free run forecast error in SST [C] on 9 February 1999, 30 days into the simulation using observations simulated at real locations and analysis intervals, a 16 member ensemble, and 2% covariance inflation.....	82
3.19 Analysis error in SST [C] on 9 February 1999, 30 days into the simulation using observations simulated at real locations and analysis intervals, a 16 member ensemble, and 2% covariance inflation.....	83
3.20 Improvement of the analysis over the free run forecast, defined as the absolute value of the free run error minus the absolute value of the analysis error, in SST [C] on 9 February 1999, 30 days into the simulation using observations simulated at real locations and analysis intervals, a 16 member ensemble, and 2% covariance inflation. Positive values (red) indicate areas where the analysis is superior while negative values (blue) indicate that the analysis is less accurate than the free run forecast.....	84
3.21 Ensemble spread in SST [C] on 9 February 1999, 30 days into the simulation using observations simulated at real locations and analysis intervals, a 16 member ensemble, and 2% covariance inflation.....	85
4.1 The diurnal cycle of the MGCM at the surface (Level 28). Temperature [K] is shaded and the contours represent the Martian surface topography. A few of the major features—the Hellas Basin, Olympus Mons (the largest mountain in the solar system), the lowlands of the Vastitas Borealis, and the volcanic Tharsis plateau—are labeled (top right). Courtesy of S. Greybush.....	108

4.2 (a) The northern summer zonal mean of zonal wind shows a strong wind jet in the southern (winter) hemisphere. (b) The northern winter zonal mean of zonal wind shows a strong wind jet in the northern (winter) hemisphere. Courtesy of S. Greybush.....109

4.3 Left: TES surface temperature retrievals (K) along a few orbits corresponding to 0.25 sols. Right: TES temperature profile retrievals with the horizontal axis representing observation numbers along the orbital path. Deep red areas represent levels that are below the surface. Courtesy of S. Greybush.....109

4.4 The mean of the initial ensemble surface temperature forecast (top left) has significant errors (top right), compared to the truth. The analysis ensemble mean after one step (bottom left), however, is very close to the truth and the errors almost do not show up on the same scale (bottom right).....110

4.5 (a) The global RMS error in temperature from an identical twin experiment using observations at every grid point with observation error of 1K, a 1200km horizontal localization radius, and 10% inflation. (b) The global RMS error in zonal wind of the same experiment. The analysis and forecast are improved even though no wind observations are assimilated.....111

4.6 Left: The temperature and zonal component of the wind vector field at model level 25 [m/s]. Right: The temperature and zonal component of the wind vector field at model level 5 [m/s].....112

4.7 (a) Time evolution of the root-mean-square error in the estimates of the temperature [K] by the free model run and the cycled data assimilation of temperature observations at model level 25. (b) Time evolution of the root-mean-square error in

the estimates of the temperature [K] by the free model run and the cycled data assimilation of temperature observations at model level 5.....	113
4.8 The ensemble spread by vertical level over a 50 sol simulation using 1K observation error, 10% inflation, 16 ensemble members, and full coverage observations.....	114
4.9 The time averaged analysis error [K] (contour) and truth temperature field [K] (shaded) at model level 17 using observations at every grid point with 1K observation error, 10% inflation, and 16 ensemble members.....	115
4.10 Vertical profile of the time averaged analysis error [K] (contour) and truth temperature field [K] (shaded) using observations at every grid point with 1K observation error, 10% inflation, and 16 ensemble members. The vertical axis is pressure in mb.....	116
4.11 (a) Background error [K] (shaded) and background spread in temperature [K] (contour) averaged over the period from sol 2 of the simulation to sol 31 at model level 25 using observations at every grid point with 1K observation error, 10% inflation, and 16 ensemble members. (b) Analysis error (shaded) and analysis spread (contour).....	117
4.12 Comparison of the global RMS error in temperature using observations at every grid point and observations at simulated TES locations both only horizontally and both horizontally and vertically. A 1200km horizontal localization radius is used with an observation error of 1K and 10% inflation.....	118
4.13 Comparison of the global RMS error in zonal wind using observations at every grid point and observations at simulated TES locations both only horizontally and	

both horizontally and vertically. A 1200km horizontal localization radius is used with an observation error of 1K and 10% inflation.....	119
4.14 (a) Comparison of the analysis temperature RMS error from the free run, assimilation using simulated TES observations with 3K error, and assimilation using simulated TES observation with 1K observation error. (b) Comparison in zonal wind.....	120
4.15 Temperature RMS error from an experiment using simulated TES observations with 3K error, 10% inflation, and a 16 member ensemble in (a) level 5 (b) level 25.....	121
.16 Zonal wind RMS error from an experiment using simulated TES observations with 3K error, 10% inflation, and a 16 member ensemble in (a) level 5 (b) level 25.....	122
4.17 Vertical profile of the time averaged analysis error [K] (contour) and truth temperature field [K] (shaded) using simulated TES observations with 3K observation error, 10% inflation, and 16 ensemble members. The vertical axis is pressure in mb.....	123
4.18 Error in the free run forecast in level 25 (top left) and level 5 (top right) and the analysis in level 25 (bottom left) and level 5 (bottom right) from sol 2, hour 6 of an experiment using simulated TES observations with error 3K, 16 ensemble members, and 10% inflation.....	124
4.19 (a) The analysis error (shaded) in temperature [K] after the first analysis in level 25 of the model using simulated TES observations at all vertical levels and a 1200km	

localization. The contour shows the observation track. (b) The same figure but with a 2500km localization radius.....	125
4.20 The ensemble correlation to the point (30,18,25) averaged over the final 48 sols of a 50 sol assimilation run. The correlation at level 25 (7.39mb) is shown at the top left, a cross section along $x=30$ is shown top right, and a cross section along the equator is show bottom right. The vertical axis for the cross section is pressure in mb.....	126
4.21 The ensemble correlation to the point (30,18,15) averaged over the final 48 sols of a 50 sol assimilation run. The correlation at level 15 (2.50mb) is shown at the top left, a cross section along $x=30$ is shown top right, and a cross section along the equator is show bottom right. The vertical axis for the cross section is pressure in mb.....	127
4.22 The ensemble correlation to the point (30,18,5) averaged over the final 48 sols of a 50 sol assimilation run. The correlation at level 5 (0.026mb) is shown at the top left, a cross section along $x=30$ is shown top right, and a cross section along the equator is show bottom right. The vertical axis for the cross section is pressure in mb.....	128
4.23 From an experiment using simulated TES observations with 3K error, 10% inflation, a 16 member ensemble, and larger horizontal localization in the upper atmosphere, (a) the global temperature RMS error (b) Global zonal wind RMS error.....	129

A.1 Meridional velocity at Brazil-Malvinas Confluence. Panels showing the Background state, Analysis and Truth from 8 members simulations. All simulations refer to a climatological January.....139

A.2 Meridional velocity at Brazil-Malvinas Confluence. Panels showing the Background state, Analysis and Truth from 12 members simulations. All simulations refer to a climatological January.....140

Chapter 1: Introduction

Introduction

Mathematically, forecasting the behavior of a physical system is an initial value problem which requires a numerical model approximation of the system and an estimate of the current system state. For a complex, chaotic system, such as the ocean and the atmosphere, errors in the initial state estimate are amplified by instabilities in the system, eventually causing a significant decrease in forecast skill. To accurately forecast a complex system, it is important to understand the timescales and dynamical causes of these instabilities and to be able to correct the resulting errors. One method of addressing this issue is to use a number of slightly different initial states and follow their trajectories. The resulting difference between the ensemble members describes the uncertainty in the forecast. The breeding method utilizes the difference between model runs beginning from slightly different initial conditions to identify and isolate instabilities of different timescales. Ensemble Kalman filter methods use the difference between members of an ensemble to estimate the forecast uncertainty.

This dissertation explores breeding and data assimilation over different dynamical systems. Chapter 2 presents a new method of computing energetics using breeding and then applies this method to the study of instabilities in the global ocean. Bred vector energy equations are used to address the question of what are the main dynamical causes of Tropical Instability Waves in the tropical Pacific and Atlantic Oceans as well as an instability in the South Atlantic off the coast of South America.

Data assimilation in the Chesapeake Bay using the Local Ensemble Transform Kalman Filter (LETKF) is studied in Chapter 3. This chapter studies the feasibility of an ensemble Kalman filter system in the Chesapeake Bay and evaluates the current observational network for the purpose of assimilation. The LETKF is also applied to a Martian General Circulation Model in Chapter 4 and the predictability of the Martian atmosphere is addressed. The chapter addresses the question of whether the LETKF effectively improves the state estimate on the Martian atmosphere using a realistic satellite observation distribution. A discussion of the results and future research is presented in Chapter 5. An appendix presents preliminary results from an assimilation and forecast system in the global ocean.

Each chapter constitutes a separate project and the results from each are being written up in separate papers. A paper containing the main results from Chapter 2 has been accepted to GRL pending small revisions and papers on the Chesapeake Bay and Mars data assimilation projects are currently being written.

The Breeding Method

The breeding method was originally developed both for application to data assimilation (to identify the growing component of the analysis error (Yang et al., 2008)) and to provide a set of plausible initial conditions for ensemble forecasting of atmospheric motions representative of the growing errors in the analysis (Toth and Kalnay, 1993, 1997). Here the method is extended to provide an alternative method of computing the energetics of the global upper ocean which has advantages of being simple to implement and computationally inexpensive.

The breeding method begins with an arbitrary small perturbation of the initial state of an unstable system, such as the ocean, represented by a numerical model. This model is integrated forward for a time interval, Δt , beginning from both the perturbed and unperturbed (or control) initial state. The vector difference in ocean state variables between the two resulting nonlinear forecasts is called the bred vector. At Δt this bred vector is rescaled to the size of the initial perturbation and then is added to the control simulation to form the perturbed initial state for a new simulation. Examples of norms for rescaling are the root mean square difference of sea surface temperature (SST) or the kinetic energy of the perturbations. Twin simulations beginning with the control and newly perturbed control initial state at Δt are then integrated forward from Δt to $2\Delta t$ to create a new simulation pair. The bred vector at time $2\Delta t$ is then computed, rescaled, and the process is repeated. After a short spinup and when carried out over many cycles, the resulting time series of bred vectors has been shown by Toth and Kalnay to isolate and identify the components of the system that grow most rapidly on a time-scale of Δt or longer, and to separate them from other rapidly growing components that saturate in times shorter than Δt . By varying Δt (hereafter known as the "breeding interval"), Peña and Kalnay (2004) showed how to isolate instabilities of different temporal scales. The bred vectors created by this process are essentially non-linear generalizations of Lyapunov vectors and, like Lyapunov vectors, they are independent of the norm chosen for rescaling (Toth and Kalnay, 1997; Kalnay, 2004). Equivalent results can be obtained with any norm; however, given a norm, rescaling the BVs to different sizes as measured by that norm controls the degree of nonlinearity in the BV evolution. In addition, the

time interval can be chosen to select phenomena which have not reached error saturation in that interval. It is through tuning these two parameters that the breeding method can be used to isolate different types of instabilities (Peña and Kalnay, 2004; Chikamoto et al., 2007; Vikhliav et al., 2007).

Data Assimilation

Introduction

While data assimilation has been performed on ocean models and planetary models for many years, the schemes used have usually not been as sophisticated as those used on their atmospheric counterparts. Many ocean data assimilation efforts, including most of the operational systems have used some type of optimal interpolation (Mellor and Ezer, 1991; Fana et al., 2004). In the Chesapeake Bay, salinity data from a ship-towed vehicle was assimilated by Xu et al. (2002) using a nudging method. While some improvements were seen, it was also noted that the nudging method introduced errors from disrupting the system balance, something that advanced assimilation methods do a better job of preserving (Xu et al., 2002).

Recently, a number of global and coastal scale assimilation efforts have been undertaken using advanced methods (*e.g.*, Lermusiaux et al. 2006; R. Hoffman et al. 2008; Wunsch and Heimbach 2007). The majority of these systems utilize an assimilation system related to three or four dimensional variational (3D-Var and 4D-Var) methods (Wunsch and Heimbach 2007; Stammer et al. 2002), while a few have used ensemble Kalman filter methods (R. Hoffman et al., 2008; Fukumori, 2002).

Studies of the Martian atmosphere have used similar assimilation methods. Banfield et al. (1995), one of the earliest studies, assimilated simulated observations

using a Kalman filter approach with a fixed covariance matrix. Simulated observations were also used with the analysis correction scheme (Lewis and Read, 1995; Lewis et al., 1996, 1997). Houban (1999) assimilated real Thermal Emission Spectrometer (TES) temperature observations with a 4D-VAR scheme using an approximation of the tangent linear model. The assimilation run was very short, but some promising analyses of the zonal mean were shown. TES temperature observations were also assimilated by Zhang et al. (2001) using the steady state Kalman filter of Banfield (1995). Results from this study were mixed and there was not convincing evidence that the filter was converging sufficiently.

Data assimilation methods which focus on state estimation, such as most Kalman filter based methods, attempt to improve forecasts by improving the accuracy of the current state estimate (which is the initial condition) (Hunt, 2007, Houtekamer, 1998). In a data assimilation scheme, an estimate of the current state is derived by combining current observations and a previous forecast, which is referred to as the background. This state estimate, hereafter called the “analysis”, is then used as the initial condition for the model, which, in turn, creates a new forecast. Data assimilation proceeds in this manner, alternating between a forecast step, where the model predicts the future state of the system, and an analysis step, where observations taken at this future time are incorporated and the analysis is created.

Both the background and the observations have errors, and the analysis step consists of a statistical procedure that takes these errors into account in determining the analysis state. Since the estimate takes into account the observations and the background state, in addition to the relative covariances of each state, approximations

of the covariances must be derived. In most of the currently used data assimilation techniques, such as 3D-VAR and 4D-VAR, the background error covariance is assumed to be constant in time and is approximated using a climatological average. While this is a reasonable approximation, it does not account for the day-to-day variations in the background error covariance that naturally occur. In contrast, Ensemble Kalman Filters (EnKFs) estimate the background error covariance using the sample covariance of an ensemble of forecast states (Hunt, 2007, Houtekamer, 1998, Whitaker, 2002). One of the significant advantages of the ensemble methods over variational schemes is that ensemble methods account for "errors of the day" much more effectively by allowing the background error covariance to change at each step (Kalnay, 2003, Hunt, 2007).

The Local Ensemble Transform Kalman Filter

In this thesis the data assimilation framework of the Local Ensemble Transform Kalman Filter (Hunt et al., 2007) is utilized. Data assimilation in general, and the LETKF in particular, has a longer history in atmospheric science than in either oceanography or planetary science. Among the reasons that ocean and planetary data assimilation has lagged behind that of the atmosphere are that observational data is much more sparse and that weather prediction has a much larger daily human impact. With the advent of newer, more sophisticated, observing methods, however, the observational coverage of the ocean is increasing and along with it the potential gains in forecasting skill through effective and efficient data assimilation. Similarly, a new generation of Martian satellites in the 1990s has made

Martian data assimilation a promising tool for increasing our understanding of the Martian climate.

The central problem in oceanic and atmospheric modeling is the same in that both systems can be modeled through a set of partial differential equations. These equations, along with boundary values given by the current state of the system, form a well-defined initial value problem whose solution can be used to predict the state of the system at subsequent times. In practice, these equations will never be exact due to unavoidable errors in parameters such as friction or viscosity coefficients, as well as approximations made to facilitate computation. There will also always be errors in the estimation of the current state of the system due to instrumental errors, the lack of full observational coverage, and representativeness errors. Even if the equations and boundary conditions were exact, however, the chaotic nature of these systems means that even the inherent errors caused by discretizing the equations and solving them numerically would lead to large errors over a long forecast.

Despite the grim long term outlook, accurate forecasts can be made over reasonable time intervals and are very valuable. Improvements to forecasting skill can be made in a number of ways and serve to both improve the forecast on a particular day and to increase the length of usable forecasts. As discussed above, data assimilation methods, such as the LETKF, attempt to improve forecasts by improving the accuracy of the current state estimate. In the LETKF, this synthesis of background and observations is accomplished using a Bayesian maximum likelihood estimate. Before delving into the mechanics of the LETKF, however, it is necessary to

introduce both the notation used and the original Kalman filter, on which the LETKF is based.

The Kalman filter was first introduced in 1960-61 as a method for estimating the true state, denoted \mathbf{x}^t , of a dynamical system (Kalman, 1960; Kalman and Bucy, 1961). As described above, this method is a statistical procedure which combines observations, \mathbf{y}^o , with the background state estimate, \mathbf{x}^b , to create the analysis estimate, \mathbf{x}^a . Because the statistical estimate assumes that the background and the analysis have Gaussian and unbiased errors, \mathbf{x}^b and \mathbf{x}^a have corresponding covariance matrices \mathbf{P}^b and \mathbf{P}^a , respectively. In practice, there is never an observation taken at every grid point of the model nor is any individual observation exact. Thus we assume that $\mathbf{y}^o = H(\mathbf{x}^t) + \varepsilon$, where the operator H is the (possibly nonlinear) map from model space (which here is considered to be a discrete grid) to the observation space and the error term ε is a Gaussian random variable with covariance matrix \mathbf{R} . In practice, the linearization, \mathbf{H} , of the transformation H is frequently used to simplify the computation. For this reason, \mathbf{H} is used in place of H in the subsequent equations. The linear Kalman filter then creates the analysis and its corresponding covariance using the following equations:

$$\mathbf{x}^a = \mathbf{x}^b + \mathbf{K}(\mathbf{y}^o - \mathbf{H}\mathbf{x}^b) \quad (1.1)$$

$$\mathbf{P}^a = (\mathbf{I} - \mathbf{K}\mathbf{H})\mathbf{P}^b \quad (1.2)$$

where $\mathbf{K} = \mathbf{P}^b\mathbf{H}^T(\mathbf{H}\mathbf{P}^b\mathbf{H}^T + \mathbf{R})^{-1}$ is the Kalman filter gain matrix. In a completely linear case, this least-squares approach yields an optimal analysis. Although atmospheric and oceanic models are non-linear, the uncertainties involved are small enough that the Kalman filter approach still theoretically gives a reasonable

approximation. In practice, however, the size of ocean (and atmospheric) models (typically on the order of several million variables) makes the required matrix inversions prohibitively expensive (Hunt et al., 2007).

To get around this barrier, an ensemble is used to estimate the Gaussian error distribution and propagate it forward in time. At a given time, t_{n-1} , a k -member ensemble of initial conditions is chosen whose mean is \mathbf{x}_{n-1}^a and whose spread characterizes the covariance \mathbf{P}_{n-1}^a . Using the notation of Hunt et al. (2007), this ensemble is denoted $\{\mathbf{x}_{n-1}^{a(i)}: i = 1, 2, \dots, k\}$. Each member of this ensemble is then propagated forward using the model to form a new ensemble. This new ensemble is the background ensemble at time t_n which is written $\{\mathbf{x}_n^{b(i)}: i = 1, 2, \dots, k\}$. Because a Gaussian distribution will be mapped to a Gaussian distribution through this process, the resulting ensemble can be used to characterize the new background state \mathbf{x}_n^b and its associated covariance matrix \mathbf{P}_n^b . Specifically, the background state is the mean of the background ensemble,

$$\mathbf{x}_n^b = \frac{\sum_{i=1}^k \mathbf{x}_n^{b(i)}}{k}, \quad (1.3)$$

and the background covariance is given by

$$\mathbf{P}_n^b = \frac{\mathbf{X}^b (\mathbf{X}^b)^T}{k-1} = \frac{\sum_{i=1}^k (\mathbf{x}_n^{b(i)} - \mathbf{x}_n^b) (\mathbf{x}_n^{b(i)} - \mathbf{x}_n^b)^T}{k-1} \quad (1.4)$$

where \mathbf{X}^b is defined as the matrix whose i^{th} column is $\mathbf{x}_n^{b(i)} - \mathbf{x}_n^b$ and the time index has been dropped for simplicity. Note that there are only $k-1$ linearly independent rows in both \mathbf{P}^b and \mathbf{X}^b . This, as will be shown below, helps reduce the computational resources needed to solve Equations 1.1 and 1.2 by effectively

reducing the space over which the analysis is found to the point where the problem is expensive but feasible.

Another technique utilized by Hunt et al. (2007) to facilitate the calculation of the analysis is spatial localization. There are a number of reasons to perform spatial localization, and three are touched on here. First, breaking the problem down into independent local pieces allows the computation to be done more efficiently in parallel.

In addition to increasing the speed of the calculation, localization improves the accuracy as well. As noted above, the background covariance matrix \mathbf{P}^b has rank $k - 1$ and therefore can only represent and correct uncertainty in the (at most) $k - 1$ -dimensional subspace spanned by the ensemble members. Because atmospheric and oceanic systems are typically higher-dimensionally unstable, running a k -dimensional ensemble filter globally will not account for all of the forecast errors. It has been shown, however, that the dimension of the unstable direction can be reduced when confined to a sufficiently small region (Patil et al., 2001). This fact was utilized in the Local Ensemble Kalman Filter (Ott et al., 2004). By breaking the problem into local regions and performing the analysis individually on each region, the LETKF is able to globally correct errors over a much larger space than would otherwise be possible.

The third major benefit of localization is in eliminating spurious correlations over great distances. While using a small ensemble has many benefits, one unwelcome consequence of the small ensemble size is that these false correlations appear between far off grid points in the background covariance matrix \mathbf{P}^b . In a non-

localized analysis, these correlations would cause observations at one grid point to incorrectly influence other distant and unrelated grid points, resulting in an increase in error.

In the LETKF proposed by Hunt et al. (2007), localization is achieved by performing an independent analysis at each individual grid point using only observations from a neighborhood of that point. This is what is known as an explicit method of localization and has been used in various implementations of the ensemble Kalman filter (Houtekamer and Mitchell, 1998). An implicit method of localization can also be used, where the elements of \mathbf{P}^b are multiplied by a function that decays to zero beyond a given radius (Whitaker and Hamill, 2002).

Having discussed how localization facilitates the calculation of the analysis, the pertinent issue is then how exactly this calculation takes place. As previously discussed, the computation involves taking the background ensemble and transforming it into the analysis ensemble through the introduction of observational data. The transformation of the background ensemble to the analysis ensemble is accomplished through matrix transformations, following the Ensemble Transform Kalman Filter of Bishop et al. (2001). What follows is a summary of some key points from the method of Hunt et al. (2007).

One method of calculating the analysis, as discussed above, is through the Kalman filter equations (equations 1.1 and 1.2). It turns out that these equations are equivalent to the problem of minimizing the cost function

$$J(\mathbf{x}) = (\mathbf{x} - \mathbf{x}^b)^T (\mathbf{P}^b)^{-1} (\mathbf{x} - \mathbf{x}^b) + [\mathbf{y}^o - H(\mathbf{x})]^T \mathbf{R}^{-1} [\mathbf{y}^o - H(\mathbf{x})], \quad (1.5)$$

where H is the nonlinear observation operator. On first inspection, however, it appears that equation 1.5 is not well defined. The cost function relies on the term $(\mathbf{P}^b)^{-1}$, but since \mathbf{P}^b , as defined in equation 1.4, is an $m \times m$ matrix with $\text{rank}(\mathbf{P}^b) \leq k - 1 < m$, \mathbf{P}^b is not invertible. To get around this, Hunt et al. (2007) look to minimize J not in the full space \mathbf{R}^m , but in a subspace of \mathbf{R}^m over which $(\mathbf{P}^b)^{-1}$ makes sense. The proper subspace to use for this purpose is the column space of \mathbf{P}^b , denoted S . Since \mathbf{P}^b is a symmetric matrix, it is one-to-one on its column space S , which is the same as the column space of \mathbf{X}^b . Because of this one-to-one property, $(\mathbf{P}^b)^{-1}$ can be suitably defined on S and $(\mathbf{x} - \mathbf{x}^b)^T (\mathbf{P}^b)^{-1} (\mathbf{x} - \mathbf{x}^b)$ makes sense as long as $\mathbf{x} - \mathbf{x}^b$ is also in S . Thus the minimization of $J(\mathbf{x})$ can be performed with the restriction that $\mathbf{x} - \mathbf{x}^b \in S$.

Before proceeding with the minimization, though, a suitable basis must be chosen for the subspace S , which has dimension of at most $k-1$. While there are a number of possible avenues of pursuit in this endeavor, here it is accomplished through a coordinate transformation (Hunt et al., 2007). Specifically, the matrix \mathbf{X}^b can be viewed as a linear transformation onto S from some k -dimensional space \tilde{S} . The analysis can then be performed in the space \tilde{S} and subsequently mapped over to the space S . More precisely, let \mathbf{w} be a Gaussian random variable of 0 mean and covariance $\frac{1}{k-1}$, then the vector $\mathbf{x} = \mathbf{x}^b + \mathbf{X}^b \mathbf{w} \in S$ is Gaussian and has mean \mathbf{x}^b and covariance $\mathbf{P}^b = \frac{\mathbf{X}^b (\mathbf{X}^b)^T}{k-1}$, just as in equation 1.4. Using this change of variables, the cost function can be rewritten in terms of \mathbf{w} instead of \mathbf{x} . This yields

$$\tilde{J}(\mathbf{w}) = (k-1)\mathbf{w}^T \mathbf{w} + [\mathbf{y}^o - H(\mathbf{x}^b + \mathbf{X}^b \mathbf{w})]^T \mathbf{R}^{-1} [\mathbf{y}^o - H(\mathbf{x}^b + \mathbf{X}^b \mathbf{w})]. \quad (1.6)$$

It can be shown that if \mathbf{w}^a minimizes the cost function $\tilde{J}(\mathbf{w})$, then the corresponding vector $\mathbf{x}^a = \mathbf{x}^b + \mathbf{X}^b \mathbf{w}^a$ is a minimizer of the cost function $J(\mathbf{x})$. As a further simplification, the observational operator H can be approximated by its linearization around \mathbf{x}^b . This is the same approximation that was made when the Kalman filter equations (equations 1.1 and 1.2) were introduced earlier and is a reasonable estimation. In the method of Hunt et al. (2007), the linearization is performed by applying the nonlinear H to each member of the background ensemble to create a new ensemble $\mathbf{y}^{b(i)} = \mathbf{H}(\mathbf{x}^{b(i)})$. This leads to the linear approximation

$$H(\mathbf{x}^b + \mathbf{X}^b \mathbf{w}) \approx \mathbf{y}^b + \mathbf{Y}^b \mathbf{w}. \quad (1.7)$$

where \mathbf{y}^b is the mean of the ensemble $\{\mathbf{y}^{b(i)}\}$ and \mathbf{Y}^b is the matrix whose i^{th} column is given by $\mathbf{y}^{b(i)} - \mathbf{y}^b$. Using this approximation leads to the following updated form of the Kalman filter equations:

$$\mathbf{w}^a = \tilde{\mathbf{P}}^a (\mathbf{Y}^b)^T \mathbf{R}^{-1} (\mathbf{y}^o - \mathbf{y}^b), \quad (1.8)$$

$$\tilde{\mathbf{P}}^a = [(k-1)\mathbf{I} + (\mathbf{Y}^b)^T \mathbf{R}^{-1} \mathbf{Y}^b]^{-1}. \quad (1.9)$$

These equations solve the problem in the space $\tilde{\mathcal{S}}$ and can then be converted to the model analysis and covariance through the equations

$$\mathbf{x}^a = \mathbf{x}^b + \mathbf{X}^b \mathbf{w}^a, \quad (1.10)$$

$$\mathbf{P}^a = \mathbf{X}^b \tilde{\mathbf{P}}^a (\mathbf{X}^b)^T. \quad (1.11)$$

This process of solving in one space and transforming to another simplifies the computation and makes the scheme more efficient (Hunt et al., 2007). Finally, the new analysis ensemble is computed as

$$\mathbf{X}^a = \mathbf{X}^b \mathbf{W}^a, \quad (1.12)$$

where \mathbf{W}^a is the symmetric square root given by

$$\mathbf{W}^a = [(k - 1)\tilde{\mathbf{P}}^a]^{1/2}. \quad (1.13)$$

The use of the symmetric square root ensures that \mathbf{W}^a depends continuously on $\tilde{\mathbf{P}}^a$ and that the sum of the columns of \mathbf{X}^a are zero (Hunt et al., 2007). The matrix \mathbf{W}^a gives weights to the background ensemble members for the creation of the new analysis ensemble.

Chapter 2: Use of Breeding to Detect and Explain Instabilities in the Global Ocean

Abstract

The breeding method of finds the perturbations that grow naturally in a dynamical system like the atmosphere or the ocean. Here breeding is applied to a global ocean model forced by reanalysis winds in order to identify instabilities of weekly and monthly timescales. This chapter extends the method to show how the energy equations for the bred vectors can be derived with only very minimal approximations and used to assess the physical mechanisms that give rise to the instabilities. Tropical Instability Waves in the tropical Pacific are diagnosed, confirming the existence of bands of both baroclinic and barotropic energy conversions indicated earlier by Masina et al. and others. In the South Atlantic Convergence Zone, the bred vector energy analysis shows that there is kinetic to potential ocean eddy energy conversion, suggesting that the growing instabilities found in this area are forced by the wind. Tropical Instability Waves in the tropical Atlantic are also diagnosed, confirming similar instability mechanisms to the tropical Pacific but with a different seasonal cycle.

Motivation

Previous examinations of the structure and causes of flow instabilities in the ocean have generally required consideration of time averages of the kinetic and potential energy equations (e.g., Pinardi and Robinson, 1986; Ducet et al., 2000) or

even a full linear instability analysis (Huck and Vallis, 2001). However, the process of time averaging reduces the ability of this approach to discriminate among several concurrent instabilities with differing time-evolutions. Here the potential of the breeding method to isolate and identify the aspects of time-dependent ocean flows that are unstable to small perturbations is explored.

Like the atmosphere, upper ocean currents are subject to a variety of flow instabilities. These instabilities are concentrated in regions of strong currents such as the western sides of subtropical gyres and the deep tropics where eddy kinetic energy may exceed $4500 \text{ cm}^2\text{s}^{-2}$ (Ducet et al., 2000). Many currents, such as the Agulhas, Kuroshio, Gulf Stream, Brazil, Malvinas, and Antarctic Circumpolar Currents, have a fairly constant level of eddy variability year round. Others, such as the North Equatorial Counter Current (NECC) of the tropical Pacific, show strong seasonality. For the NECC instability generated eddy kinetic energy reaches a maximum at 10°N in summer (Ducet et al., 2000). A little south of the NECC, in the latitude range 3°N - 6°N , tropical instability waves (TIWs) occur in the longitude band between 180° and 120°W longitude. These TIWs also have a well defined seasonal cycle, with activity beginning in August and continuing through March of the next year (Masina et al., 1999).

Beginning with Philander (1976) there has been a long running discussion in the literature regarding the relative importance of baroclinic, barotropic, and frontal instabilities in providing the energy source for these TIWs. On the equator, most of the wave energy has been observed just above the Equatorial Undercurrent (EUC) (Weisberg, 1984; Luther and Johnson, 1990; Qiao and Weisberg, 1998). Using

observations from moored current meters, Weisberg (1984) calculated that the barotropic conversion in the cyclonic shear region of the EUC in the Atlantic was enough to account for the growth of the TIWs there and argued for a similar mechanism in the Pacific. In another observation experiment, Luther and Johnson (1990) argued for three distinct sources of TIW energy: the barotropic conversion in the EUC at the equator and two regions of baroclinic conversion between 3°N and 6°N and between 5°N and 9°N. More recently, numerical model simulations have been used to diagnose the instabilities. Masina et al. (1999) suggest that there are two distinct locations of energy conversion with baroclinic conversion occurring between 3°N and 5°N and barotropic energy conversion occurring further equatorward. Perturbation energy budgets performed on a 2.5 layer model by McCreary and Yu (1992) emphasized the importance of barotropic instability and introduced a frontal instability mechanism as an energy source for TIWs. Baroclinic instability, however, was found to be an energy sink. Using data from a 28-year long run of a coupled general circulation model, though, Yu and Liu (2003) found that baroclinic instability associated with the northern SST front was of major importance in generating Pacific TIWs around both 2°N and 2°S. The strength of the TIWs is closely tied to the phase of ENSO, with the diminished strength of SST front in El Niño years associated with a decrease in TIW production and the increased SST front of La Niña causing stronger TIW activity (Contreras, 2002).

To explore the potential of the breeding approach in examining fluid instabilities in the ocean the breeding method is extended by defining the potential and kinetic

energy equations for the perturbations and these equations are used to explore instabilities in an ocean general circulation model driven by observed winds.

The MOM2 Model

The primitive equation Geophysical Fluid Dynamics Laboratory (GFDL) Modular Ocean Model v.2 is used in a domain extending from 62.5°S-62.5°N with 1°x1° horizontal resolution in midlatitudes reducing to 1°x½° at the equator in order to resolve the intense equatorial current systems. The model has 20 fixed depth levels in the vertical with 15m resolution near the surface expanding to 737m near the bottom. Horizontal and vertical mixing and heat and salt diffusion parameters are set as described in Carton et al. (2000) in order to reproduce the main observed features of the time mean ocean circulation. Initial conditions of climatological temperature and salinity are obtained from the World Ocean Atlas 1994 (Levitus and Boyer, 1994), while monthly winds are provided by the National Centers for Environmental Prediction (NCEP) reanalysis (Kalnay et al., 1996). Surface heat and freshwater flux are calculated using a simple Haney-type relaxation to climatological monthly temperature and salinity.

Bred Vector Energy Equations

Overview

The derivation of the bred vector conservation of kinetic and potential energy equations resembles that of the more common perturbation energy equations (Orlanski et al. 1991; Oczkowski et al. 2005) although, due to the fact that both the

control and the perturbed nonlinear runs satisfy exactly the model equations, the bred vector equations do not require Reynolds averaging. A complete derivation of the bred vector energy equations is presented in the following section. Bred vector kinetic energy in $\text{kg m}^{-1} \text{s}^{-2}$ (Joules/m³) is defined as $KE_b \equiv \rho_0 \vec{V}_b \cdot \vec{V}_b / 2$ where \vec{V}_b is the bred vector horizontal velocity. Substituting this definition into the momentum equations, where \vec{V}_c is the control run horizontal velocity, leads to:

$$\begin{aligned} \frac{\partial KE_b}{\partial t} = & - \left[\nabla \cdot (\vec{V}_c KE_b) + \frac{\partial}{\partial z} (w_c KE_b) \right] - \left[\nabla \cdot (\vec{V}_b p_b) + \frac{\partial}{\partial z} (w_b p_b) \right] - w_b g \rho_b \\ & - \rho_0 \left[\vec{V}_b \cdot (\vec{V}_b \cdot \nabla) \vec{V}_c + \vec{V}_b \cdot \left(w_b \frac{\partial \vec{V}_c}{\partial z} \right) \right] + \rho_0 \vec{V}_b \cdot \vec{F}_b \end{aligned} \quad (2.1)$$

where w_b and w_c are bred and control vertical velocities, p_b is bred vector pressure, and ρ_b is bred vector density. The first bracketed term is horizontal and vertical divergence of the kinetic energy transport, and vanishes when integrated over the whole domain. The second is the work of the pressure force, the third is the baroclinic energy conversion between perturbation potential and perturbation kinetic energy, the fourth is barotropic energy conversion between background kinetic and bred kinetic energy, and the fifth term is a friction term. The friction term and vertical transports are generally negligible in the problems considered here.

Similarly, bred vector potential energy, defined as $PE_b \equiv \rho_b^2 g^2 / 2 \rho_0 N^2$ kg $\text{m}^{-1} \text{s}^{-3}$, where $N^2 = -\frac{g}{\rho_0} \frac{d\rho}{dz}$ is the square of the Brunt-Vaisala frequency, has the following equation:

$$\begin{aligned} \frac{\partial PE_b}{\partial t} = & - \left[\nabla \cdot (\vec{V}_c \nabla PE_b) + \frac{\partial}{\partial z} (w_c PE_b) \right] + w_b g \rho_b \\ & - \frac{\rho_b g^2}{\rho_0 N^2} \left[\nabla \cdot (\vec{V}_b \rho_c) + \frac{\partial (w_b \rho_c)}{\partial z} \right] - w_c \frac{\partial PE_b}{\partial z} \end{aligned} \quad (2.2)$$

The first bracketed term is horizontal and vertical divergence of the potential energy transport, and vanishes when integrated over the whole domain. The second term is baroclinic energy conversion and has the opposite sign of the corresponding term in the kinetic energy equation. The third term is negligible, since it is proportional to the perturbations in density times a term that vanishes when integrated over the whole domain. The last term is also negligible. The results presented here focus mainly on interpreting the bred vector kinetic energy equation.

Derivation of Bred Vector Kinetic Energy Equation

Here the bred vector kinetic energy equation and then the bred vector potential energy equation are derived. Notationally, the velocity vector of the control run is written as \vec{V}_c . The velocity of the perturbed run is then $\vec{V}_c + \vec{V}_b$, where \vec{V}_b is the bred vector velocity.

The MOM2 horizontal momentum equations for the control run are as follows:

$$\begin{aligned} \frac{\partial u_c}{\partial t} = & -\vec{V}_c \cdot \nabla u_c - w_c u_{c_z} + f v_c + \frac{u_c v_c \tan \phi}{a} - \frac{p_{c\lambda}}{a \rho_0 \cos \phi} + (\kappa_m u_{c_z})_z \\ & + F^{u_c} \end{aligned} \quad (2.3)$$

$$\frac{\partial v_c}{\partial t} = -\vec{V}_c \cdot \nabla v_c - w_c v_{c_z} - f u_c + \frac{u_c^2 \tan \phi}{a} - \frac{p_{c\phi}}{a \rho_0} + (\kappa_m v_{c_z})_z + F^{v_c} \quad (2.4)$$

This means that the momentum equations for the perturbed case are:

$$\begin{aligned} \frac{\partial(u_c + u_b)}{\partial t} = & -(\vec{V}_c + \vec{V}_b) \cdot \nabla(u_c + u_b) - (w_c + w_b)(u_c + u_b)_z \\ & + f(v_c + v_b) + \frac{(u_c + u_b)(v_c + v_b) \tan \phi}{a} \\ & - \frac{(p_c + p_b)_\lambda}{a\rho_0 \cos \phi} + (\kappa_m(u_c + u_b)_z)_z + F^{u_c+u_b} \end{aligned} \quad (2.5)$$

$$\begin{aligned} \frac{\partial(v_c + v_b)}{\partial t} = & -(\vec{V}_c + \vec{V}_b) \cdot \nabla(v_c + v_b) - (w_c + w_b)(v_c + v_b)_z \\ & - f(u_c + u_b) + \frac{(u_c + u_b)^2 \tan \phi}{a} \\ & - \frac{(p_c + p_b)_\phi}{a\rho_0} + (\kappa_m(v_c + v_b)_z)_z + F^{v_c+v_b} \end{aligned} \quad (2.6)$$

The bred vector momentum equations are then the difference between the perturbed momentum equations and the control momentum equations. Taking this difference yields:

$$\begin{aligned} \frac{\partial u_b}{\partial t} = & -\vec{V}_c \cdot \nabla u_b - \vec{V}_b \cdot \nabla u_c - \vec{V}_b \cdot \nabla u_b - w_c u_{bz} - w_b u_{cz} - w_b u_{bz} + f v_b \\ = & + \frac{(u_c v_b + u_b v_c + u_b v_b) \tan \phi}{a} - \frac{p_{b\lambda}}{a\rho_0 \cos \phi} \\ & + (\kappa_m u_{bz})_z + F^{u_b} \end{aligned} \quad (2.7)$$

$$\begin{aligned} \frac{\partial v_b}{\partial t} = & -\vec{V}_c \cdot \nabla v_b - \vec{V}_b \cdot \nabla v_c - \vec{V}_b \cdot \nabla v_b - w_c v_{bz} - w_b v_{cz} - w_b v_{bz} - f u_b \\ & + \frac{(2u_c u_b + u_b^2) \tan \phi}{a} - \frac{p_{b\phi}}{a\rho_0} + (\kappa_m v_{bz})_z + F^{v_b} \end{aligned} \quad (2.8)$$

The bred vector kinetic energy, KE_b , is defined as $KE_b = \frac{\rho_0}{2} \vec{V}_b \cdot \vec{V}_b$. Taking the dot product of \vec{V}_b and $\frac{\partial \vec{V}_b}{\partial t}$ leads to the kinetic energy equation for the bred perturbation:

$$\begin{aligned} \frac{\partial KE_b}{\partial t} = & -\vec{V}_c \cdot \nabla KE_b - \rho_0 \vec{V}_b \cdot (\vec{V}_b \cdot \nabla) \vec{V}_c - \vec{V}_b \cdot \nabla KE_b - w_c KE_{b_z} - \rho_0 \vec{V}_b \\ & \cdot (w_b \vec{V}_{c_z}) - w_b KE_{b_z} - \frac{u_b p_{b\lambda}}{a \cos \phi} - \frac{v_b p_{b\phi}}{a} \\ & + \frac{\rho_0 (u_b^2 v_c - v_b u_c u_b) \tan \phi}{a} + \rho_0 v_b (\kappa_m v_{b_z})_z \\ & + \rho_0 u_b (\kappa_m u_{b_z})_z + \rho_0 \vec{V}_b \cdot \vec{F}^{\vec{V}_b} \end{aligned} \quad (2.9)$$

This equation can be rewritten making a few approximations. First, a few of these terms are very small and can be ignored. The metric term is negligible

$\left(\frac{\rho_0 (u_b^2 v_c - v_b u_c u_b) \tan \phi}{a} \approx 0 \right)$ and can be disregarded. The term $w_b KE_{b_z}$ is, on average,

two orders of magnitude smaller than the similar term $w_c KE_{b_z}$, while $\vec{V}_b \cdot \nabla KE_b$ is

two to three orders of magnitude smaller than $\vec{V}_c \cdot \nabla KE_b$. Since $w_b \ll w_c$ and $\vec{V}_b \ll$

\vec{V}_c , the terms $w_b KE_{b_z}$ and $\vec{V}_b \cdot \nabla KE_b$ can be ignored. Next, a couple of the terms can

be combined, so

$$-\frac{u_b p_{b\lambda}}{a \cos \phi} - \frac{v_b p_{b\phi}}{a} = -\vec{V}_b \cdot \nabla p_b \text{ and } \rho_0 v_b (\kappa_m v_{b_z})_z + \rho_0 u_b (\kappa_m u_{b_z})_z + \rho_0 \vec{V}_b \cdot \vec{F}^{\vec{V}_b} =$$

$\rho_0 \vec{V}_b \cdot \vec{F}_b$. Equation 2.9 then becomes:

$$\begin{aligned} \frac{\partial KE_b}{\partial t} = & -\vec{V}_c \cdot \nabla KE_b - \rho_0 \vec{V}_b \cdot (\vec{V}_b \cdot \nabla) \vec{V}_c - \rho_0 \vec{V}_b \cdot (w_b \vec{V}_{c_z}) - w_b KE_{b_z} + \vec{V}_b \\ & \cdot \nabla p_b + \rho_0 \vec{V}_b \cdot \vec{F}_b \end{aligned} \quad (2.10)$$

Next some of the terms can be expanded. First,

$$-\vec{V}_c \cdot \nabla KE_b = -\nabla \cdot (\vec{V}_c KE_b) + KE_b \nabla \cdot \vec{V}_c = -\nabla \cdot (\vec{V}_c KE_b) + KE_b w_{c_z}$$

The last equality comes from the continuity equation, $\nabla \cdot \vec{V} + w_z = 0$. Also, using the continuity equation and the hydrostatic approximation,

$$\begin{aligned} -\vec{V}_b \cdot \nabla p_b &= -\nabla \cdot (\vec{V}_b p_b) + p_b \cdot \nabla \vec{V}_b = -\nabla \cdot (\vec{V}_b p_b) + p_b w_{bz} \\ &= -\nabla \cdot (\vec{V}_b p_b) - \frac{\partial (w_b p_b)}{\partial z} + w_b \frac{\partial p_b}{\partial z} \\ &= -\nabla \cdot (\vec{V}_b p_b) - \frac{\partial (w_b p_b)}{\partial z} - w_b g \rho_b. \end{aligned}$$

Making these two substitutions and grouping the terms yields the following bred vector kinetic energy equation:

$$\begin{aligned} \frac{\partial KE_b}{\partial t} &= - \left[\nabla \cdot (\vec{V}_c KE_b) + \frac{\partial}{\partial z} (w_c KE_b) \right] - \left[\nabla \cdot (\vec{V}_b p_b) + \frac{\partial}{\partial z} (w_b p_b) \right] - w_b g \rho_b - \quad (2.11) \\ &\rho_0 \left[\vec{V}_b \cdot (\vec{V}_b \cdot \nabla) \vec{V}_c + \vec{V}_b \cdot \left(w_b \frac{\partial \vec{V}_c}{\partial z} \right) \right] + \rho_0 \vec{V}_b \cdot \vec{F}_b. \end{aligned}$$

The barotropic energy conversion term (the fourth term in square brackets with horizontal and vertical shear components) can be rewritten as $-\vec{V}_b \cdot (\vec{V}_{b3} \cdot \nabla_3) \vec{V}_c$, where $\nabla_3 = \left(\nabla, \frac{\partial}{\partial z} \right)$ is the three dimensional gradient and $\vec{V}_{b3} = (\vec{V}_b, w_b)$ is the three dimensional velocity vector.

Derivation of Bred Vector Potential Energy Equation

The bred vector potential energy equation is derived in an analogous manner to the bred vector kinetic energy equation. The process begins with the mass conservation equation

$$\frac{D\rho}{Dt} + \rho \nabla_3 \cdot \vec{V} = 0. \quad (2.12)$$

Expanding equation 2.12 and using incompressibility yields:

$$\rho_t + u\rho_x + v\rho_y + w\rho_z = 0. \quad (2.13)$$

For this calculation the density is divided into a perturbation density, ρ' , from an equilibrium solution, $\rho_0(z)$, so $\rho = \rho_0 + \rho'$. Plugging this into equation 2.13 gives a lot of terms, but some may be neglected because of the scale. For the time and horizontal derivatives, the derivative of the perturbation density is much larger than the derivative of the equilibrium density, so we can ignore the terms involving ρ_{0t} , ρ_{0x} , and ρ_{0y} . On the other hand, the derivative of the equilibrium density is the dominant term in the vertical direction, so the term involving ρ'_z is ignored. In addition, the density is split into control and bred vector components. It is assumed that ρ_0 is the same for both runs, so the only difference is in the perturbation density. Thus instead of using ρ' , the control and perturbation run densities are written as $\rho_{control} = \rho_0 + \rho_c$ and $\rho_{perturbed} = \rho_0 + \rho_c + \rho_b$. This leaves the following equation for the control run:

$$\rho_{ct} + u_c \rho_{cx} + v_c \rho_{cy} + w_c \rho_{0z} = 0. \quad (2.14)$$

For the perturbed run, the velocities are again the sum of the control and bred vector values. After making these assumptions, the equation for the perturbed run becomes:

$$\begin{aligned} \rho_{ct} + \rho_{bt} + (u_c + u_b)(\rho_{cx} + \rho_{bx}) + (v_c + v_b)(\rho_{cy} + \rho_{by}) + (w_c + w_b)\rho_{0z} \\ = 0. \end{aligned} \quad (2.15)$$

Subtracting the control run equation from the perturbed run equation yields the bred vector equation:

$$\rho_{bt} + u_b \rho_{cx} + u_c \rho_{bx} + u_b \rho_{bx} + v_b \rho_{cy} + v_c \rho_{by} + v_b \rho_{by} + w_b \rho_{0z} = 0. \quad (2.16)$$

To calculate the potential energy change, this equation is multiplied through by $\frac{\rho_b g^2}{\rho_0 N^2}$.

Letting the bred vector potential energy be $PE_b = \frac{\rho_b g^2}{2\rho_0 N^2}$, where N^2 is the square of

the Brunt-Vaisala frequency, leads to the following bred vector potential energy equation:

$$\frac{\partial PE_b}{\partial t} = -\vec{V}_c \cdot \nabla PE_b - \vec{V}_b \cdot \nabla PE_b - \frac{\rho_b g^2}{\rho_0 N^2} \vec{V}_b \cdot \nabla \rho_c - \frac{\rho_b g^2 w_b}{\rho_0 N^2} \rho_{0z} \quad (2.17)$$

The first and second terms in this equation are both advection of kinetic energy. Since $\vec{V}_c \gg \vec{V}_b$, the advection by the bred vector velocity can be ignored, leaving only the first term. As was done in deriving the kinetic energy equation, the first term can be rewritten

$$-\vec{V}_c \cdot \nabla PE_b = -\nabla \cdot (\vec{V}_c PE_b) + PE_b \nabla \cdot \vec{V}_c = -\nabla \cdot (\vec{V}_c PE_b) + PE_b w_{c_z} \quad (2.18)$$

For the third term, we can rewrite

$$\begin{aligned} -\vec{V}_b \cdot \nabla \rho_c &= -\nabla \cdot (\vec{V}_b \rho_c) + \rho_c \cdot \nabla \vec{V}_b = -\nabla \cdot (\vec{V}_b \rho_c) - \rho_c w_{b_z} \\ &= -\nabla \cdot (\vec{V}_b \rho_c) - \frac{\partial (w_b \rho_c)}{\partial z} + w_b \rho_{c_z} \end{aligned} \quad (2.19)$$

As discussed above, the vertical derivative of ρ_c is negligible as compared to the vertical derivative of ρ_0 , so the $w_b \rho_{c_z}$ piece of the above equation can be ignored.

Finally, N^2 is defined since $N^2 = -\frac{g}{\rho_0} \frac{\partial \rho_0}{\partial z}$, so $\frac{\partial \rho_0}{\partial z} = -\frac{\rho_0 N^2}{g}$. Substituting this into the fourth term of Equation 2.17 yields:

$$-\frac{\rho_b g^2 w_b}{\rho_0 N^2} \rho_{0z} = \frac{\rho_b g^2 w_b \rho_0 N^2}{\rho_0 N^2 g} = w_b g \rho_b \quad (2.20)$$

After rewriting all of the terms of equation 2.17, the final bred vector potential energy equation is

$$\frac{\partial PE_b}{\partial t} = - \left[-\nabla \cdot (\vec{V}_c PE_b) + \frac{\partial}{\partial z} (w_c PE_b) \right] + w_b g \rho_b \quad (2.21)$$

$$- \frac{\rho_b g^2}{\rho_0 N^2} \left[\nabla \cdot (\vec{V}_b \rho_c) + \frac{\partial}{\partial z} (w_b \rho_c) \right] - w_c \frac{\partial}{\partial z} (PE_b)$$

As was previously mentioned, the first term is advection of potential energy by the control velocity. The second term is the conversion from potential to kinetic energy. It is the same term that appeared in equation 2.11, only with the opposite sign.

Breeding in the Global Ocean

Experiment Setup

To begin the breeding process, a random perturbation sampled from a flat distribution between -0.5°C and 0.5°C is introduced into the initial conditions for the sea surface temperature (SST) field. The remaining experiments reported here all use this same initial perturbation. Other experiments using different randomly chosen initial perturbations or perturbations in the velocity field yield similar results, confirming the earlier observation by Toth and Kalnay (1993, 1997) that the structure of the bred vectors is independent of the initial perturbation.

Results from control and bred vector simulations spanning two periods are examined, a multi-decadal period beginning January 1951 through December 1979 and a shorter, observation-rich period spanning the eight year period January 1985 through December 1992. We will focus on the latter period, although the longer run is used to compute climatological monthly averages. A monthly breeding interval is used for the shorter simulation, while a 10 day breeding interval is used for the longer simulation to better isolate the period of TIWs.

Although the resolution of the model is not high enough to resolve much of the boundary current instabilities, the bred vectors show evidence of western boundary current instabilities, in addition to their seasonal cycle. In April (**Fig. 2.1a**), for example, instabilities are visible primarily in the Northern Hemisphere. Specifically, instabilities can be seen at the top of the Gulf Stream and the Kuroshio Current, along the Pacific Subtropical Front, and along the Pacific equator. The mid-latitude instabilities in the Southern Hemisphere and instabilities in the tropics are much more prominent in November (**Fig. 2.1b**). The most dominant features in the BVs, though, are tropical instabilities in the Pacific Ocean. These Pacific instabilities are particularly strong throughout the boreal winter.

Pacific Tropical Instabilities

We begin by considering the bred vector energy balance on 11 November 1988, a time when the tropical Pacific was in a late developing La Niña (with a Southern Oscillation Index of 21.0 and a Nino3.4 Index value of -2°C). The bred vector shows a dipole pattern off the coast of South America and a wave pattern in the Tropical Pacific (**Fig. 2.2a**) which successive bred vectors have a period of ~ 25 days and to propagate westward at 0.46m/s . Examination of the bred vector energetics shows that baroclinic processes are causing an increase in bred vector kinetic energy along the equator (**Fig. 2.2b**). In the region of the dipole pattern in the South Atlantic off the coast of South America, by contrast, there is a conversion from bred vector kinetic to potential energy consistent with a transfer of bred vector kinetic energy from the atmosphere to the ocean, which is then converted into bred vector potential energy.

Tropical waves in this simulation first appear in August, are seen to strengthen through the winter, and then dissipate by May of the following year (**Fig. 2.3**). Bred vector baroclinic energy conversion exhibits the same seasonal cycle, with conversion increasing in August between 150°W and 120°W and shifting westward and extending to approximately 200°W by the end of the year (**Fig. 2.2b**). Bred vector baroclinic energy conversion is maximum along the northern edge of the Pacific equatorial cold tongue, between 3°N and 5°N (**Fig. 2.4a**). Positive barotropic conversion (red) is seen in two latitude bands. The maximum of barotropic energy conversion occurs just north of the Equator, while bred vector barotropic conversion can also be seen in the same 3°N to 5°N latitude band as baroclinic conversion (**Fig. 2.4a**).

We next consider the interannual dependence of the energy conversion terms (**Fig 2.4b**). Both baroclinic and barotropic energy conversion terms spike during August through January, with the size of the spike varying by year. The strongest spike in energy conversion occurs in the La Niña period of 1988-1989 when the TIWs, NECC, and Equatorial Undercurrent are all anomalously strong. During this spike in energy conversion, baroclinic energy conversion is positive, indicating a conversion from bred potential to bred kinetic energy, while the barotropic conversion is negative, indicating a transfer from bred kinetic energy to background kinetic energy. In contrast to the La Niña period, bred vector energy conversion is weak during the 1991-1992 El Niño when the Equatorial Undercurrent has reduced transport and TIWs are weak.

Finally, we examine the vertical structure of the bred vector energy conversion. The majority of the baroclinic conversion occurs above the thermocline, with the strongest conversion taking place in the upper 100 meters. This can be seen in the October average, which is qualitatively representative of the location and pattern of the relative amplitude of the conversion during fall and winter months (**Fig. 2.5a**). The longitude of this maximum baroclinic conversion corresponds to the location of the tongue of cool SSTs (which can be seen at the surface of the middle of **Fig. 2.5a**) and consequent strong meridional SST gradient. Barotropic conversion also occurs in this region and along the equator between 160°W and 125°W (**Fig. 2.5b**) although it takes place deeper than baroclinic conversion, with the strongest conversion at and just below the shear zone between the westward South Equatorial Current and the eastward Equatorial Undercurrent

Atlantic Tropical Instabilities

Though the Pacific tropical instabilities are the most dominant feature in the 10-day bred vectors, instabilities in the Atlantic and Indian Oceans are also visible. These instabilities are not analyzed here in as much depth as the Pacific, although some results from the Atlantic are presented. Atlantic TIWs have a similar 25 day central periodicity to that of Pacific TIWs. The first begin to appear in May, reach an energy peak in June, and persist through August. A secondary peak is also seen in December before the waves vanish in February or March (Weisberg, 1984; Jochem et al., 2003). Atlantic TIWs are found west of 8°W and most of the activity is between 3°N and 3°S (Weisberg and Weingartner, 1988).

The same dynamic processes that control Pacific TIWs have been argued for Atlantic TIWs. Philander (1996) showed that barotropic instabilities in the equatorial zonal currents can generate waves similar to observed TIWs. Studies have confirmed this and also argued for a component of baroclinic instability in TIW generation (Cox, 1980; Masina et al., 1999). In the Pacific, Masina et al. (1999) argued that baroclinic conversion was the dominant mechanism for TIWs. In a separate modeling study, however, Jochum et al. (2003) found that barotropic instabilities were dominant. It was postulated that this difference could be attributed to either a difference in the basins or a difference in viscosity between the two models (Jochum et al., 2003).

To explore the Atlantic, the same monthly averages that were used in the Pacific case (**Fig. 2.4a**) are presented for baroclinic conversion in the Atlantic (**Fig. 2.6**). As in the Pacific case, the north edge of the equatorial cold tongue is of vital importance in the Atlantic waves. In the Atlantic the conversion from bred potential to bred kinetic energy in the cold tongue region takes place between the equator and 2°N, which is farther south than in the Pacific. Conversion from bred potential to bred kinetic energy is seen stretching across to the Western Atlantic between the equator and 2°N starting in June and persisting through August. In addition, weaker positive baroclinic conversion also occurs between December and February in the same locations. There is virtually no baroclinic conversion in boreal spring or fall. Most of the baroclinic conversion is occurring along the thermocline in areas with colder SST (**Fig. 2.7a**). This underscores the importance of the equatorial cold tongue in TIW production. An active area of conversion is visible year-round in the very west of the basin in the fast moving western boundary current. Eddies can be seen coming off of

the boundary current and leading to energy conversion in the area around 45°W and 5°N (**Fig. 2.6, Fig. 2.8**).

During the boreal spring and fall, the temperature profile is more stratified and the SST is higher, which leads to a decrease in TIWs. Baroclinic conversion still takes place along the thermocline in boreal fall and spring, but at a decreased rate. There is also significant baroclinic instability decay in the western edge of the basin, particularly in the western boundary current off the coast of Brazil and at 45°W between 3°N and 7°N. The strongest barotropic conversion in the tropical Atlantic takes place as a result of the shear created by the fast moving western boundary currents. This conversion is present and positive for the entire year between approximately 45°W and 35°W and is the most prominent Atlantic feature (**Fig. 2.8**). Off the west edge of the basin, barotropic conversion, like baroclinic conversion, is weak in boreal spring and then picks up starting in June. Barotropic conversion persists through December and the spatial pattern of the conversion can be seen in October (**Fig. 2.8**). The majority of barotropic conversion occurs along the top of the Equatorial Undercurrent (**Fig. 2.7b**). Barotropic conversion in this simulation is not as strong as baroclinic conversion. A possible explanation for the low levels of barotropic conversion is the relatively high viscosity used in the model.

South Atlantic Instabilities

The largest amplitude in the November bred vector is in the Southern Ocean eddies and the dipole off of South America (**Fig. 2.2a**). This South American dipole is a prominent feature throughout the year and occurs in a location that has significant variability in both the atmosphere, the South Atlantic Convergence Zone (SACZ),

and the ocean, the Brazil-Malvinas Confluence (BMC). This dipole pattern off South America is consistent with observed atmospheric phenomena in the SACZ, which show a "seesaw" pattern that is thought to be related to tropical oscillations with periods between 30-60 days (Nogués-Paegle and Mo, 1997). There are also oscillations that have been detected in the BMC with periods of around 25 days. The BMC oscillations are associated with a dipole wave rotating around the Zapiola Rise (Fu et al., 2001).

Instead of looking at time averages, the instantaneous conversion is used here. At the surface, the baroclinic conversion term is mostly negative (**Fig. 2.9a**), indicating a conversion from bred vector kinetic energy to bred vector potential energy. Barotropic conversion (**Fig. 2.9b**) around 45°W is weak, with only small negative conversion near the surface. The zonal velocity at 45°W, though, has a near-surface region of increased shear which is suggestive of wind surface forcing in this region. Farther off the coast (~20°W), negative barotropic conversion occurs in the top 200-400 meters of the ocean in a narrow longitude band coincident with a longitudinal shear in the zonal velocity (**Fig. 2.9b**).

Summary

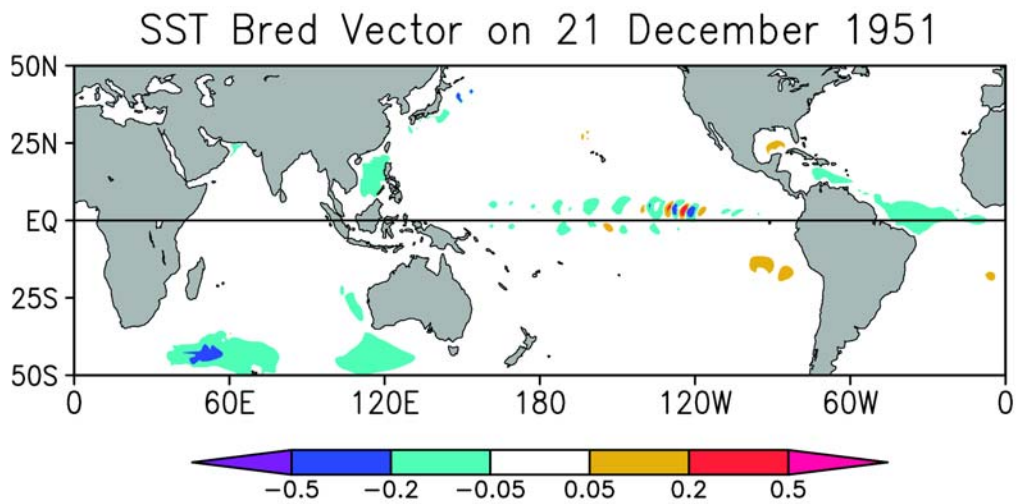
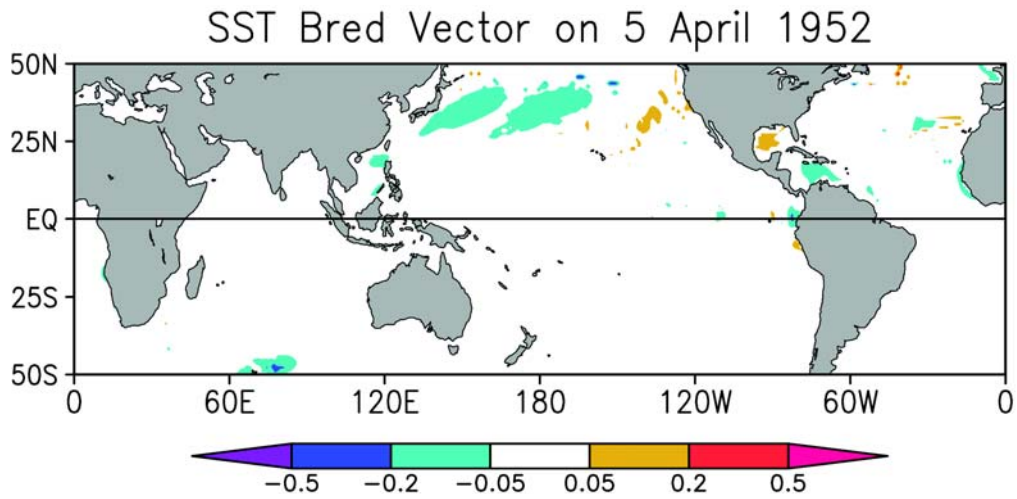
The purpose of this chapter is to apply bred vectors, an idea developed in the context of atmospheric data assimilation, to stability analysis of ocean circulation. As part of this application the bred vector energy equations are introduced, which are analogous to the more traditional eddy energy equations but are obtained without averaging or approximations other than the neglect of terms shown to be small by scale analysis due to the fact that both the control and the perturbed runs satisfy the

model dynamical equations. It is found, consistent with findings reported in Yang et al. (2006), that changes in bred vector energy reflect important aspects of the growth of flow instabilities. Thus, breeding, the process by which the bred vectors are constructed, is able to identify ocean instabilities effectively and inexpensively. Because they span the state space described by key ocean processes, bred vectors also have potential applications in the construction of ensembles of model states for ensemble data assimilation and forecasting.

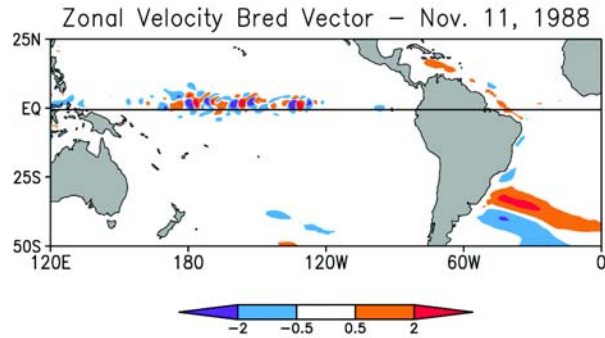
This examination of bred vectors in the global ocean focuses on instabilities of tropical Pacific currents because of their intensity, their importance for coupled air-sea interactions, and because of the extensive literature describing them. Examination of the bred vector energy equations shows that there are two locations of energy conversion for the tropical instability waves which dominate intraseasonal variability in this region. Between 3°N and 5°N, both baroclinic and barotropic energy conversion occurs along the northern edge of the cool tongue. A separate region of barotropic conversion is detected just north of the equator in the shear zone between the Equatorial Undercurrent and the shallower South Equatorial Current, e.g. in agreement with Massina et al. (1999). Both types of energy conversion have interannual variations due to changes in the currents and stratification, which are themselves closely tied to the phase of ENSO.

The analysis of bred vectors also extends to instabilities in the tropical Atlantic and the Southwestern Atlantic. Examination of the bred vector energy equations shows that tropical instabilities in the Atlantic have energy conversion along the equator in the cold tongue. Both baroclinic and barotropic conversion are detected in

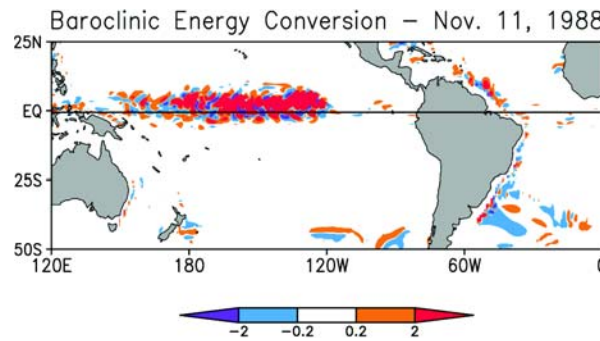
this area, with barotropic conversion occurring along the top of the Equatorial Undercurrent and baroclinic conversion occurring along the thermocline in areas with colder SST. In these experiments, baroclinic conversion is stronger than barotropic conversion, which is in disagreement with Jochum et al. (2003). This difference, however, may be explained by the high, less realistic, viscosity used in this implementation of MOM2.



2.1 (a) The SST bred vector [C] on 5 April 1952, a time when there is relatively low activity from tropical instabilities. (b) The SST bred vector [C] on 21 December 1951, when Pacific tropical instabilities are visible.



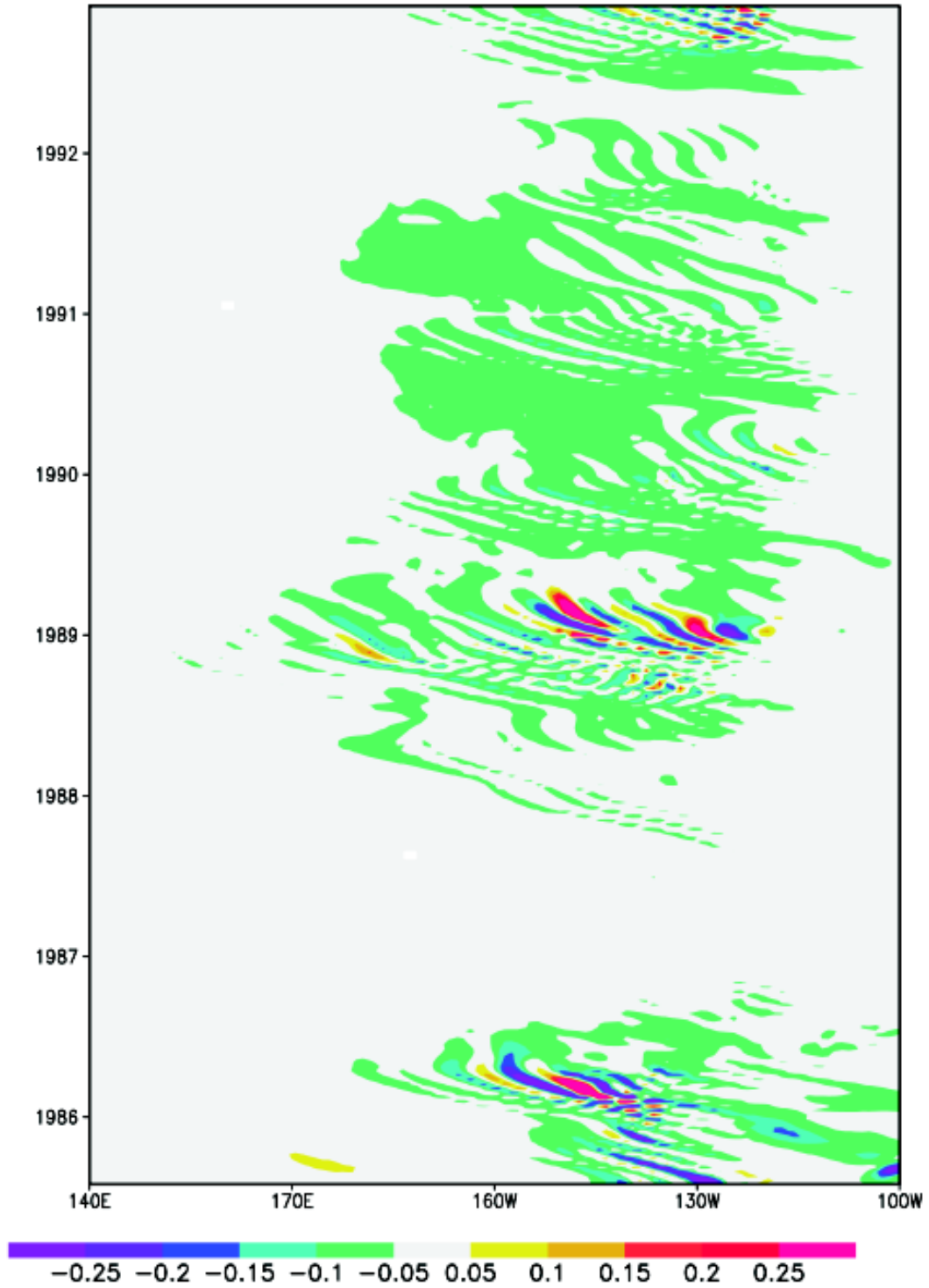
(a)



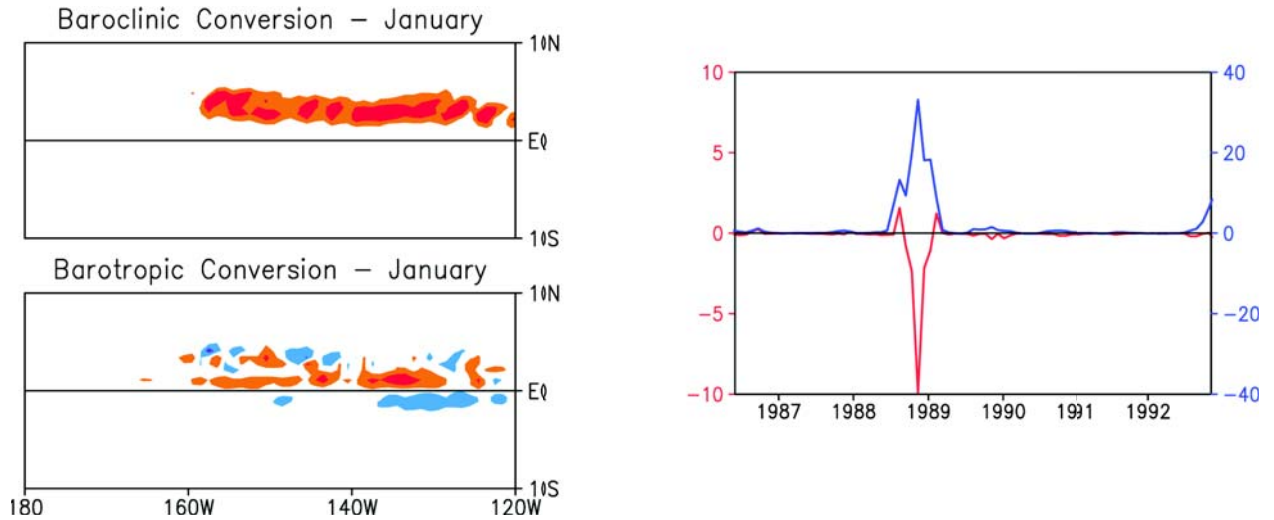
(b)

2.2 (a) Bred vector of zonal velocity on 11 November 1988, a time when the tropical Pacific was in a late developing La Niña with a Southern Oscillation Index of 21.0 and a Nino3.4 Index of -2°C . (b) The corresponding baroclinic energy conversion term. Baroclinic energy conversion contributes to the growth of bred vector kinetic energy along the Pacific equator. Off the coast of South America the baroclinic conversion term acts to convert bred vector kinetic to potential energy. The magnitudes of the fields are somewhat arbitrary due to the rescaling of the bred vectors, but the units are m/s for the velocity and $10^{-6} \text{ kg m}^{-1} \text{ s}^{-3}$ for the baroclinic energy conversion.

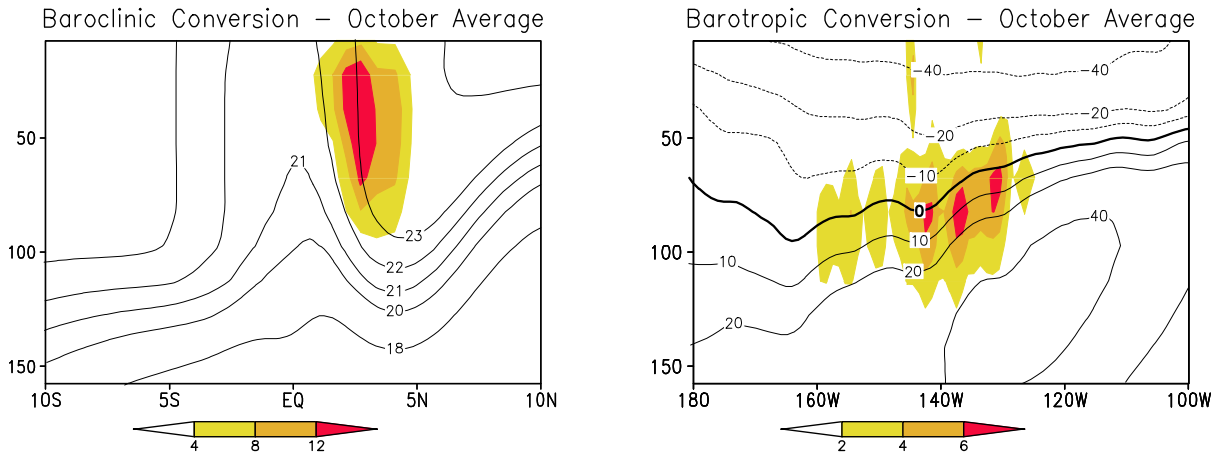
SST Bred Vector at 3.5N



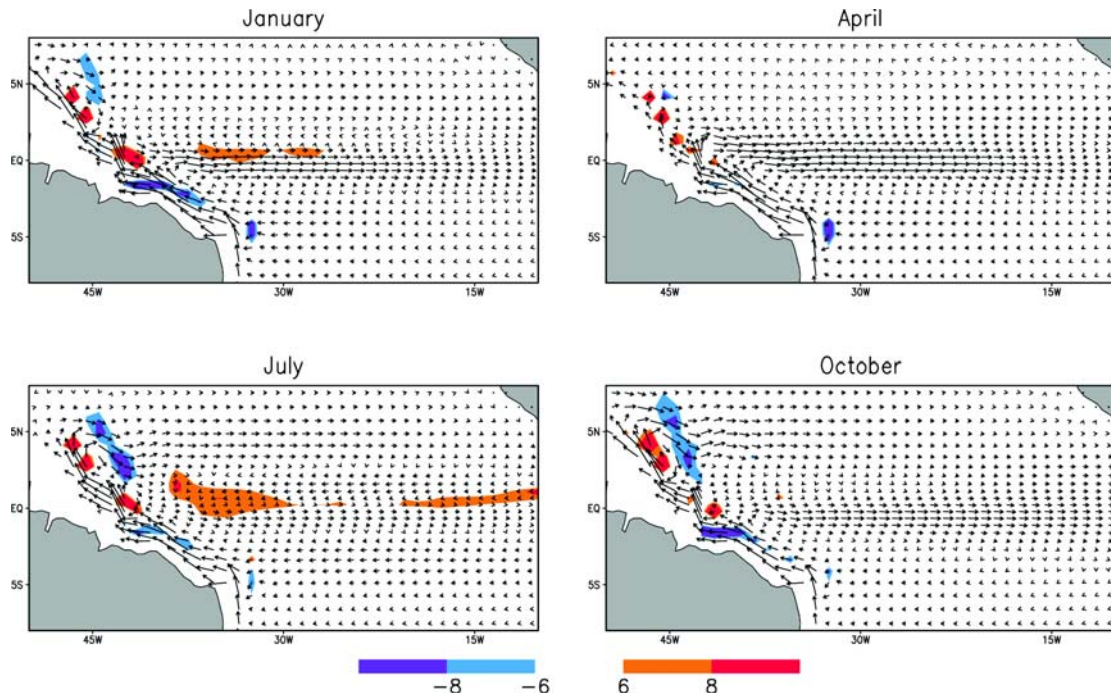
2.3 Time-longitude diagram of the SST bred vector at 3.5°N latitude from June 1985 to December 1992.



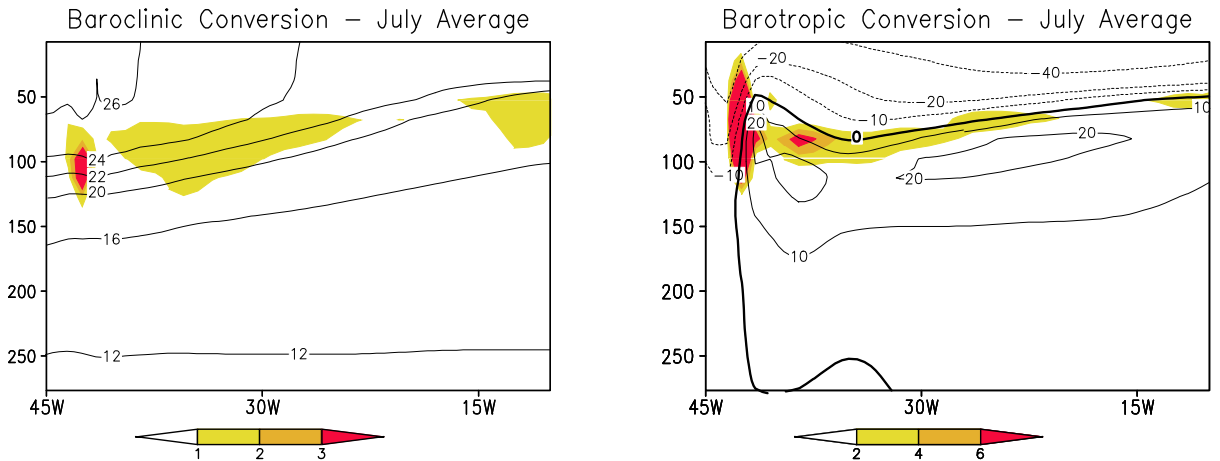
2.4 (a) The panels show the 30 year averages of the baroclinic (top panel) and barotropic (bottom panel) conversion terms for the month of January, during which barotropic energy has a peak and baroclinic energy is very strong. Positive conversion is shown in red while negative conversion is in blue. Although other months show the bred vector energy conversion occurring in different longitude regions, the January average of the conversion terms is shown here because it is representative of the shape and latitudinal location of the bred vector energy conversion. It is important to note that the sign and relative magnitude of the bred vector energy conversion terms indicate the shape, direction, and location of the energy conversion; however, the absolute magnitude of the energy conversion is not determined by this analysis. (b) The time series from June 1986 to December 1992 of the baroclinic (blue) and barotropic (red) conversion terms averaged between 180°W to 120°W longitude, -5°S to 5°N latitude, and between the surface and 150m depth. The energy conversion can be seen to increase in late summer and die off by May of the following year. In the La Niña year of 1988-1989, a significant increase in energy conversion occurs. The vertical axis has units $10^{-7} \text{ kg m}^{-1} \text{ s}^{-3}$.



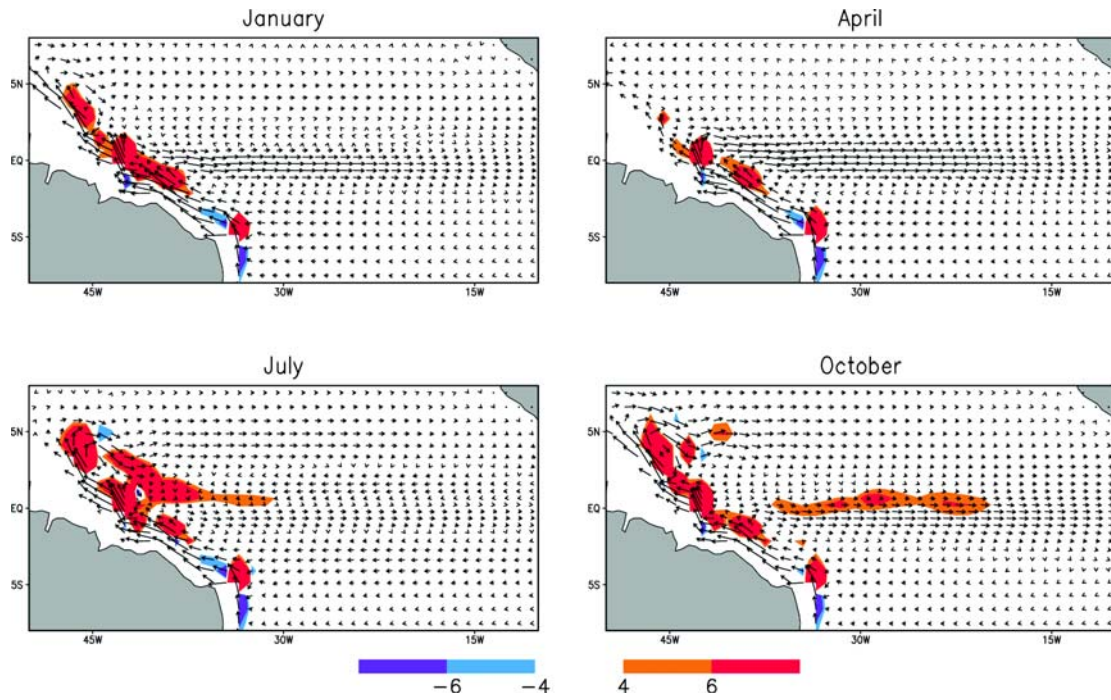
2.5 Vertical profile of climatological October properties computed from the 30 year monthly average. (a) The baroclinic conversion term (shaded) and temperature (contours) with latitude between 180° to 110° W, and (b) the barotropic conversion term (shaded) and zonal velocity (contours) with longitude at 0.65° N. Both the baroclinic and barotropic terms have units $10^{-6} \text{ kg m}^{-1} \text{ s}^{-3}$. Baroclinic conversion from potential to kinetic bred perturbation energy occurs above the thermocline with maximum at the latitude of coldest SST. This area of coldest SST (top center of (a)) corresponds to the Pacific cold tongue. The maximum barotropic conversion from the background kinetic energy to the bred perturbation occurs along the shear zone between the westward South Equatorial Current and eastward Equatorial Undercurrent. The October average is shown here because it is qualitatively representative of the location and pattern of the relative amplitude of the conversion during fall and winter months.



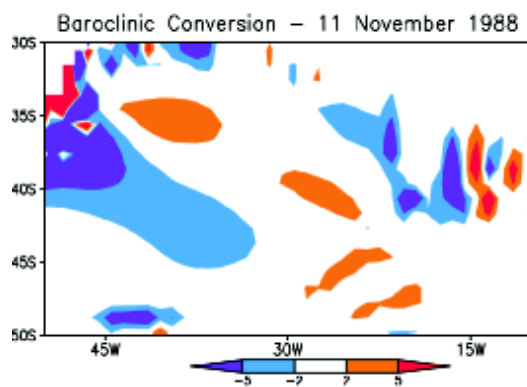
2.6 The vertically averaged baroclinic conversion term (shaded) and vertically averaged current vectors in the equatorial Atlantic from 8°S to 8°N and 45°W to 10°W. All values are $10^{-7} \text{ kg m}^{-1} \text{ s}^{-3}$.



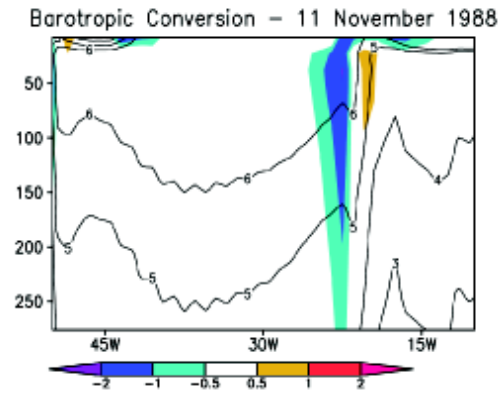
2.7 a) Vertical profile of the monthly averaged temperature in July from 1951 to 1979 (contour) overlaid on the averaged baroclinic conversion term (contour) in the equatorial Atlantic at 0.65°N and between 50°W to 10°W . The majority of the baroclinic conversion is taking place along the thermocline. (b) Vertical profile of the monthly averaged zonal velocity in July from 1951 to 1979 (contour) overlaid on the averaged barotropic conversion term (shaded) in the same region.



2.8 The vertically averaged barotropic conversion term (shaded) and vertically averaged current vectors in the equatorial Atlantic from 8°S to 8°N and 45°W to 10°W. All values are $10^{-8} \text{ kg m}^{-1} \text{ s}^{-3}$.



(a)



(b)

2.9 (a) The surface baroclinic conversion term on 11 November 1988 in the Western South Atlantic Ocean off the coast of South America. (b) The vertical profile of the barotropic conversion term (shaded) [$10^{-9} \text{ kg m}^{-1} \text{ s}^{-3}$] at 40°S on 11 November 1988 overlaid with the zonal velocity [cm/s] (contour) in the same region.

Chapter 3: An Advanced Data Assimilation System for the Chesapeake Bay

Abstract

Data assimilation methods, which combine current observational data with previous state estimates based on numerical models to create a more accurate state estimate, have the potential to improve coastal and estuary prediction systems. Here a Chesapeake Bay implementation of the Regional Ocean Modeling System (ROMS) is coupled with the local ensemble transform Kalman filter (LETKF). This chapter uses identical twin experiments, where a model run is taken to be the true state, to explore the potential of data assimilation for the Chesapeake Bay and to evaluate the current observational network in the Bay. The LETKF performs well, with analysis errors becoming smaller than observation errors within a few cycles and staying smaller than forecast errors using no data assimilation. Ensemble data assimilation also allows for observation targeting along with the assimilation and this is used in this chapter to identify the areas and seasons when observations are most beneficial.

Introduction

As the largest estuary in North America, the Chesapeake Bay is an economically and ecologically important resource. Approximately \$1 billion is brought in yearly by the shellfish and finfish harvest and millions more come in through sport fishing, boating, and other recreational activities. The Chesapeake Bay and supported wetlands system is home to 173 species of shellfish, 348 kinds of finfish, 29 types of waterfowl, and 2700 plant species. Most of the Chesapeake is

shallow, with an average depth of approximately 6.5 meters, with a deep channel running up the main stem of the Bay and reaching a maximum depth of 63 meters. The Bay is 300km long and 50km wide at its widest.

The circulation of the Chesapeake Bay has been modeled since the 1950s using equations of longitudinal momentum and water and salt mass balance (Pritchard, 1952, 1954, 1956). The main longitudinal circulation of the Chesapeake is a two-layer, salt wedge structure with salt water from the ocean entering through the channel at lower depths and freshwater exiting at the surface and creating a freshwater outflow plume. Tidal amplitude in the Bay is moderate, with a 0.91 meter mean tidal range at the mouth of the Bay, 0.70 meters at the head, and between 0.30 to 0.46 meters at most of the gauges along the main stem (Hicks, 1964).

A large freshwater runoff characterizes the Chesapeake, with approximately 38 million gallons of water per minute entering the Bay. About 50% of that freshwater comes from the Susquehanna River, 18% comes from the Potomac River, 14% comes from the James River, and 18% comes from the remaining rivers. Near the head of the Bay, the Susquehanna discharge determines the flow on timescales of 5 days and wind forcing has a large impact on scales of 3 days or less (Elliott et al., 1978). Sea level height has a dominant fluctuation of 20 days, with a 5 day Ekman effect fluctuation and a 2.5 day longitudinal-wind driven seiche oscillation also observed (Elliott et al., 1978). Winds are mostly episodic, but the preferred direction varies seasonally. Northwesterly winds are more common in November-February, whereas Southerly winds occur more often in the spring and summer. Because of the

salt wedge structure of the Chesapeake it is stratified for most of the year, but extreme winds in the fall can destratify the Bay (Goodrich et al., 1987).

Blumberg (1977a, 1977b) used a two-dimensional, depth averaged model to study the dynamical balance and eddies in the Chesapeake. A three-dimensional hydrodynamic model, called Curvilinear Hydrodynamics in 3 Dimensions (CH3D), was developed by Wang and Johnson (2000). An implementation of the Princeton Ocean Model (POM) was also used to study the circulation of the Bay (Guo and Valle-Levinson, 2008). Both CH3D and the POM implementation overestimated salinities and stratification at depths, especially in the lower Bay. Li et al. (2005) applied the Regional Ocean Modeling System (ROMS) to the Chesapeake Bay to investigate turbulent mixing, stratification events, and tidal energy flux (Li et al., 2006, 2007). That implementation of ROMS produced weaker stratification in high runoff periods and was less accurate under high stratification (Li et al., 2005).

Some of these model errors can be corrected through the use of data assimilation. In this study, an advanced data assimilation system has been developed for the Chesapeake Bay Forecast System to improve state estimation. To accomplish this, a ROMS implementation on the Chesapeake Bay has been interfaced with the Local Ensemble Transform Kalman Filter (LETKF). Ensemble data assimilation provides a method for error estimation that can be used to create targeted observations. Here the ensemble spread is used to evaluate the impact of observations in the Chesapeake Bay and to determine areas where more monitoring is needed.

To test the ability of the LETKF-ROMS system to correct the state estimate of temperature, salinity, and currents in the Chesapeake Bay, identical twin experiments were run taking a model run as truth and assimilating simulated observations. This verification, including settings for covariance inflation and method of simulating observations, follows that of R. Hoffman et al. (2008). Using the perfect model framework, we perform sensitivity experiments in varying the observational data coverage to determine how many observations are required to provide an accurate analysis. The metric of ensemble spread, defined as the RMS distance of the ensemble to its mean, has been used to measure the spatial distribution of instabilities and forced errors and for observation targeting (Liu and Kalnay, 2007). Here we calculate the ensemble spread to show areas of the Chesapeake Bay which exhibit the greatest instability and can therefore benefit the most from improved observational coverage.

In these identical twin experiments, what we call the “truth” is a model run beginning on 8 January 1999. The initial conditions were created by spinning up the model for two weeks. Instantaneous snapshots from that spin up run were saved and a random sampling of these model states is used to initialize the ensemble. All observations are generated by taking the truth state, randomly selecting locations, and adding random errors with a preset variance. The locations of observations are randomly distributed both horizontally and vertically and vary for each variable and each time step. Random locations represent the ideal information content for a given number of observations and provide more information than can be expected in reality, but it is a good test of the performance of the filter.

As a reference for the evaluation of the benefit of data assimilation, a simulation is run beginning from the initial background state. This simulation, called the free run forecast, represents the case where only model physics and forcing, and not observational information, impact the forecast.

Analyses were performed every 3 hours using observations of temperature, salinity, and zonal and meridional currents. Initial experiments used a covariance inflation of 9% as in R. Hoffman et al. (2008). While 9% inflation gave good results for a dense data set, when the data coverage dropped to 0.5% or 0.1% a lower covariance inflation value was needed. For experiments presented with 0.5% or 0.1% coverage, 2% covariance inflation was used. Observation errors were set as 0.5°C, 0.6psu, and 0.05m/s. The temperature and current errors are the same as those used by R. Hoffman et al. (2008), while the salinity error is lower than the 1psu used in the same study. Initial experiments used current observations, but later experiments use only temperature and salinity observations because they are more prevalent and reliable in the Chesapeake.

Identical twin experiments using data coverage of 10% are run first to test the system with plenty of observational information. Data coverage of 10% corresponds to approximately 4000 observations per variable, which is more than can be realistically expected. To check the sensitivity of the data assimilation system to observational coverage, experiments were run using identical setups except for varying the data coverage. Beginning at 20% coverage, observational density was then dropped to 10%, 5%, 1%, 0.5%, and 0.1%. Data coverage of 0.1% corresponds

to using about 40 observations per field at each analysis time, which is close to realistic in terms of the average number of observations routinely available.

Even with reduced coverage, the observations at random locations provide more information than is realistic. An observation operator is developed for the system and observations of temperature and salinity are simulated in a realistic spatial distribution. To complete the identical twin experiments, real observational data is read into the system and temperature and salinity observations are simulated at real locations and the correct time window.

The Model

For the model, we use the ChesROMS implementation of the ROMS model with a reduced vertical grid. ChesROMS uses a curvilinear grid with a 100x150 horizontal mesh and 20 vertical levels. ROMS is a free surface, primitive equation model that utilizes a terrain following sigma coordinate in the vertical. For the assimilation experiments presented here, the vertical resolution was reduced to 10 levels to reduce the computational cost. Only the physical part of the model is used here for data assimilation. A full description of the numerics can be found in Shchepetkin and McWilliams (2005). Time integration is split into internal and external modes for surface elevation, currents, and salinity. Bathymetry data for ChesROMS comes from the US Coastal Relief Model at NOAA's National Geophysical Data Center (NGDC) (**Fig. 3.1**).

ChesROMS is forced from three main areas: the open ocean boundary, fresh water river discharge, and the air-surface interface. The open ocean boundary is prescribed using nine tidal constituents from the ADCIRC model and non-tidal water

levels from the National Oceanic and Atmospheric Administration's (NOAA) National Ocean Service program. These components are the same as used by Li et al. (2005). For the barotropic component, Chapman's condition for surface elevation (Chapman, 1985) and Flather's condition for barotropic velocity (Flather, 1976) are employed. For the baroclinic component, a radiation condition is used for velocity along with nudging to climatology from the World Ocean Atlas 2001 (WOA01) for temperature and salinity (http://www.nodc.noaa.gov/OC5/WOA01/pr_woa01.html). A k- ω turbulence closure is used.

Daily freshwater river discharges are prescribed from the United States Geological Survey (USGS) stream water monitoring project for 9 tributaries. Forcing at the air-surface boundary—such as 3-hourly winds, net shortwave and downward longwave radiation, temperature, relative humidity, and pressure—are given by the National Center for Environmental Prediction (NCEP) North America Regional Reanalysis (NARR). More information on ChesROMS, including the open source code, can be found at <http://sourceforge.net/projects/chesroms>.

In comparing hindcasts from 1991 to 2005 with observations of water level, temperature, salinity, and currents, Xu et al. (2009) found that the model reproduced the tidal propagation and accurately captured the variability of all of the studied fields. Some model deficiencies were found, including errors in upper Bay water level, insufficient currents in the lowest layers, and lower modeled salinities in the upper Bay.

LETKF Code Setup

The LETKF code of Dr. Eric Kostelich (personal communication, 2007) was modified by Dr. Ross Hoffman to work with ocean models taking into account bottom topography and coastlines, among other issues (R. Hoffman et al., 2008). Both the LETKF and ChesROMS model are treated, as much as possible, as black boxes, so FORTRAN and C-Shell interface scripts were developed to run the coupled LETKF-ChesROMS system.

Identical Twin Experiments

Experiments with 10% Data Coverage

In the perfect model experiments, the LETKF quickly reduces both the analysis and forecast errors below the specified observational errors (**Fig. 3.2a**). Moreover, the errors continue to decrease and remain below the observational errors for the duration of the simulation. At 10% data coverage the analysis error in temperature quickly converges to less than the observational error in around 6 hours. After about a week, the system appears to have spun up and the error remains low with only a few oscillations due to instabilities in the system. By comparison, the error in the free run forecast doesn't drop below the level of the observational error until around 16 days. The free run forecast in the Chesapeake Bay does show significant error reduction over time (**Fig. 3.2a**), which is a much different behavior than in the atmosphere. The decrease in the free run error over time indicates that forcing is a dominant factor in the evolution of the Bay and the system is more stable than chaotic.

Dependence on Data Coverage

All of these data coverages exhibit an initial, significant decrease of RMS error to below the observational error level within the first two days (**Fig. 3.2b**). Not surprisingly, as the data coverage decreases, there is degradation in the quality of the analyses. While 20%, 10%, and 5% data coverage yield very similarly accurate results, there is greater error using 1% data coverage and a still larger error for 0.5% and then 0.1% data coverage.

Even with 0.1% data coverage, however, the LETKF still significantly improves the forecast. Although the analysis error is larger than in the case of more complete data coverage, the LETKF still reduces the analysis error to below the observational error in about 30 hours—a significant improvement from the free run forecast.

Observation Targeting Using Ensemble Spread

In addition to providing more accurate nowcasts and subsequent forecasts, the fact that the LETKF characterizes the uncertainty can be exploited to target observations. The LETKF describes the uncertainty using the measure of ensemble spread, which is the root mean squared distance of the background ensemble members from the ensemble mean. Ensemble spread is a reasonable approximation of the error and areas of large ensemble spread correspond to areas of large error. Spikes can be seen in the temperature RMS error in **Figure 3.2a**. These spikes occur when the wind forcing shifts so that the winds point directly up the mouth of the Chesapeake in combination with a strong tidal cycle. This forcing drives a warm plume up the Bay mouth and causes temperature errors in the upper levels of the

model. The ensemble spread is able to accurately capture the spatial pattern and location of these errors, although it underestimates the size of the error (**Fig. 3.3**).

The fact that the ensemble spread accurately represents areas of large forecast error can be exploited to target observation locations that will be particularly beneficial to the analysis. To demonstrate this potential in an idealized experiment, assume that there exists an instrument, such as a high resolution satellite, which is able to take one surface temperature observation at any location. At every analysis time, the observation set then consists of the same 0.5% of randomly selected points as was used in the previous experiment, plus one extra surface temperature observation taken at the location of the largest ensemble spread. The result is a global temperature RMS error which is uniformly lower with the one added observation than without (**Fig. 3.4**). Moreover, the largest increase in accuracy with the additional observation is during the wind forced warm plumes when the temperature error spikes. Only one observation was added out of approximately 300, but the resulting impact was large.

While such an idealized satellite is unrealistic, it is an instructive example of how the ensemble spread can be used to advise observing missions. A more realistic observing mission is one that changes location not every analysis time, but every season. Such an instrument has been discussed in the Chesapeake observing community. To investigate where this type of instrument would provide the greatest benefit to the Chesapeake forecasting problem, perfect model simulations are performed in April, July, and October to complement the January experiment that was described above.

The spread in temperature shows a distinct seasonal cycle. In January, the average ensemble spread is greatest in the tributaries of the Chesapeake, particularly the Patuxent, York, Rappahannock, and Choptank Rivers as well as the upper Potomac (**Fig. 3.5**). There is also large ensemble spread in near the mouth of the Bay and out into the open ocean. As a percentage of the monthly averaged temperature, however, the spread in the rivers is more significant due to the colder winter temperature in the shallow river basins. During winter the river discharge has large variability due to ice and snow melt, which may account for the large spread in the tributaries.

Ensemble spread in the tributaries is decreased in April and spread in the lower Bay and open ocean is increased (**Fig. 3.5**). In July, large values of ensemble spread are concentrated in the lower Chesapeake from the Bay mouth up to the Rappahannock River. In addition, patches of large ensemble spread are present in the western Bay between the mouths of the Potomac and Patuxent Rivers and just north of the Patuxent (**Fig. 3.5**).

In October, the largest patch of high ensemble spread is in the eastern part of the lower Bay, but the magnitude of the spread is significantly smaller than in January, April, or July (**Fig. 3.5**). Areas of high ensemble spread can also be seen in the lower Rappahannock and York Rivers during October. The fact that there is large ensemble spread in the lower part of the Bay year-round suggests that this region has more interesting dynamics than the remainder of the Bay. This is reasonable because this region is the widest and deepest part of the Chesapeake.

Salinity ensemble spread, like that of temperature, is particularly large in the tributaries of the Bay during January (**Fig. 3.6**). All of the seasons show high spread in the upper York River, but in January there is an increase in ensemble spread in the upper Potomac and Rappahannock Rivers as well. In October, a patch of high salinity spread is visible in the upper Bay at the mouth of the Miles River (**Fig. 3.6**). This location has noticeable spread during the entire year, but it is more pronounced during the fall.

Throughout the year there is large ensemble spread near the mouth of Chesapeake, although the spatial distribution of the spread varies. In January, the largest values of ensemble spread point from the mouth of the Bay directly up the main channel of the Bay, with slightly less spread at the southernmost point of the Bay and near the mouth of the James River (**Fig. 3.6**). By the summer, there is very little spread near the mouth of the James River and the largest spread is concentrated along the eastern side of the main channel (**Fig. 3.6**). The opposite is true in October, as the highest values of ensemble spread stretch along the southern edge of the Bay from the Bay mouth up into the lower James River. Spread in salinity at the mouth of the Bay is lowest in October, when the salinity distribution is more homogeneous due to mixing and decreased river discharge (Valle-Levinson and Lwiza, 1997).

Higher salinity spread is also present year round in the outflow plume of the Chesapeake Bay. Mean daily river discharge is greatest in March and April, so the outflow plume is strongest in April and May (Valle-Levinson et al., 2007). The stronger plume can be seen in the April ensemble spread, as the spread is higher and extends farther into the open ocean. Similarly, the outflow plume is weakest in

September to November after the August minimum in river discharge (Valle-Levinson et al., 2007). This is reflected in the smaller values of ensemble spread in October.

Realistic Observation Distribution and the H Operator

Using simulated observations at randomly selected grid points is an excellent way of debugging, testing, and studying the properties of an assimilation system. In the experiments described above, observations were simulated at a fixed percentage of random chosen grid points and the grid points containing observations varied during each assimilation time and were evenly distributed through the water column. The use of a random sampling derives maximum information from an observation set. In practice, many observations come from buoys which have a fixed location and do not take observations at regular intervals. In addition, most of the observations are taken near the surface of the Bay or at one or two deeper levels. The result is an observation set that is significantly less evenly distributed both spatially and temporally than the randomly generated observations. Furthermore, the previous experiments assimilated current information, but these observations are scarce in practice.

Observations in the Chesapeake Bay come from a number of different groups, such as the Chesapeake Bay Observing System (CBOS) and the Chesapeake Bay Program (CBP). Each of these observational data sets will now be described. The CBOS program consists of six stations throughout the bay. Two of the CBOS stations take observations of the current in the mid bay, three take salinity observations, and three take temperature observations. CBOS stations report real-

time data every 6 to 30 minutes, depending on the station. In 1999, only two CBOS stations were operational at some part of the year. CBOS stations have also experienced technical difficulties at times and all six stations are not currently producing data.

The CBP has over 100 stations around the bay, with about 40 of these in the main part of the bay. CBP stations collect profiles of both temperature and salinity. Unlike CBOS, however, the CBP stations are not read continuously and data is read at irregular intervals ranging from 10 days to a month or longer. The time distribution of CBOS and CBP observations between 10 January 1999 and 14 February 1999 is shown in **Figure 3.7**. During many 6-hour analysis windows, the CBOS observations are the only available observations, while the addition of CBP observations adds over 100 observations in some windows. There is also an over 2 week period from 22 January to 7 February where no CBP observations are available. The frequency of observations is season dependent, with more frequent observations between spring and fall and larger observation gaps in the winter. The spatial distribution of the CBOS and CBP station locations can be seen in **Figure 3.8**.

CBOS and CBP observations are the primary data sets used for validating and tuning ChesROMS, but other observation sets exist or are in development. The Virginia Institute of Marine Science (VIMS) at The College of William and Mary has a number of stations in the Virginia portion of the Chesapeake Bay. VIMS runs the Virginia Estuarine and Coastal and Coastal Observing System (VECOS), which consists of five continuous data stations and thirty-one fixed stations that record physical and water quality variables (<http://www2.vims.edu/vecos/default.aspx>). All

of the VECOS stations are located in the tributaries of the Bay. Another interesting and potential source of observational data is the use of CODAR high-frequency radar to determine currents and wave speeds near the mouth of the Chesapeake Bay. This project—which is undertaken through Old Dominion University—could provide valuable current observations for assimilation in the lower Bay (<http://www.ccpo.odu.edu/currentmapping/>). Another potential source of data is satellite observations, which, with improved resolution, could provide a few observations of each pass over the Chesapeake. MODIS currently takes ocean color observations that can be used in the Chesapeake Bay region and takes SST data as well (<http://coastwatch.noaa.gov/cwn/search/interface.html>). The NOAA-16 and NOAA-18 satellites also take radiances from which SST can be derived.

The station observations are all at fixed locations, but the locations are not on the grid points as was the case in the previous simulated observation experiments. This necessitated the development of an H-operator for the LETKF-ChesROMS system. The ROMS system already contains an interpolation package that allows it to interpolate to observation locations for the purpose of model validation. The package uses simple linear interpolation in both the horizontal and vertical directions. The interpolation code from ROMS was modified to integrate with the LETKF system and create the H-operator.

To test the performance of the H-operator and the ability of the LETKF to correct fields with stationary, unevenly distributed observations, identical twin experiments were run using observations of temperature and salinity simulated at the surface of the bay at the locations of all CBOS and CBP stations. For the purpose of

this experiment, only the location of the station was used and not the real time distribution of the observational data nor the real observed fields. Instead, it was assumed that all stations take observations at every assimilation time in both temperature and salinity (**Fig. 3.8**). The initial improvement with these observations is very good in the main stem of the Bay, with larger analysis errors in some of the tributaries and in the open ocean (**Fig. 3.8**).

Using these observations, the analysis improvement still exhibits the same characteristics as the assimilations with random observations distributed through all levels. There is a sharp reduction in the both analysis and forecast RMS error in temperature, with the error level dropping below the observational error within a day and remaining low (**Fig. 3.9a**). Moreover, similar improvement is seen in salinity (**Fig. 3.9b**). Even though no current observations were assimilated, the LETKF corrects the currents based on the temperature and salinity observations, which leads to improvement in the current fields as well (**Fig. 3.10a** and **Fig. 3.10b**).

Realistic Temporal Observation Distribution

The previous experiment demonstrates that the LETKF is able to correct errors using observations in realistic locations and analysis times. As discussed above, the temporal distribution of the observations is very non-uniform and further thins the available observations at a given analysis time (**Fig. 3.7**). A more realistic experiment was run where the CBP and CBOS station data in the analysis window was read into the system and observations were simulated at the real locations. To accomplish this, a C-shell script was written to pull all of the observational data from a given time window together into a single file. FORTRAN code was then created to

read this file in and replace the value of the measurement with the simulated value.

One advantage of this code structure is that it is a relatively simple step to transition to assimilating full real observations.

Initially, using the same parameters as in previous experiments, the analysis would blow up after a week of improvement. It was found that the problem was that the ensemble was diverging in the open ocean (**Fig. 3.11a**) where there are no observations. Even using a localization radius of 20 grid points was not enough to constrain the open ocean. In order to correct this, the localization was enlarged in the lower part of the model. A localization radius of 60 grid points was used in the first 12 latitudes, which contain only open ocean grid points. For the remainder of the open ocean latitudes (from model latitude 13 to 36), a localization radius of 40 grid points was used. The rest of the Bay used a localization radius of 20 grid points. With this localization, the ensemble spread is no longer seen to diverge (**Fig. 3.11b**).

The analysis using this new localization shows significant improvement over the free run forecast (**Fig. 3.12**). Unlike the previous experiments, the global RMS error in temperature decreases in steps rather than a sharp initial drop. This behavior is due to the number of observations at a given analysis time. For the first day of the simulation, only CBOS observations are assimilated and the analysis is seen to slowly improve. During 11 January 1999, the number of observations spikes due to the CBP data and the analysis improves significantly. Two more sharp analysis reductions are seen coincident with the infusion of CBP data before the global analysis RMS error asymptotes after approximately 5 days (**Fig. 3.12**). A similar improvement is found in the salinity field as well, with slow initial improvement followed by sharp

decreases in error with the infusion of larger numbers of observations (**Fig. 3.13**). Salinity observations are taken on the same buoys as the temperature observations, so their temporal distribution (**Fig. 3.14**) is similar to the temporal distribution of the temperature observations (**Fig. 3.7**) although the numbers are different.

Globally, the assimilation of spatially and temporally realistic observations significantly improves the estimate of the dynamical state of the Chesapeake Bay. This improvement is not uniform, however, and it is important to investigate which areas receive the largest benefit from the data assimilation. On 11 January 1999, the second day of the simulation, some of the largest errors in the free run forecast are in the tributaries of the Bay, although the entire Bay and open Ocean have large errors (**Fig. 3.15**). The analysis error at the same time is much lower throughout most of the Bay (**Fig. 3.16**). The exception is the eastern part of the middle Bay and the northern Bay. These areas have much larger errors because no assimilations have been performed at these locations. The sharp divide that cuts through the eastern part of the Bay between assimilated and unassimilated regions suggests that the localization for this experiment may not be optimal.

The improvement after assimilation is emphasized by looking at the improvement of the analysis over the free run forecast. The metric used is the absolute value of the free run error minus the absolute value of the analysis error. This gives positive values where the analysis is an improvement over the free run and negative values where the analysis has deteriorated the state estimate. Large improvement can be seen in the majority of locations, although there is no

improvement where there are no observations and there are some areas where the analysis is worse (**Fig. 3.17**).

After 30 days, the free run forecast has improved significantly and the majority of the errors are less than 0.4°C (**Fig. 3.18**). Errors are extremely low in the upper regions of the Bay tributaries, where river forcing is dominant. The largest error in the free run forecast are seen in the widest parts of the main stem and in the open ocean, where forcing does not always trump the internal variability. The analysis at the same time has errors which are below 0.2°C over nearly the entire Chesapeake Bay (**Fig. 3.19**). Larger errors, however, can be seen in the open ocean. The open ocean errors in the analysis state estimate are larger in some places than in the free run forecast, whereas the state estimate of the entire main part of the Bay is greatly improved by the data assimilation (**Fig. 3.20**). Ensemble spread is low throughout the Bay except for areas in the Rappahannock River, the Patapsco River, and the area near the mouth of the Pocomoke River (**Fig. 3.21**). Ensemble spread is much larger in the open ocean, where larger analysis errors were observed.

Summary

The Local Ensemble Transform Kalman Filter was coupled with the ChesROMS model to enable advanced data assimilation in the Chesapeake Bay. To test the system, we ran perfect model experiments with simulated observations. First, a long model run was performed from a set of initial conditions and observed forcing. Then an ensemble of initial conditions was chosen from previous model states and data assimilation was performed every 3 hours using observations created by perturbing the original model run. In addition, a free run forecast is created by

running the model starting from the mean of the initial ensemble states. After only a few assimilation cycles, the analysis errors drop significantly below the observation error levels and asymptote to very small values. The errors in the analysis and subsequent forecast are significantly less than the errors of the free run forecast, which shows that the observations information is being assimilated properly.

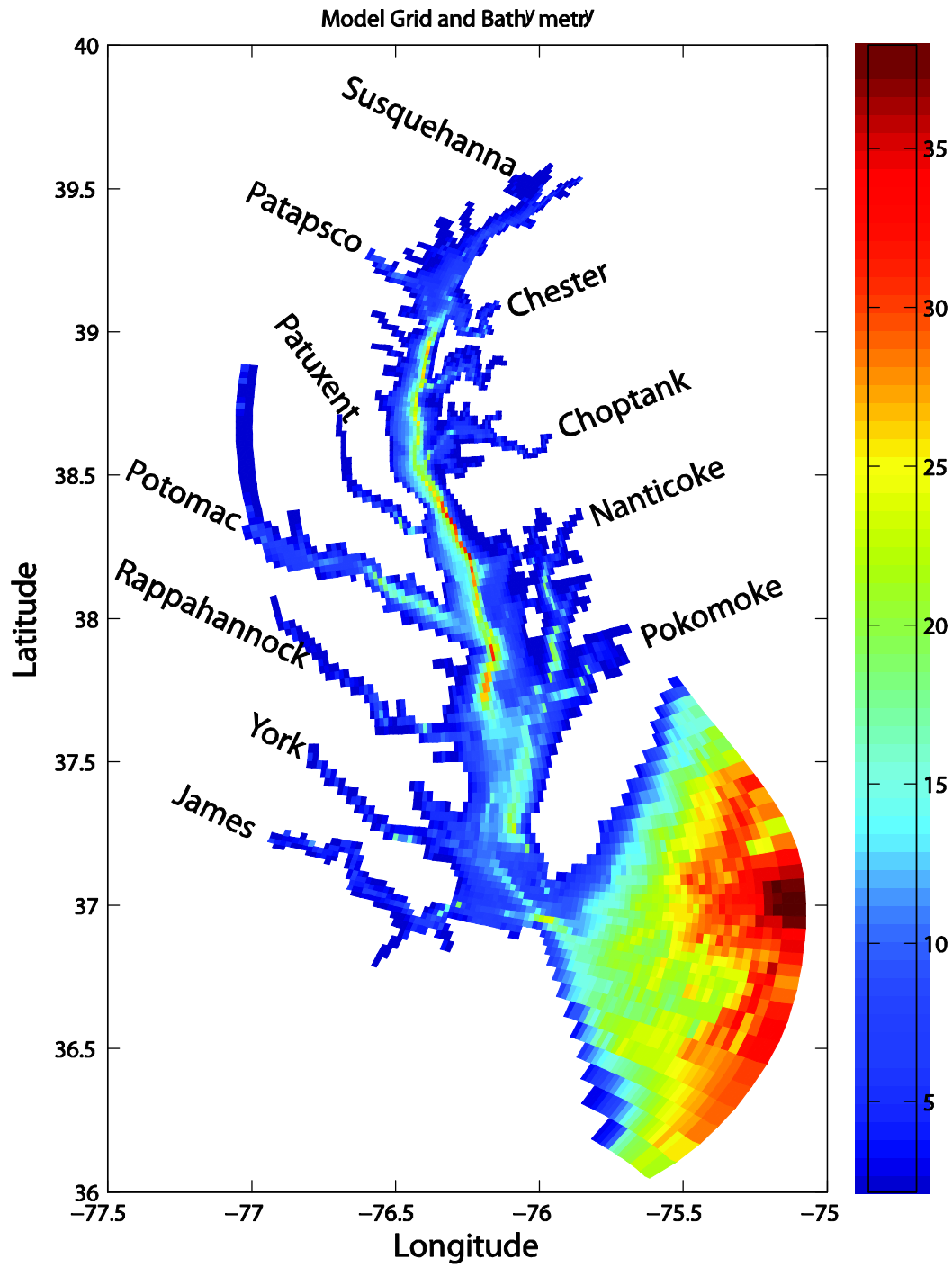
The speed of the error reduction is dependent on the amount of observations used, but even when data coverage is only 0.1% the analysis errors are far below those of the free run forecast and asymptote well below the observation error. This reduction in error is seen using a very small ensemble size. Improvements were seen in the analysis using only 8 ensemble members and the results presented use 16 members.

One useful feature of EnKF methods is that they provide an estimate of the error at each analysis step. We utilize this to determine areas of the Bay and seasons where more observations are needed. First we consider an idealized satellite, which is able to take a temperature observation at each analysis time at the location of maximum ensemble spread. Assimilating just this one extra observation uniformly reduces the analysis error in temperature and shows the greatest reduction in error during spikes in the analysis error caused by a surface forcing driven event.

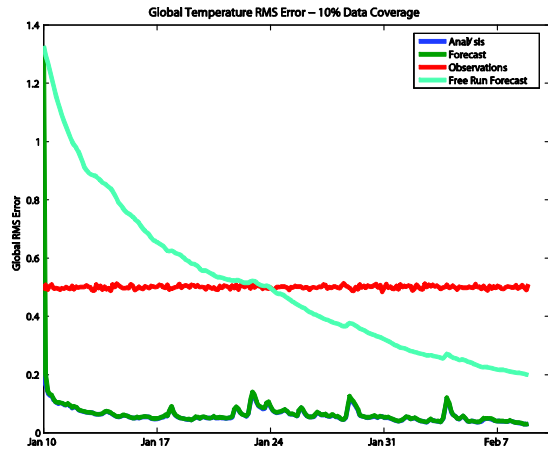
Ensemble spread is also used to investigate the seasonal variability of uncertainty in the Chesapeake Bay. During the winter, the largest ensemble spread in temperature is found in the tributaries of the Chesapeake Bay, whereas by the summer the largest ensemble spread is located in the lower Bay. In the fall and spring, the magnitude of the spread is lower, although there are areas of high ensemble spread in

the lower Rappahannock and York Rivers. These results suggest a mobile instrument that was able to take temperature observations in the rivers during the winter months and move into the lower Bay during the summer has the potential to increase the predictability of the entire Chesapeake Bay system.

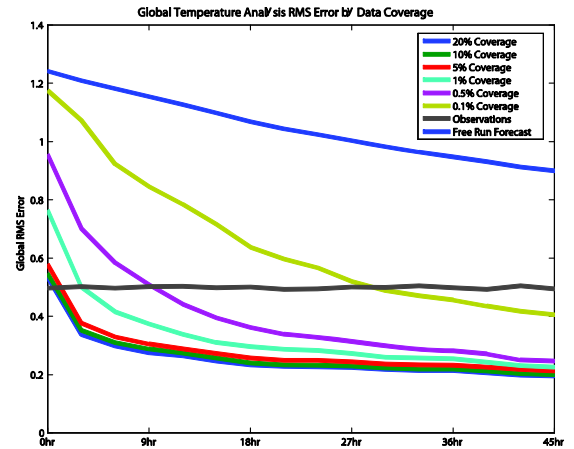
An H-operator based on the ROMS interpolation operator was also developed for the LETKF-ChesROMS system as a first step towards assimilating real observations. This observation operator was tested by simulating temperature and salinity observations at the surface of the Bay at real station locations. Using this observation distribution, the LETKF reduces the global RMS error in the temperature, salinity, and current fields. Observations are also simulated at real observation locations and correct analysis times and the LETKF is found to improve the state estimate of the Chesapeake Bay. This is a very promising result for moving towards assimilating real observations.



3.1 Model bathymetry in meters along with the names of major rivers.

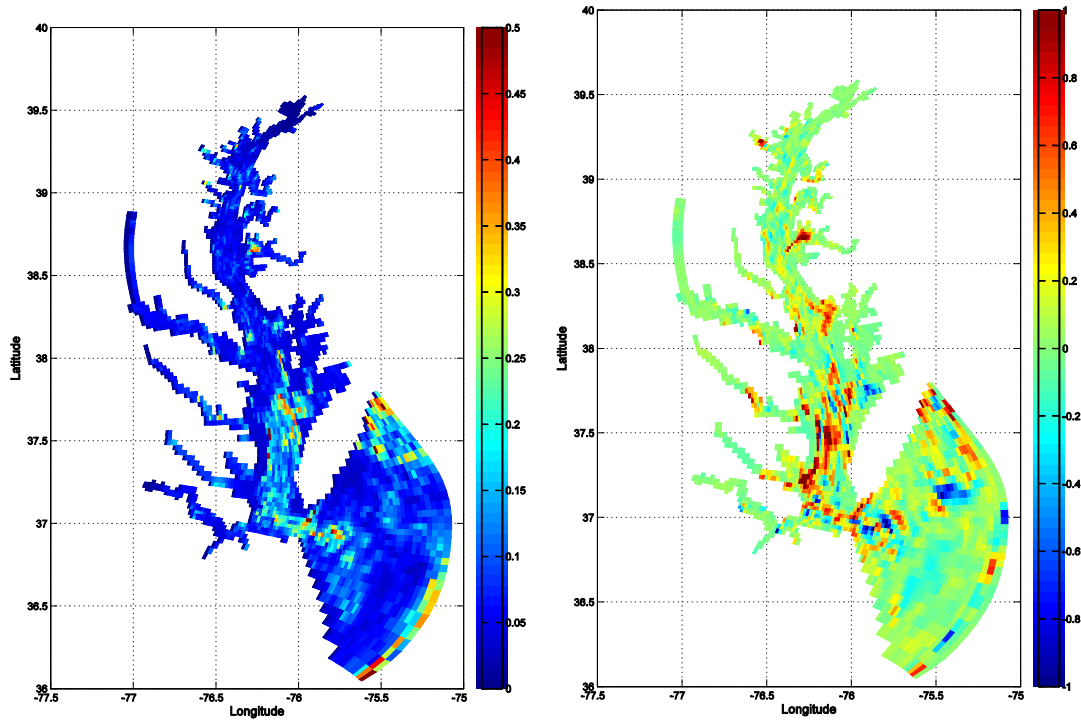


(a)



(b)

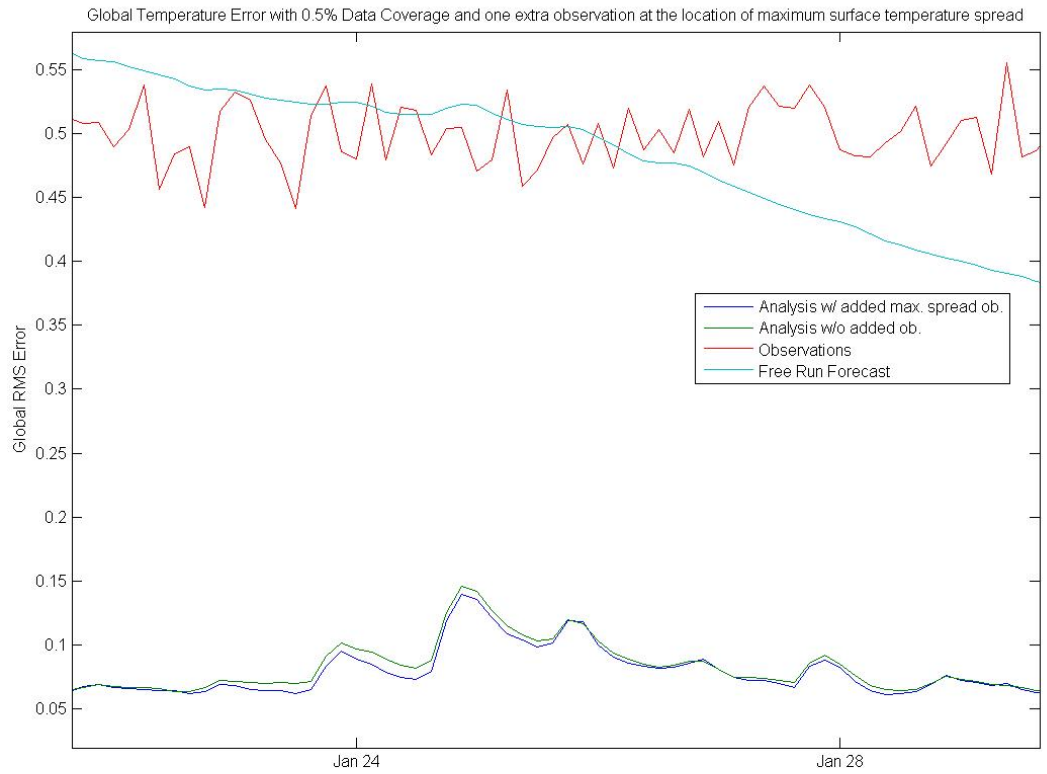
3.2 Global RMS temperature error [C] from 10 January to 9 February 1999 (a) from an identical twin experiment using 10% observational data coverage and 9% inflation and (b) with varying data coverage in identical twin experiments using 9% inflation and a 16 member ensemble.



(a)

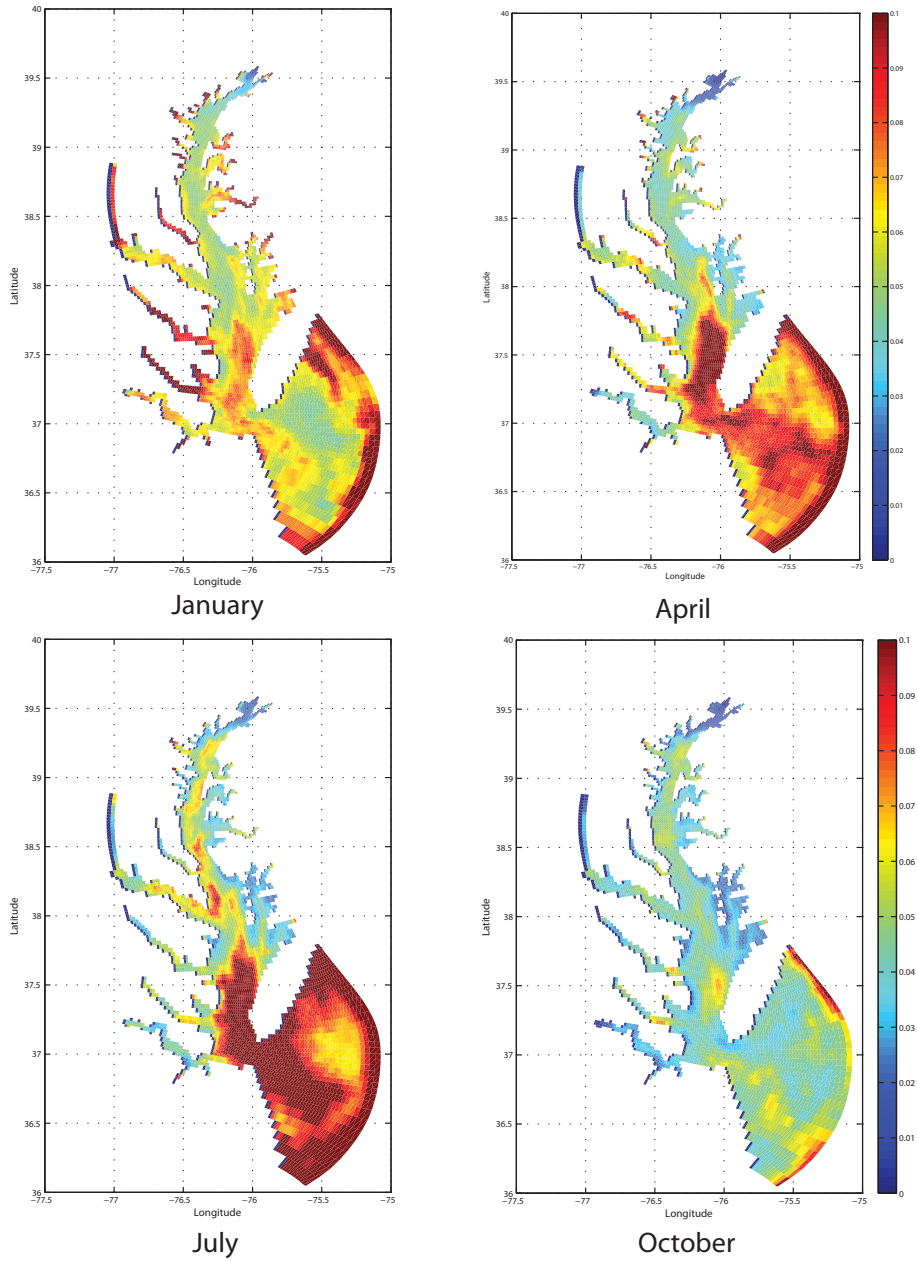
(b)

3.3 (a) SST ensemble spread on 20 January 1999 during a spike in global temperature RMS error (see Fig. 3.1) caused by an event where surface winds are pointing into the Bay and pushing warm water up the mouth of the Bay. (b) Forecast error on 20 January 1999. Note that the error in the lower Bay is captured by the ensemble spread in **Fig. 3.3a**, but the magnitude of the spread is several times smaller than the error.



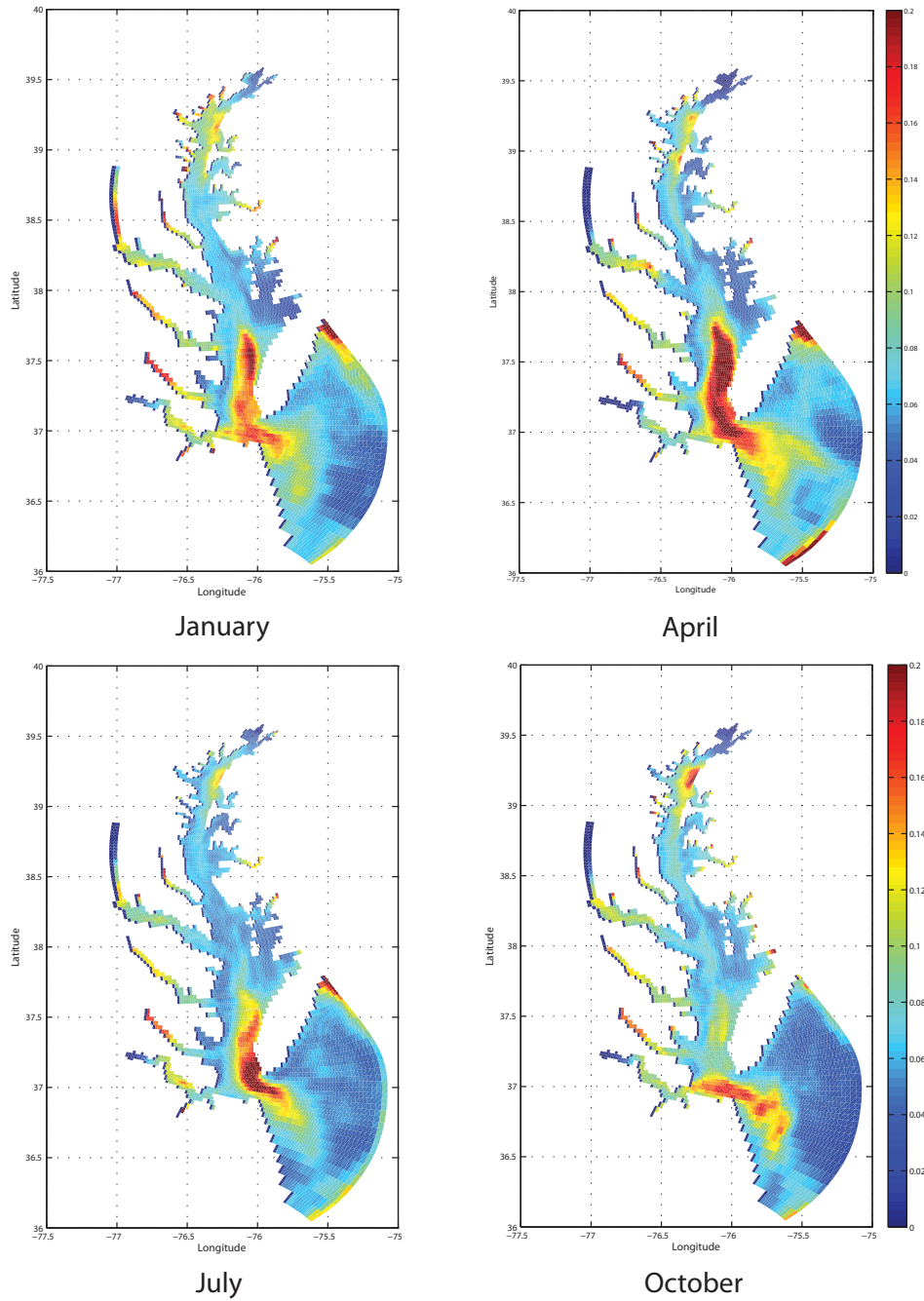
3.4 Comparison of global temperature analysis RMS error during the RMS error spike from 23 January 1999 and 26 January 1999 between an experiment using a single observation taken at the maximum SST spread and one without that extra observation. Both simulations have 0.5% data coverage and 2% inflation used throughout. The analysis is uniformly better in temperature over the entire run, but is particularly improved during the times when the RMS error is spiking due to a response to surface forcing.

Monthly Average of Ensemble Spread in Temperature

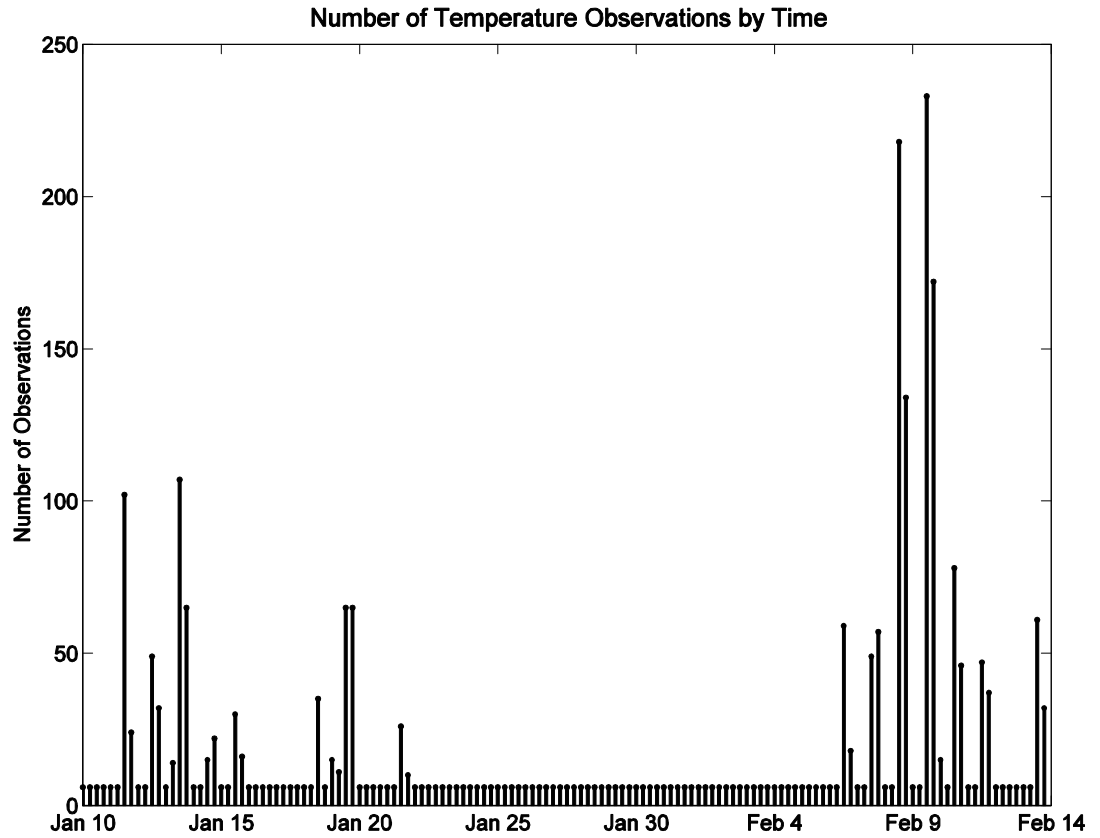


3.5 Average ensemble spread in SST during January, April, July, and October 1999 for experiments using 2% inflation, a 16 member ensemble, and 0.5% data coverage.

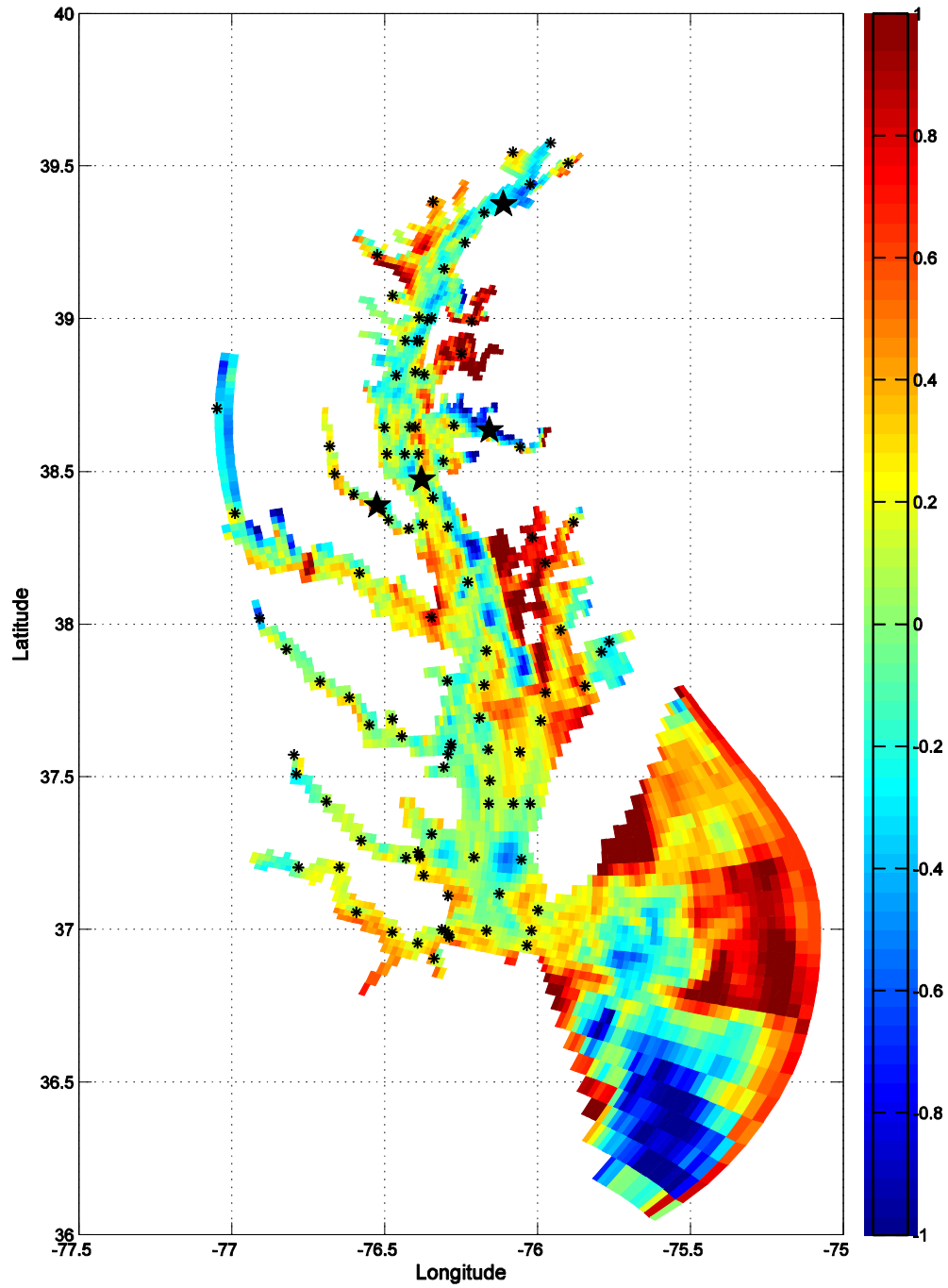
Monthly Average of Ensemble Spread in Salinity



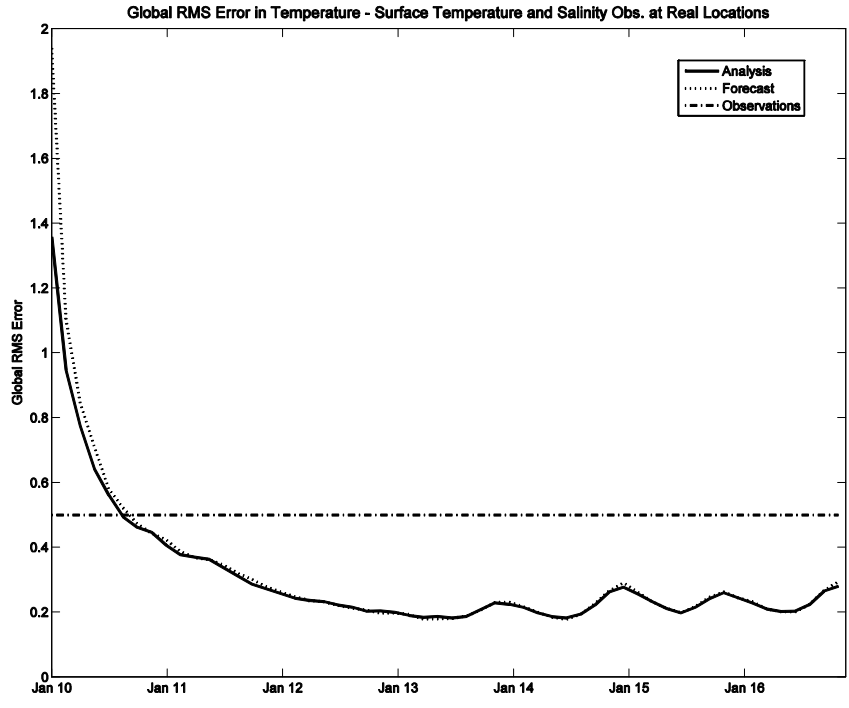
3.6 Average ensemble spread in surface salinity during January, April, July, and October 1999 for experiments using 2% inflation, a 16 member ensemble, and 0.5% data coverage.



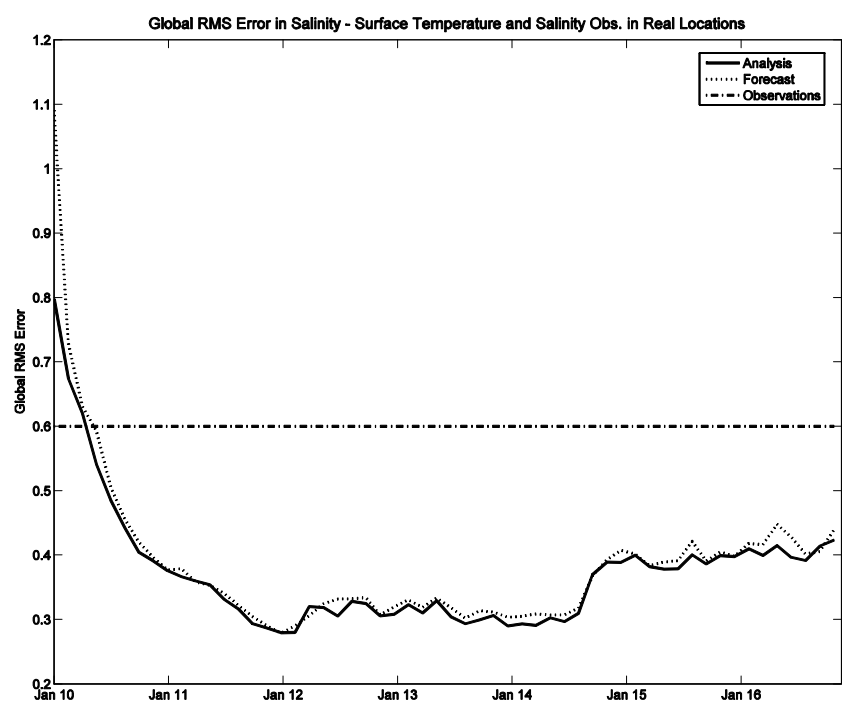
3.7 Number of observations in temperature from CBOS and the CBP during each 6-hour analysis window between 10 January 1999 and 14 February 1999. The same number of CBOS observations is present at every analysis window, so spikes in the number of observations are due to an influx of CBP data.



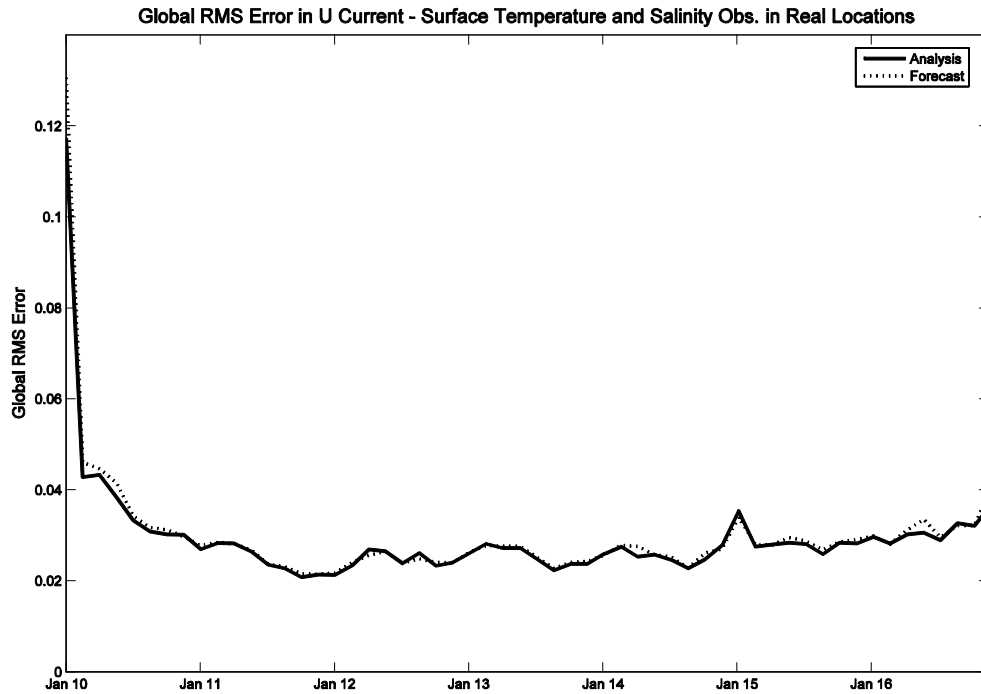
3.8 Locations of CBOS (stars) and CBP (*) observation stations in the Chesapeake Bay are shown in black. The analysis error in SST after the first analysis using only temperature and salinity observations at the surface is shown in the background.



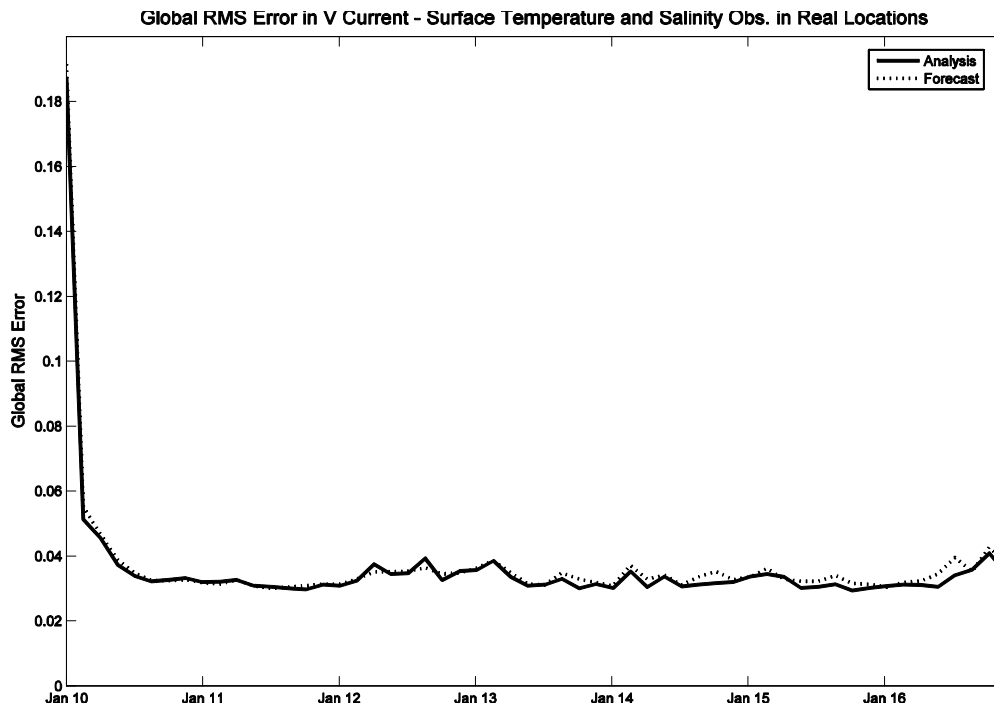
3.9 Global RMS error in (a) temperature from 10 January to 17 January 1999 from an identical twin experiment using simulated observations of temperature and salinity at the surface at real station locations.



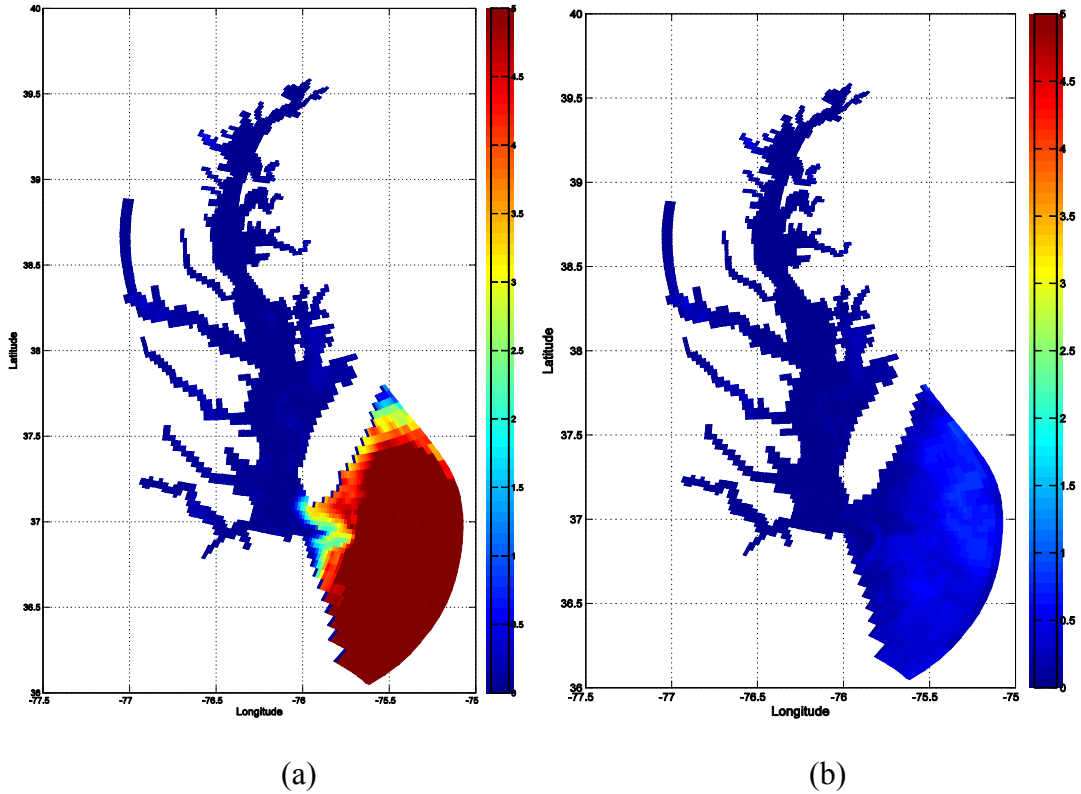
(b) Global RMS error in salinity from the same experiment.



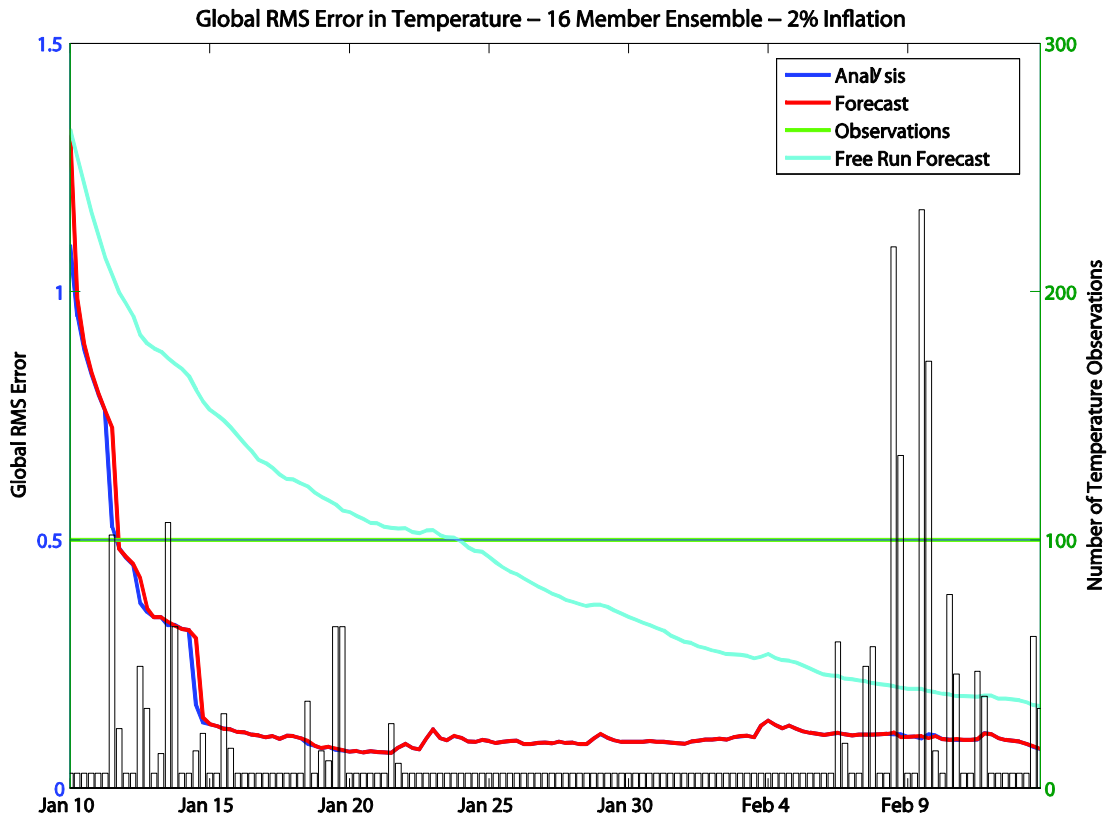
3.10 Global RMS error in (a) the u current component from 10 January to 17 January 1999 from an identical twin experiment using simulated observations of temperature and salinity at the surface at real station locations.



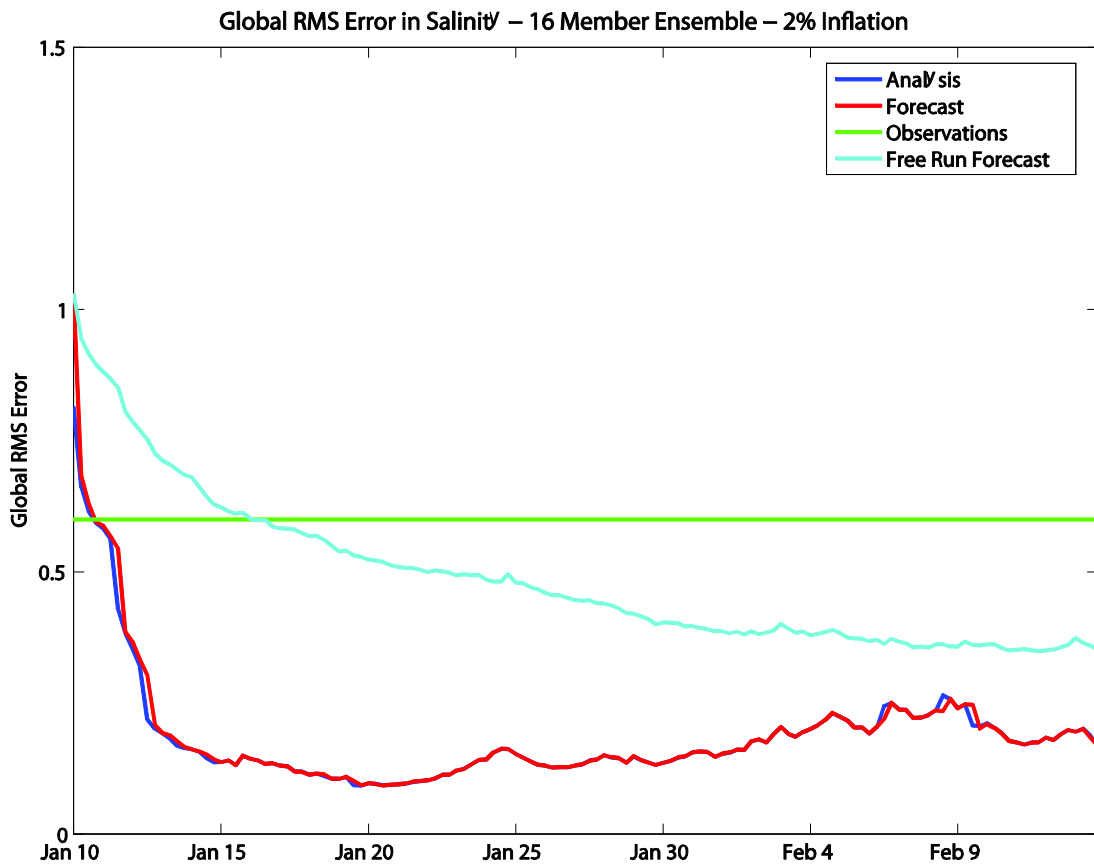
(b) Global RMS error in v current component from the same experiment.



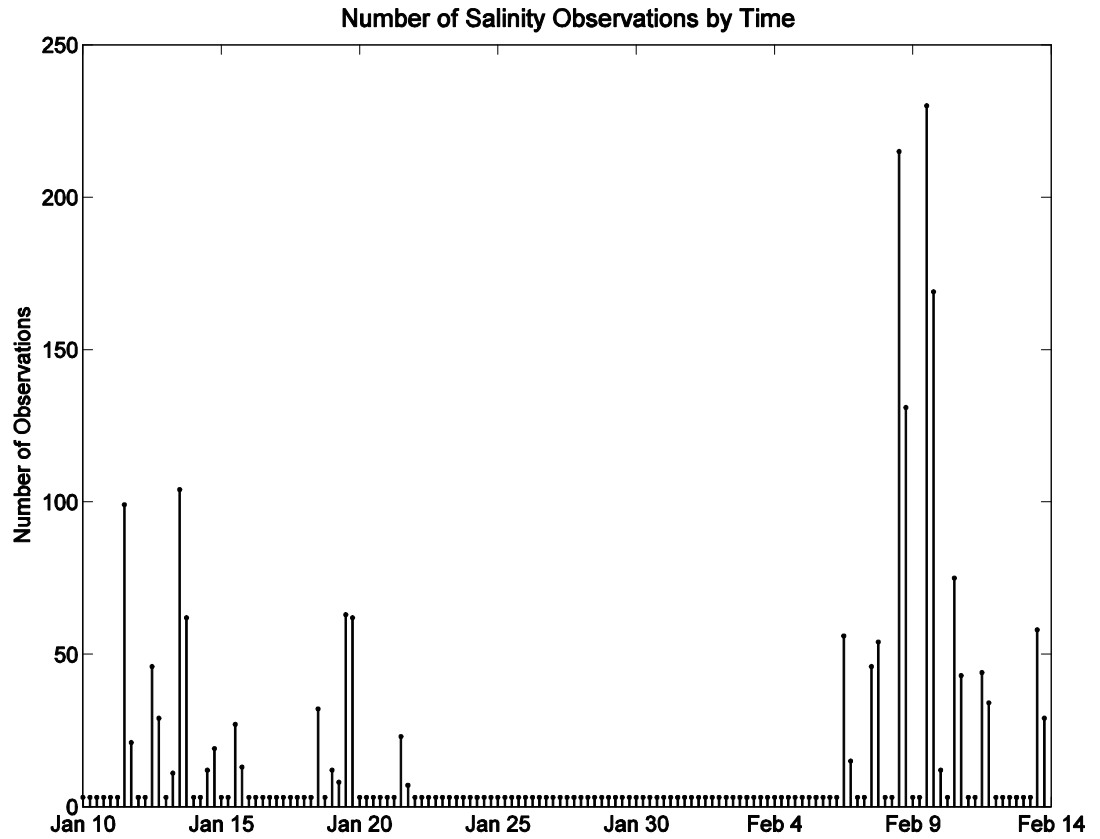
3.11 (a) Ensemble spread in SST [C] on 12 February 1999, 32 days into the simulation using a 16 member ensemble, simulated observations at real locations and assimilation times, and 2% inflation. The horizontal localization used was uniformly 20 grid points. The ensemble can be seen to diverge in the open ocean. (b) Ensemble spread in SST [C] on 12 February 1999 from an experiment with the same parameters except for a larger localization. The localization is 60 grid points below the mouth of the Bay, 40 grid points for the rest of the open ocean, and 20 grid points for the rest of the Bay.



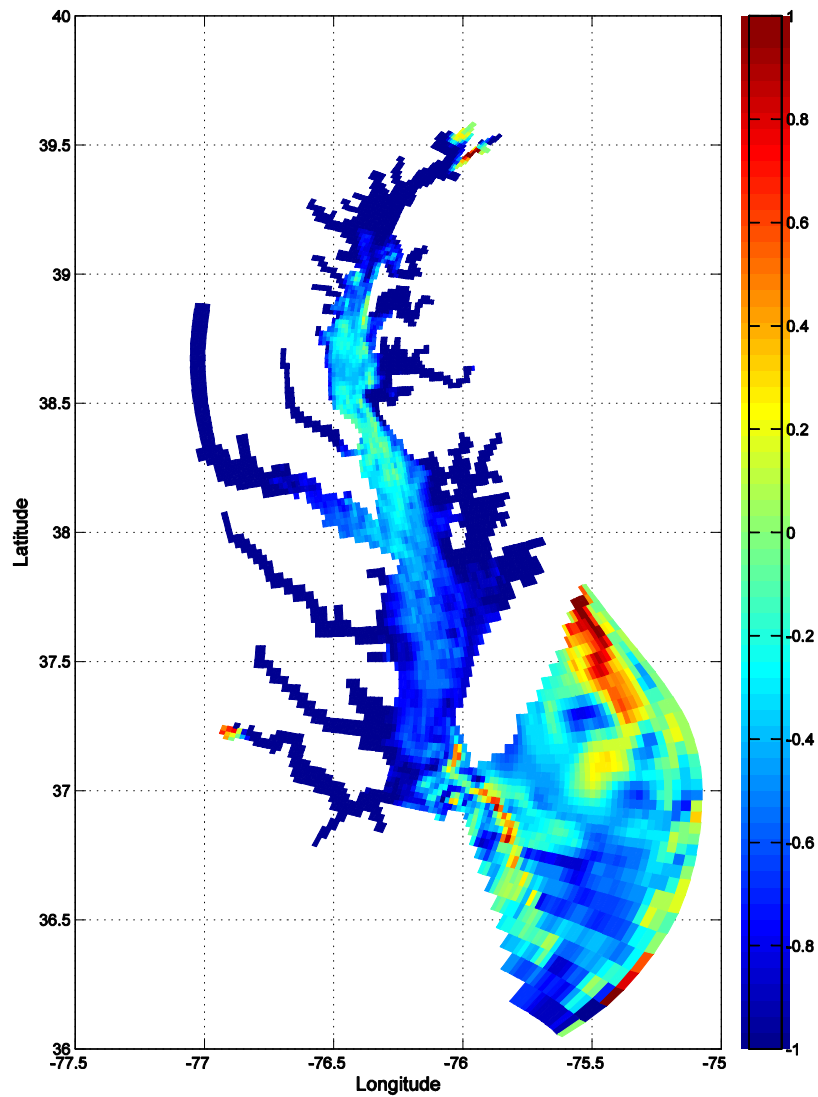
3.12 Global RMS error in temperature for the analysis (blue), forecast (red), observations (green), and free run forecast (cyan) for an identical twin experiment using observations simulated at real assimilation times and locations. The experiment uses 12 ensemble members, 2% inflation, and temperature and salinity observations. The number of temperature observations is shown in the bar graph, which has the same information as **Fig. 3.7**.



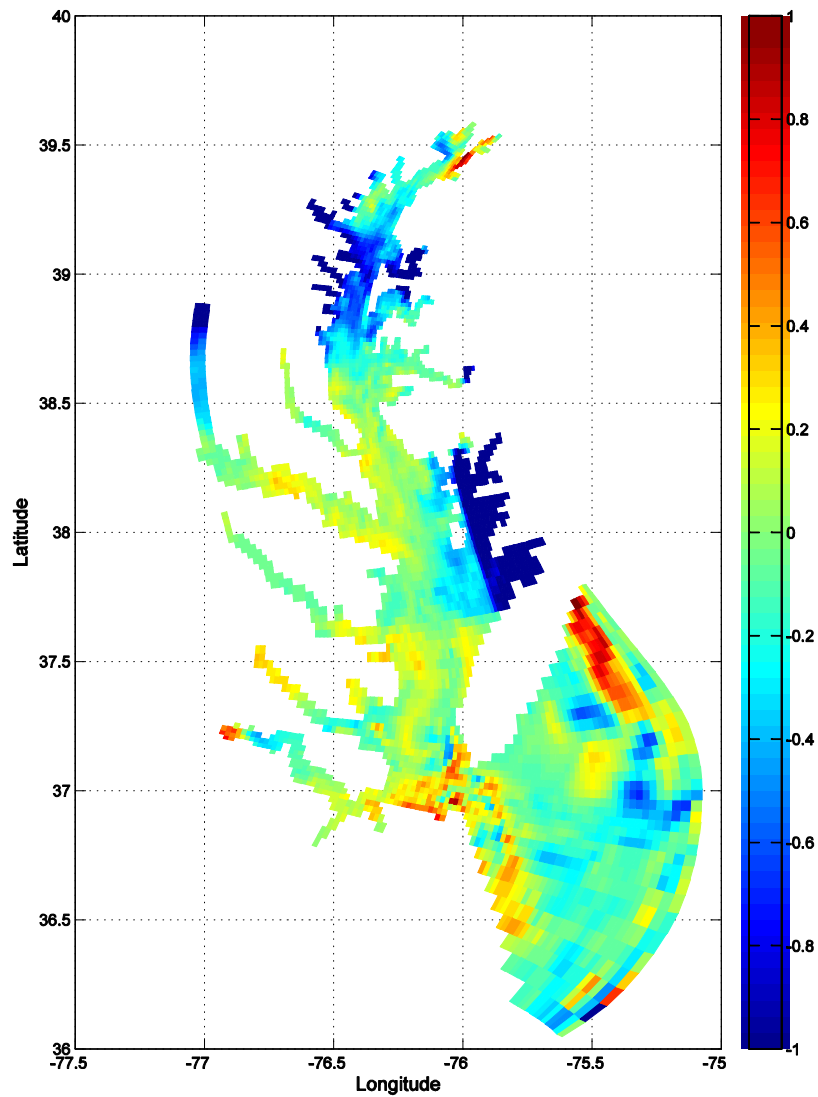
3.13 Global RMS error in salinity for the analysis (blue), forecast (red), observations (green), and free run forecast (cyan) for an identical twin experiment using observations simulated at real assimilation times and locations. The experiment uses 12 ensemble members, 2% inflation, and temperature and salinity observations.



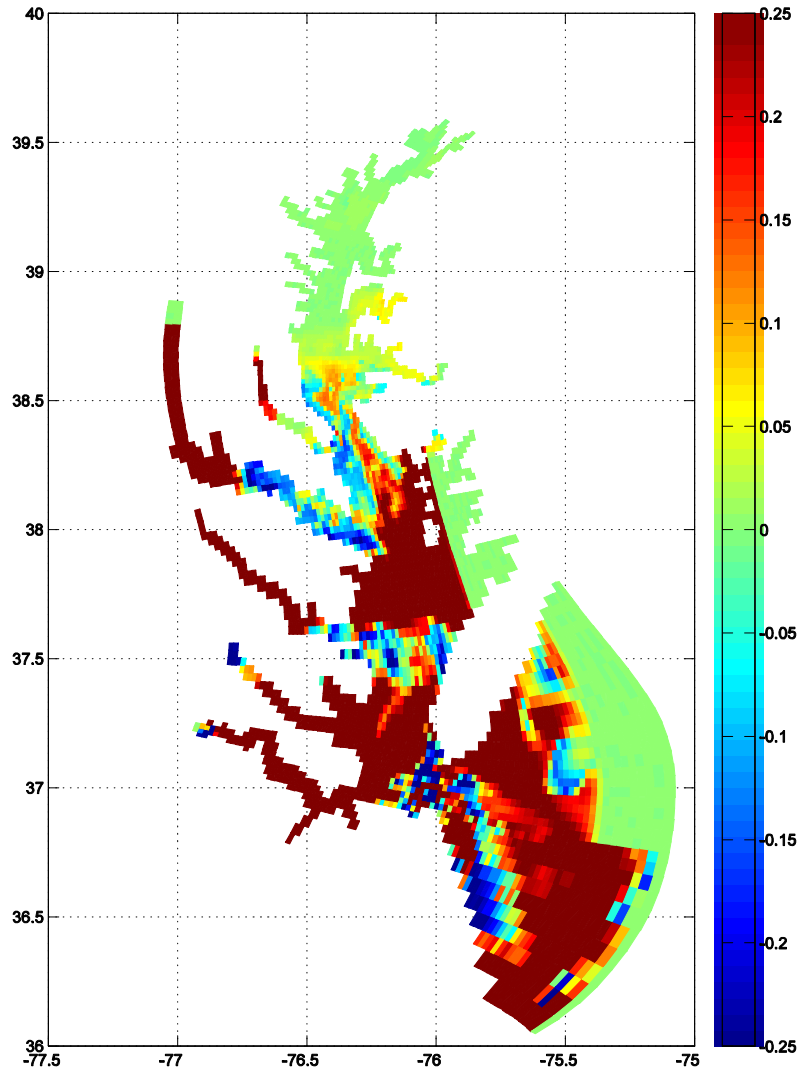
3.14 Number of observations in salinity from CBOS and the CBP during each 6-hour analysis window between 10 January 1999 and 14 February 1999. The same number of CBOS observations is present at every analysis window, so spikes in the number of observations are due to an influx of CBP data.



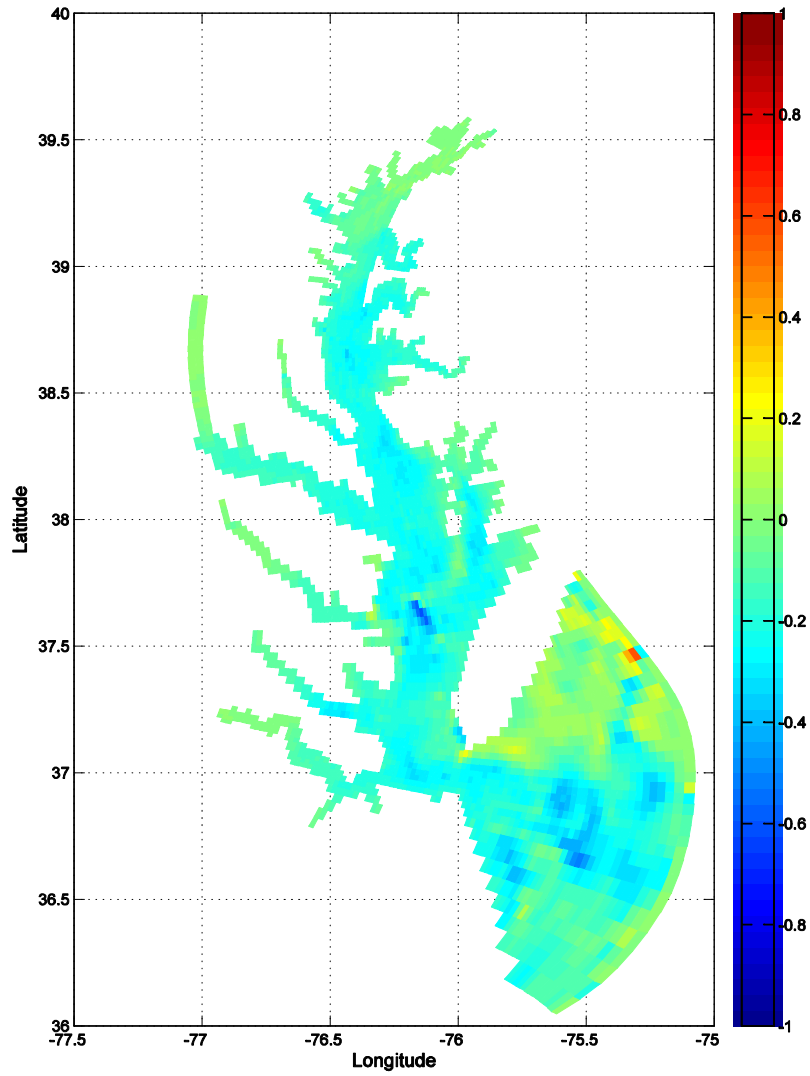
3.15 Free run forecast error in SST [C] at 1200 hours on 11 January 1999, 1 day into the simulation using observations simulated at real locations and analysis intervals, a 16 member ensemble, and 2% covariance inflation.



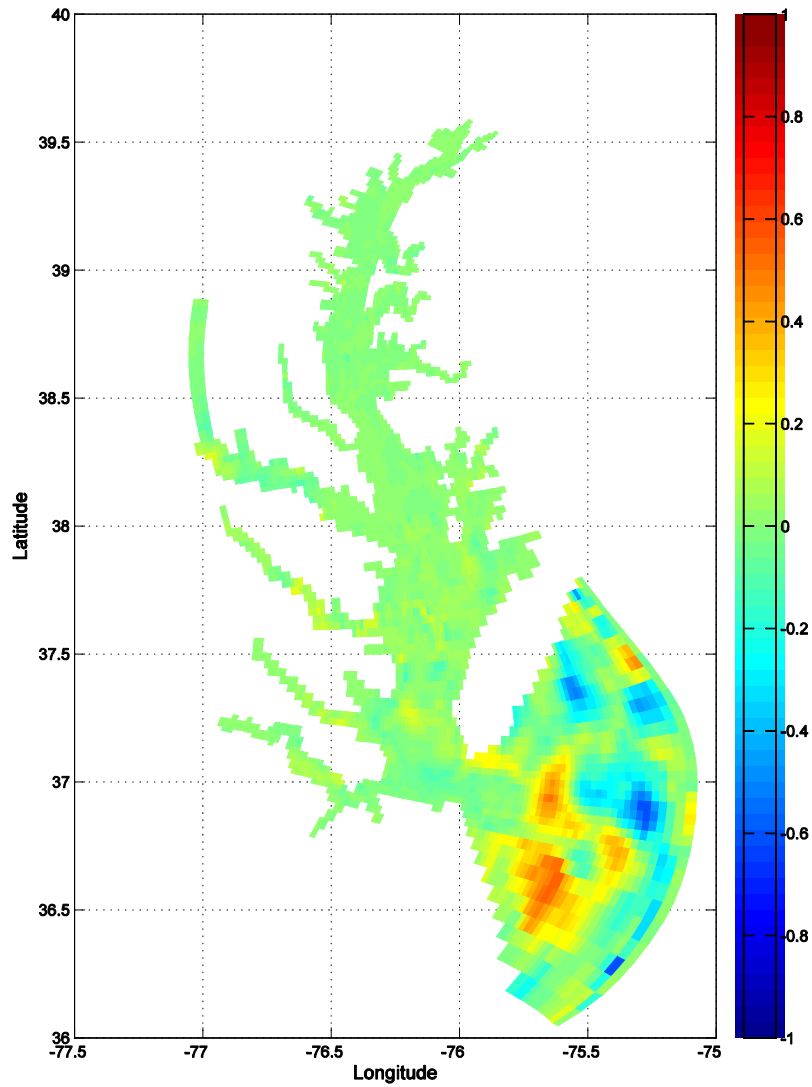
3.16 Analysis error in SST [C] at 1200 hours on 11 January 1999, 1 day into the simulation using observations simulated at real locations and analysis intervals, a 16 member ensemble, and 2% covariance inflation. The darkest blue areas have not yet been corrected by the LETKF.



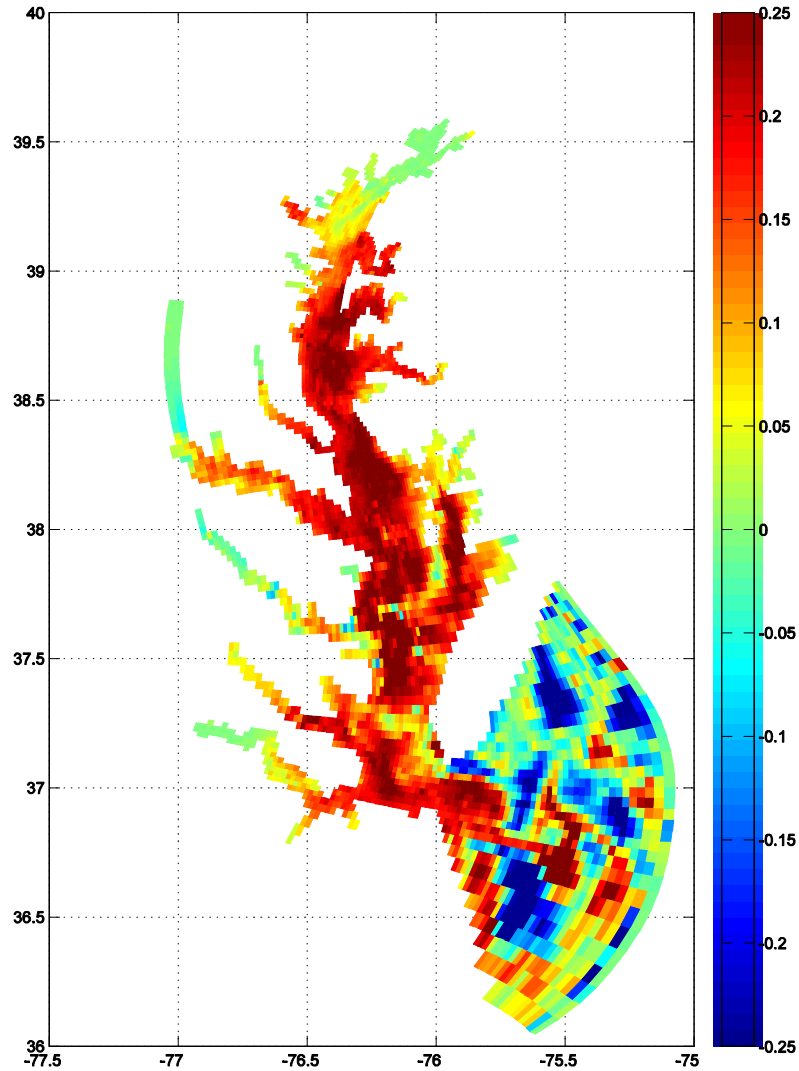
3.17 Improvement of the analysis over the free run forecast, defined as the absolute value of the free run error minus the absolute value of the analysis error, in SST [C] at 1200 hours on 11 January 1999, 1 day into the simulation using observations simulated at real locations and analysis intervals, a 16 member ensemble, and 2% covariance inflation. Positive values (red) indicate areas where the analysis is superior while negative values (blue) indicate that the analysis is less accurate than the free run forecast.



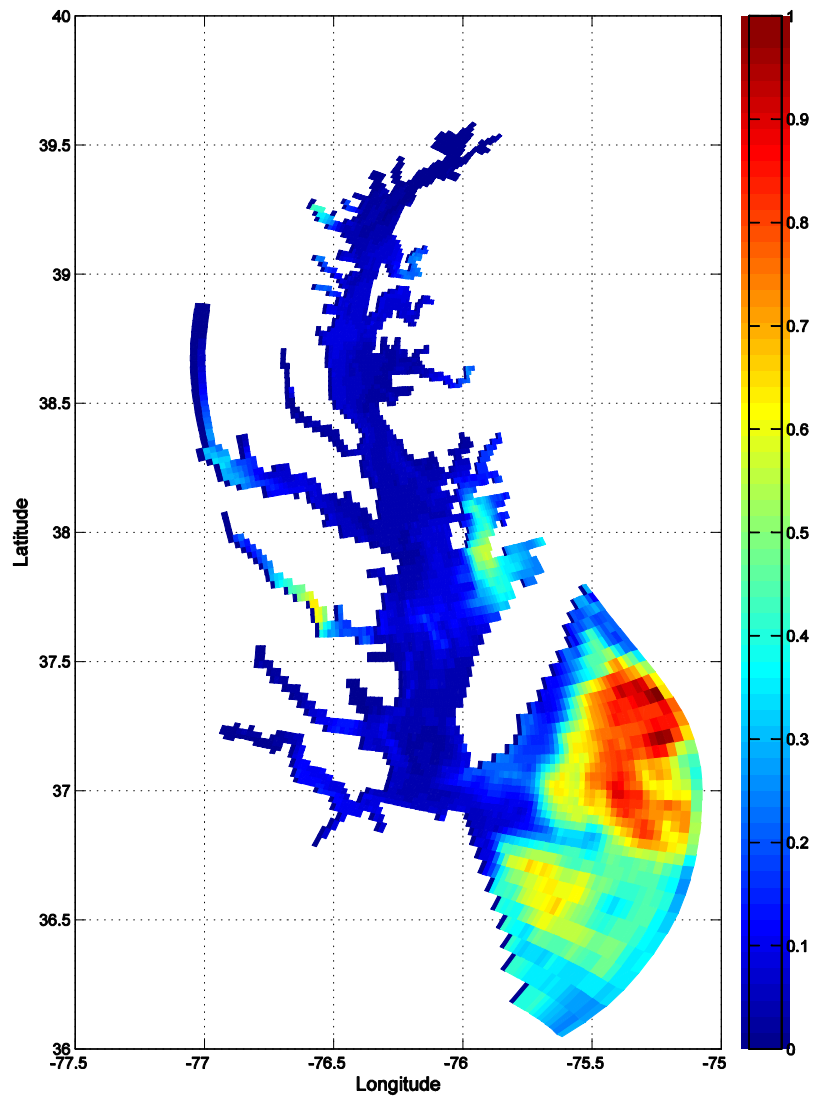
3.18 Free run forecast error in SST [C] on 9 February 1999, 30 days into the simulation using observations simulated at real locations and analysis intervals, a 16 member ensemble, and 2% covariance inflation.



3.19 Analysis error in SST [C] on 9 February 1999, 30 days into the simulation using observations simulated at real locations and analysis intervals, a 16 member ensemble, and 2% covariance inflation.



3.20 Improvement of the analysis over the free run forecast, defined as the absolute value of the free run error minus the absolute value of the analysis error, in SST [C] on 9 February 1999, 30 days into the simulation using observations simulated at real locations and analysis intervals, a 16 member ensemble, and 2% covariance inflation. Positive values (red) indicate areas where the analysis is superior while negative values (blue) indicate that the analysis is less accurate than the free run forecast.



3.21 Ensemble spread in SST [C] on 9 February 1999, 30 days into the simulation using observations simulated at real locations and analysis intervals, a 16 member ensemble, and 2% covariance inflation.

Chapter 4: An LETKF Based Assimilation System for the Martian Atmosphere

Abstract

Ensemble data assimilation has potential advantages for planetary applications. Here a Mars General Circulation Model (MGCM) is coupled with the local ensemble transform Kalman filter (LETKF). Identical twin experiments are performed to explore the potential of data assimilation for the Martian atmosphere. The results show that the LETKF is able to correct errors in the Martian atmosphere and improve the state estimates in the wind fields in the absence of wind observations. This chapter explores the causes of error in the LETKF-MGCM system and finds that large-scale baroclinic waves along the Northern (winter) Hemisphere temperature front and instabilities in the upper atmosphere zonal wind jet are two important sources of error.

Introduction

Due to Mars' similarities with and proximity to the Earth, the circulation of the Martian atmosphere has been actively studied. Mars is the fourth planet from the sun and has a radius of 3.396×10^6 m. Despite having an atmosphere that is 1000 times less dense than that of the Earth, Mars still supports active weather systems including clouds, high winds, and large scale dust storms. Because of its smaller size gravity on Mars is 3.72 m s^{-2} . The Martian day is called a sol and is 88,775 seconds, as opposed to 86,400 seconds on Earth, and the Martian year lasts 686.98 Earth days. The deformation radius, $R = \frac{fa}{N}$, for both planets is very similar (920 km for Mars and

1100km for Earth), which means that both support similar scale storm systems. Because Mars is smaller, however, the storms take up a larger portion of the planet.

The Northern and Southern Hemispheres of Mars have different elevations, with most of the Southern Hemisphere situated on a higher plain than the Northern Hemisphere. At 27 kilometers, Olympus Mons is the largest volcano in the solar system. Mars has dramatic temperature differences between the seasons and the winter hemisphere develops a thick ice cap of solid carbon dioxide that is deposited from the atmosphere. A smaller ice cap containing some water ice is present year round.

Dynamically, the Martian atmosphere is more stable than the terrestrial atmosphere. Since the early 1980s (Barnes, 1980, 1981) it has been observed that the Martian atmosphere is frequently dominated by large-scale baroclinically unstable transient waves. These baroclinic transients have low wavenumbers ($m=1-3$) and near periodic 2-8 days signals which persist for more than 30 days (Barnes, 1980, 1981). In breeding experiments, Newman et al. (2004) found that after 30 sols the large-scale baroclinic mode ($m=1-2$) exhibited the most rapid sustained mean growth. A few studies have postulated that the Martian climate attractor has a relatively low dimension which leads to a more regular atmosphere than that of Earth (Martinez-Alvarado et al., 2008; Read et al., 2006). The Martian synoptic variability, it is suggested, is largely due to a few global baroclinically unstable atmospheric modes and the diurnal tide (Read et al., 2006). EOF and Fourier analyses have strengthened this theory. Fourier analysis indicates that the diurnal tide, the semi-diurnal tide, the diurnal Kelvin wave, and transient baroclinic waves are the most energetic EOFs

(Martinez-Alvarado et al., 2008). Moreover, 80% of total energy was found to be in the first 7 EOFs (Martinez-Alvarado et al., 2008).

With the increase in observational missions in the 1990s, data assimilation became a realistic option for Martian climate studies. After the Viking landers of the late 1970s, Mars exploration ceased for about two decades before the 1996 launches of the Mars Global Surveyor (MGS) and the Mars Pathfinder, which followed the failed launch of the Mars Observer in 1992. Probes have been launched with some frequency since then, with failed launches of the Mars Climate Orbiter and Mars Polar Lander in 1998, the successful Mars Odyssey in 2001, the Mars Express in 2003, the Spirit and Opportunity rovers in 2003, the Mars Reconnaissance Orbiter in 2005, and more missions planned over the next 10 years. These missions have begun to build a more complete observational data set of the Martian atmosphere, although the coverage remains relatively sparse.

The ability of data assimilation to integrate sparse data sets with general circulation models (GCMs) makes it an extremely useful tool for the Martian atmosphere. The potential benefit of data assimilation has been confirmed by a number of studies (Lewis and Read, 1995, 2003; Lewis et al., 1996, 1997; Houban, 1999) which have performed data assimilation to analyze spacecraft observations. These assimilation efforts have focused primarily on observations from the MGS spacecraft's Thermal Emission Spectrometer (TES, <http://tes.asu.edu/>). Between 1999 and 2005, during more than 25,000 polar orbits of Mars, the TES made hundreds of millions of IR radiance measurements of the Martian atmosphere with a footprint size of approximately 3x3 km. These radiances have been used to derive vertical

temperature profiles and dust opacity retrievals. In turn, these atmospheric retrievals of temperature profiles (Houben, 1999; Zhang et al., 2001) and total dust optical depth (Lewis et al., 2003) have been used in assimilation studies with varying results.

Banfield et al. (1995), one of the earliest studies, assimilated simulated observations using a Kalman filter approach with a fixed covariance matrix (which eliminates the advantage of the Kalman filter scheme). Simulated observations were also used with the analysis correction scheme of Lorenc (1988) (Lewis and Read, 1995; Lewis et al., 1996, 1997). Houban (1999) assimilated real TES temperature observations with a 4D-VAR scheme using an approximation of the tangent linear model instead of the full tangent linear model. The assimilation run was very short, but found promising analyses of the zonal mean fields. TES temperature observations were also assimilated by Zhang et al. (2001) using the steady state Kalman filter of Banfield et al. (1995). Results from this study were mixed and there was not convincing evidence that the filter was converging sufficiently.

The UK Mars data assimilation system is currently the most comprehensive system in use. Both temperature and dust opacity retrievals from the TES were assimilated by Lewis and Read (2007) using the analysis correction scheme (Lorenc, 1988), which is a modification of the successive corrections method (SCM). Assimilating these retrievals was found to benefit the atmospheric analysis during a Martian dust storm (Lewis et al., 2007). A reanalysis of the Martian atmosphere using this method currently provides the best estimate of the state of the Martian atmosphere during the MGS mission.

In these existing studies, the assimilation methods used have been less advanced as compared to the methods currently used in terrestrial atmospheric data assimilation. One of the primary challenges in Martian data assimilation is that observational data is extremely sparse. Advanced data assimilation methods, though, are better able to deal with sparse data sets and different dynamical regimes. This chapter discusses the application of the data assimilation framework of the Local Ensemble Transform Kalman Filter (LETKF) (Hunt et al., 2007) to the NASA/NOAA Mars GCM (MGCM).

NASA/NOAA Mars Global Circulation Model

The NASA/NOAA Mars Global Circulation Model originated from the GFDL SKYHI stratospheric GCM (Wilson and Hamilton, 1996) and the physics have evolved since then. The current MGCM dynamical core and coding structure is part of the Geophysical Fluid Dynamic Laboratory (GFDL) Flexible Modeling System. The NASA/NOAA MGCM utilizes finite volume (FV) numerics in the dynamical core and has a terrain following, hybrid vertical coordinate. The FV dynamical core supports two grid geometries and the latitude-longitude grid is used here. The grid is 60x36 grid points in the horizontal, which means $6^{\circ} \times 5 \frac{1}{7}^{\circ}$ resolution, with 28 vertical levels. Physical parameterizations for the MGCM are taken from the original GFDL SKYHI-based MGCM and the NASA/Ames radiation model (Wilson et al., 2008). Model forcing in these experiments come from climatology. In the remainder of this chapter, MGCM is assumed to refer to the NASA/NOAA MGCM unless otherwise specified.

Model Verification

Before developing the data assimilation code, model validation was performed using a long nature run. The model was spun up and a full Martian year was simulated with outputs every 6 hours. In the model, there are 24 hours in a Martian sol and 668.6 sols in a Martian year. After discarding the first 30 sols of spin-up time, seasonal averages were computed and compared with the TES and Oxford model results presented in the book “The Martian Climate Revisited” by Peter Read and Stephen Lewis (2004). Considering that the MGCM used here differs from the Oxford MGCM used by Read and Lewis (2004), the results agree very well. The MGCM accurately represents the major daily and seasonal features of the Martian climate. The Martian diurnal cycle is very strong, with day-night differences up to 100K, and its influence on atmospheric conditions frequently dominates that of day-to-day variability (Read and Lewis, 2004). This diurnal cycle is well modeled by the NASA/NOAA MGCM (**Fig 4.1**). As in the Earth’s atmosphere, a strong zonal wind jet develops in the winter hemisphere on Mars. The position of this feature in the summer (**Fig. 4.2a**) and winter (**Fig. 4.2b**) zonal means is also in agreement with Lewis and Read (2004).

LETKF Code Setup

The LETKF code used here is the MPI version of Dr. Eric Kostelich’s code. Since the open source code is designed for atmospheric applications, no serious numerical modifications were necessary. The code did have to be changed to support the NetCDF data structure of the MGCM output and to account for the Martian

geography. In addition, a suite of FORTRAN and Bash interface scripts was developed to run the LETKF-MGCM system.

Identical Twin Experiments

Full Coverage Experiments

To test the performance of the LETKF-MGCM system, identical twin experiments were completed. Observations were simulated by taking the year long nature run and adding random Gaussian errors with a prescribed standard deviation (1K error in temperature was used in the initial experiments). The assimilation was started from sol 10 of the nature run and assimilations were performed every 6 hours. In the results that follow, observations of temperature were assimilated at every grid point, 16 ensemble members were used, and the covariance inflation was 10%. The initial horizontal localization radius for this study was 1200km, which was selected based on the fact that observations had a radius of influence of 1200km in the assimilation study of Lewis et al. (2007). The horizontal localization is larger than the Martian deformation radius of 920km, so any Martian storms should be captured. A trapezoidal taper is used for the horizontal localization which gives weight 1 to all observations inside of 900km and then linearly decreases the weights out to 1200km. Vertical localization is set as a fraction of the atmospheric scale height and is varied by level. Due to the thinner atmosphere, the Martian scale height of 10.8km is larger than the terrestrial scale height of 7.5km. Table 4.1 shows the localization parameters that are used in the initial experiment. Experiments run with 40 ensemble members yielded nearly identical results, which emphasizes the low-order dynamics of the Martian atmosphere. No observations of winds were used, although zonal and

meridional winds were corrected by the LETKF based on the temperature observations.

The motivation for using only temperature observations is the goal of eventually assimilating real TES temperature retrievals. The TES retrievals follow the satellite track and provide an observational coverage of the Martian atmosphere which is more sporadic in space and time than the full coverage observations. (**Fig. 4.3**). Testing the performance of the analysis system with more realistic observation coverage, using simulated TES retrievals, is presented later in the chapter.

To create the initial ensemble, model states from the first 10 sols of the nature run were used. Creating the initial ensemble in this manner averages out the diurnal cycle in the initial background and leads to a very erroneous initial background state. In just one step, though, the analysis from the LETKF is able to reconstruct the spatial pattern of the diurnal cycle (**Fig. 4.4**).

<i>Levels</i>	<i>Vertical Localization</i>	<i>Horizontal Localization</i>	<i>Horizontal Taper Start</i>
28 -19	0.05	1200km	900km
18-17	0.15	1200km	900km
16-14	0.25	1200km	900km
13-9	0.35	1200km	900km
8-3	1.00	1200km	900km
2	1.50	1200km	900km
1	2.00	1200km	900km

Table 4.1 The localization parameters used at each vertical level of the MGCM for the full coverage observation experiment.

The LETKF-MGCM system was then run for 50 sol period. As a benchmark, a long integration of the model was carried out starting from the background of the very first data assimilation step. The results from this run, called the free run forecast, represent the case where no observational information is injected into the state estimation process.

The LETKF-MGCM system quickly reduces the global analysis and subsequent forecast error for both the temperature (**Fig. 4.5a**) and the zonal velocity (**Fig. 4.5b**). Upper and lower levels of the MGCM exhibit different behavior in the free run forecast based on their different dynamics. Results are shown for two levels: level 25 is near the surface and strongly affected by interactions of the atmosphere with the Martian surface; level 5 is in the free atmosphere and is characterized by a strong zonal jet. The difference between the atmospheric flow at the two levels is illustrated by showing the temperature and the zonal component of the wind at those two levels (**Fig. 4.6**).

The evolution of the root-mean-square (RMS) error in the estimates of temperature at the two model levels is shown in **Figure 4.7a** and **4.7b**. The state estimation error in the free run rapidly decreases with time in level 25, which indicates that the forcing terms play a dominant role in the evolution of the system, especially at near surface levels. More variability is seen in level 5, although both levels appear to reach a mean error between 2K and 3K. This suggests that the qualitative dynamics of the Mars GCM are more stable and similar to that of a coastal ocean model rather than to that of a terrestrial GCM. Notwithstanding the lack of

exponential growth of the root-mean-square error in the free model run, the data assimilation has a positive influence on the accuracy of the state estimate. The injection of observations with the LETKF accelerates the initial speed of the convergence and leads to a major reduction of the asymptotic value of the error in the state estimate.

There is a difference between the behavior of the estimation errors at the two vertical levels over the first 2 to 3 sols. Data assimilation leads to a quicker improvement in the lower levels and error remains relatively constant in time. In the upper atmosphere, where dynamics plays a relatively more important role compared to the forcing terms, there is more fluctuation initially before the RMS error approaches the asymptotic value at sol 5. The greater role of dynamics as opposed to forcing in the upper levels of the atmosphere can also be seen in the ensemble spread. Between level 4 and level 20, the ensemble spread collapses quickly due to the strong forcing, whereas the spread is larger in the upper 8-10 levels (**Fig 4.8**). Ensemble spread is also larger in the bottom 4 levels of the model, which is presumably due to topographic effects.

In this experiment, the largest analysis error is in the Northern Hemisphere in the lower levels. The time average of the analysis error and the temperature field shows that the largest analysis error occurs along the sharp temperature gradient around 45°N at the boundary of the polar ice cap (**Fig. 4.9**). The analysis error extends upwards in the vertical along this temperature front, which can be seen in the zonal average (**Fig. 4.10**). The analysis error is extremely low in other regions. Analysis error at around 45°N is due to the presence of strong baroclinic waves in this

region. These waves have the same horizontal and vertical signature as seen in **Fig. 4.9** and **4.10**.

This area of background error is largely captured by the ensemble spread and the values of the spread match up well with the background error (**Fig. 4.11a**). The ensemble spread is seen to be largest around 45°N and the shape of the spread is spatially similar to that of the analysis error. The average analysis error is smaller than the background error and the analysis spread has the same spatial structure as the analysis error (**Fig. 4.11b**).

Simulated TES Observations

Experiments assimilating observations at every grid point are an excellent method of studying predictability and testing the performance of the LETKF, however they do not represent the actual distribution of the TES observational data. To investigate the sensitivity of the LETKF-MGCM system to data coverage, the observational data was thinned so that it more accurately represented the spatial and temporal distribution of the TES data. At every assimilation time, the real TES observations from the previous 6 hours were read into the system and observations were simulated at the grid points closest to the real observations. In addition to this realistic horizontal distribution, a more realistic vertical distribution was used as well. The vertical profiles derived from the TES observations have 19 levels. Those levels were mapped to the nearest pressure level of the MGCM and observations were simulated at these model levels. Table 4.2 describes the average model and TES pressure levels. There are a few instances of model levels being closest to more than one TES profile level. In this case, only one observation was used at that closest

<u>Model Level</u>	<u>Model Pressure Level (mb)</u>	<u>TES Obs. Pressure Level (mb)</u>
28	7.674068	10.0572, 7.83255504
27	7.610184	
26	7.517812	
25	7.387211	
24	7.206897	
23	6.964379	
22	6.647541	
21	6.246812	6.1
20	5.758012	
19	5.185371	
18	4.543823	4.75068478
17	3.85941	3.69983702
16	3.166856	2.88143597
15	2.504267	2.24406459
14	1.906177	1.74767926
13	1.397171	1.36109398
12	0.9883192	1.06002106
11	0.6774463	0.82555, 0.64293527
10	0.4525899	0.50071849
9	0.2968393	0.38996, 0.3037
8	0.1926955	0.23652, 0.18420404
7	0.1160123	0.14346, 0.1117254
6	0.05927968	
5	0.02571784	
4	0.0100148	
3	0.003582296	
2	0.001127899	
1	0.0003546658	

Table 4.2 The pressure levels of the TES vertical profiles and closest model levels.

model level. Instead of 19 profile levels, only 14 are used in the assimilation. These levels are not evenly distributed throughout the model. The majority of the TES profile observations are concentrated in the middle of the model, with levels 7 through 18 all containing observations. The upper 6 levels have no observations and the lowest 10 levels contain only 2 observations. In practice, the distribution will be different at different points in the model because the hybrid vertical coordinate has different values at each grid point. The model pressure values in table 4.2 are shown with the values of the closest TES levels.

The experiment using full observational coverage corresponds to 57120 temperature observations at every analysis time. The more realistic TES horizontal and vertical distribution corresponds to approximately 4300 observations per analysis, although there are some analysis times with no observations. In reality, because TES observations are retrievals, they have correlated error. Here we have ignored this and instead we consider the case of larger random errors.

Because the real TES observations have a vertical distribution that leaves large gaps of model levels with no observations, if the same vertical localization is used as in the full coverage experiments then some model levels are not corrected. When this happens, it can lead to discontinuities in the analysis field and the resulting analysis is worse than the free run forecast. In order to fix this, the vertical localization radius was increased to include more vertical levels in the analysis at each point. A description of the localization used in the simulated TES observation experiments can be found in Table 4.3

<i>Levels</i>	<i>Vertical Localization</i>	<i>Horizontal Localization</i>	<i>Horizontal Taper Start</i>
28	0.05	1200km	900km
27-21	0.10	1200km	900km
20-17	0.15	1200km	900km
16-14	0.25	1200km	900km
13-9	0.35	1200km	900km
8-6	1.00	1200km	900km
5	2.50	1200km	900km
4	3.00	1200km	900km
3	4.00	1200km	900km
2	5.50	1200km	900km
1	6.50	1200km	900km

Table 4.3 The localization parameters used at each vertical level of the MGCM for the simulated TES observation experiment.

The state estimate of temperature using the simulated TES observations is worse than the analysis using observations at every grid point, although both experiments stabilize at very low error levels after 10-15 sols (**Fig. 4.12**). Having observations at every grid point leads to a quicker initial reduction of the temperature error, with the analysis error dropping below the observation error after just 1 assimilation. The state estimate with the simulated TES observations shows initial fluctuation and does not drop below the observation error until after 5 days. The state estimate of zonal velocity exhibits similar behavior (**Fig. 4.13**). There are 2 large

spikes in analysis error during the first 5 sols of the experiment with the simulated TES observations which are not seen in the full coverage experiment. After that initial period, the analysis error drops dramatically and approaches an asymptotic value between 13 and 14 sols.

One difficulty in the assimilation of real TES observations is that the observation error of the TES data is not well known and there are vertical correlations. A separate assimilation experiment was thus run using observations with an error of 3K instead of 1K. Using this data set, the analysis error still drops quickly and remains below the free run forecast error. The state estimate from the analysis using observations with larger error is worse than the analysis with more accurate observations, but both analyses exhibit similar patterns of error reduction (**Fig. 4.14**), although the temperature RMS error from the experiment using 3K observations is lower between sols 2 and 5. After sol 5, the analysis with 3K observation error is less accurate for the remainder of the run. The zonal wind RMS error using 3K observation error is worse than the analysis using observations with 1K error at every time. After stabilizing, the zonal wind analysis RMS error using 1K error observations generally remains between 0.4 and 0.6m/s, whereas the analysis RMS error using 3K error observations is between 0.8 and 1.0m/s. Larger fluctuations, with the RMS jumping to 2.0m/s at times, are seen in the analysis RMS error using 3K error observations.

The error reduction is shown for levels 5 and 25, which represent different types of dynamics—level 25 is forced by solar radiation and topography while level 5 is in the free atmosphere and has a temperature and zonal wind jet (**Fig. 4.6**). In

addition, neither level 5 nor level 25 contains simulated TES observations so all corrections come from observations at other levels. The temperature RMS error in both levels decreases below the observation RMS error, but the state estimate for level 25 is more accurate when compared to the free run forecast (**Fig. 4.15**).

Interestingly, the zonal wind analysis state estimate in both levels is worse than the free run forecast for the first 1 to 2 sols, before the analysis becomes better for the remainder of the run (**Fig. 4.16**). In level 25, the analysis and free run zonal wind RMS errors remain within 1m/s for much of the run, whereas in level 5 the analysis RMS error is more than 2m/s lower than the free run forecast RMS error.

Analysis errors are higher in the upper atmosphere using the simulated TES observation because dynamics are more important than forcing and there are no observations in the upper 6 levels. In contrast to the full coverage experiment (**Fig. 4.10**), where the dominant vertical errors were from the baroclinic waves in the lower atmosphere, the dominant analysis errors using simulated TES observations are in the zonal jet in the upper levels of the winter hemisphere (**Fig. 4.17**). The state estimate at level 25 is accurate, even in the absence of direct observations, because the forcing constrains the atmosphere in the lower levels.

Despite the presence of analysis error in the upper atmosphere in level 5, the analysis provides a superior estimate of the location and strength of the zonal jet than the free run forecast (**Fig. 4.18**). After 2 sols, the free run forecast has an incorrect location for the Northern Hemisphere zonal jet, which leads to errors of over 20m/s. In the analysis, the jet location is correct, and errors are less than 10m/s in the jet

region. Improvement in the zonal wind is also seen near the surface in level 25, but is not as dramatic as in the upper atmosphere.

Dependence on Localization

In the above experiments, neither the horizontal nor the vertical localization have been optimized. When using observations at every grid point, the abundance of observational data makes the system less sensitive to the choice of localization. The vertical localization used for the full coverage experiments allowed observations from 1 or 2 vertical levels above or below the assimilation point to be included. With fewer observations, however, the localization becomes more important. Table 4.2 showed that there are large gaps of up to 6 levels with no observational data.

Experiments in the last section showed that increasing the vertical localization radius in the upper atmosphere improves the analysis, but do the dynamics of the Martian atmosphere support this choice of localization? The thinner observations also impact the assimilation in the horizontal. In the simulated TES observation experiment, the 1200km localization radius leaves some grid points with no nearby observations (**Fig. 4.19a**). Consequently, large analysis errors can be seen in between the satellite tracks around 60° and 240° longitude in the first analysis. Subsequent passes of the satellite provides observations at these points at later analysis times, but a larger localization radius or an adaptive localization radius could allow for better use of the observational information. With a 2500km localization, for example, observations are used for the analysis at more grid points between the satellite tracks and the resulting analysis errors are reduced (**Fig. 4.19b**). The fact that Martian atmospheric

dynamics are low dimensional and are dominated by a few, predominantly baroclinic, modes with wavenumbers 1-3 could justify the use of a larger localization radius.

The ensemble correlation between points is used here to identify reasonable choices for the localization. Here, ensemble correlation refers to the pattern anomaly correlation between the ensemble perturbation values at two points. Following Hunt et al. (2007), \mathbf{X}^b was defined as the matrix of ensemble perturbations whose i^{th} column is $\mathbf{x}_n^{b(i)} - \mathbf{x}_n^b$. The ensemble correlation is then the pattern anomaly correlation between two rows of the matrix \mathbf{X}^b . Mathematically, if $\mathbf{r}_{(i,j,k)}$ and $\mathbf{r}_{(i',j',k')}$ are the rows corresponding to the grids points (i,j,k) and (i',j',k') , the ensemble correlation between these two points is given by:

$$\text{Correlation} = \frac{\langle \mathbf{r}_{(i,j,k)}, \mathbf{r}_{(i',j',k')} \rangle}{\sqrt{\langle \mathbf{r}_{(i,j,k)}, \mathbf{r}_{(i,j,k)} \rangle} \sqrt{\langle \mathbf{r}_{(i',j',k')}, \mathbf{r}_{(i',j',k')} \rangle}} \quad (4.1)$$

This idea of ensemble correlation has been used by Bishop and Hodyss (2007; 2009) as part of the ECO-RAP method of performing adaptive localization.

To get an idea of the typical correlation in the Martian atmosphere, the time average of the correlation to a single point was computed for the 50 sol assimilation run. Correlation maps calculated from experiments using different localization were found to be extremely similar, so the correlation is not sensitive to the value of the localization. Correlations are presented at three levels above the equator which represent parts of the atmosphere with different dynamics and forcing. Level 25 and Level 15 of the model both exhibit forced behavior, but level 25 has a much stronger dependence on topography. Level 5 of the model, in contrast, is in the free atmosphere.

In the longitudinal direction, the correlation with a point on the equator in the level 25 is above 0.2 for about a third of the equatorial radius or approximately 7100km (**Fig. 4.20**). A similar correlation diameter is found in level 15, along with a more circular distribution of the correlation and a dipole pattern in both the horizontal and the vertical (**Fig. 4.21**). In the upper atmosphere, the correlation diameter is much larger and stretches across all latitudes (**Fig. 4.22**). There is also a large correlation pattern in the vertical, with a dipole correlation pattern between the upper levels of the atmosphere (~ 0.01 pa) and pressure levels of approximately 1pa. The 7100km diameter found in the lower levels corresponds to a radius of 3550km, which is almost three times the 1200km radius that was initially used. In the upper levels, that 1200km radius is about a tenth of the radius of the correlation patterns which are observed.

Another experiment was run using the simulated TES observations with 3K observation error, 10% inflation, a 16 member ensemble, and a localization radius that varied with height. The localization radius was identical in the lower atmosphere and grew to 3600km at the top level of the model. The localization parameters are shown in Table 4.4. The temperature state estimate is better with the varied localization for the first sol and then the 1200km uniform localization analysis has a lower RMS error until sol 6 (**Fig. 4.23**). After sol 6, the analysis using the varied localization is better for the remainder for the simulation. While the zonal wind analysis using the 1200km uniform localization has small spikes in the error, the analysis error with the varied localization is lower and does not exhibit these fluctuations.

<i>Levels</i>	<i>Vertical Localization</i>	<i>Horizontal Localization</i>	<i>Horizontal Taper Start</i>
28	0.05	1200km	900km
27-21	0.10	1200km	900km
20-17	0.15	1200km	900km
16-14	0.25	1200km	900km
13-9	0.35	1200km	900km
8-6	1.00	2000km	1000km
5	2.50	2500km	1500km
4	3.00	3000km	2000km
3	4.00	3000km	2000km
2	5.50	3600km	2000km
1	6.50	3600km	2000km

Table 4.4 The localization parameters used at each vertical level of the MGCM for the simulated TES observation experiment with increased localization radius in the upper atmosphere.

Summary

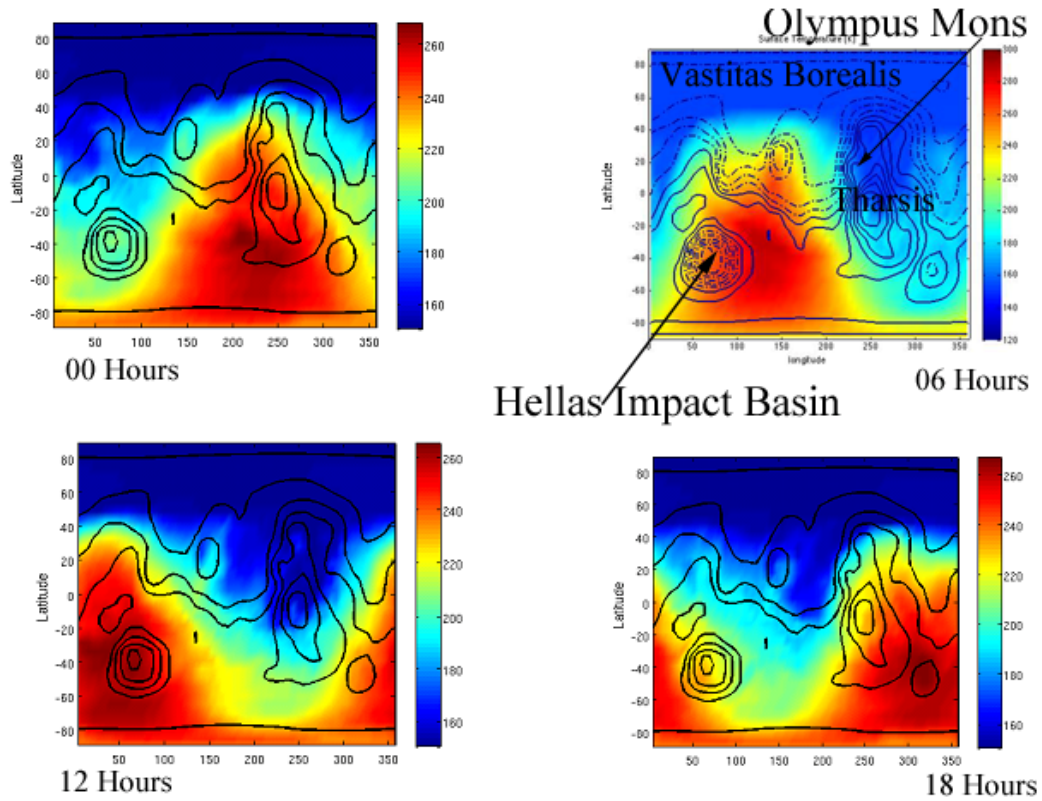
The local ensemble transform Kalman filter has been applied to the NASA/NOAA Mars general circulation model. In identical twin experiments using full observational coverage in temperature, the LETKF is found to provide a significant reduction in the RMS error of the temperature and wind fields as compared to a forecast with no data assimilation. The Martian atmospheric dynamics

are dominated by forcing at lower levels and the primary sources of analysis error are the large scale, low wavenumber baroclinic instabilities in the winter hemisphere. The atmosphere is more dynamic driven in the upper levels and characterized by a strong zonal jet which the LETKF analysis corrects, even without and zonal wind observations.

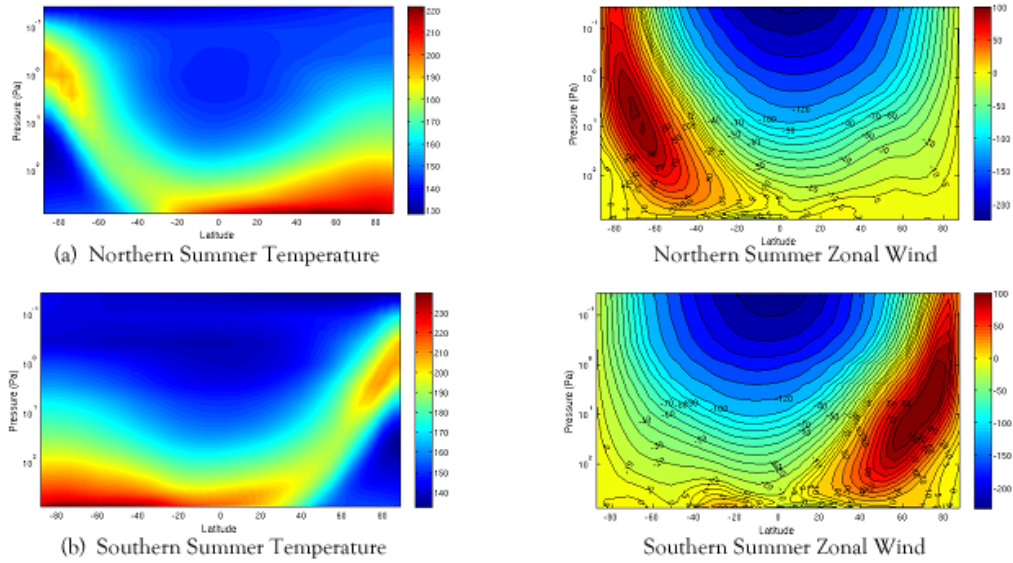
Assimilations using observations at every grid point provide a good test of the LETKF-MGCM system, but the real observational data from the TES instrument are much sparser and have vertically correlated errors. The vertical correlation in the observation errors was not accounted for in these experiments and larger random errors were used instead. To see the sensitivity of the system to the decreased observation density, observations are simulated at the grid points closest to the real TES track. The resulting analysis is a significant improvement over the free run forecast and approaches the accuracy of the full coverage analysis after approximately 15 sols. These results show that there is much potential for using the LETKF-MGCM system to produce an accurate reanalysis of the Martian climate. Because the real observations have vertically errors, a second experiment was run using an observation error of 3K as opposed to 1K. Even in the presence of larger observation error, the analysis provides an improved state estimate.

Most of the simulated TES observations are in the middle levels of the model, with no observations in the upper 6 levels. As a result, the largest analysis errors using the simulated TES observations are in the zonal jet and the upper atmosphere. Ensemble correlation was calculated in an attempt to determine a more effective localization for the upper atmosphere. The correlation patterns in the upper

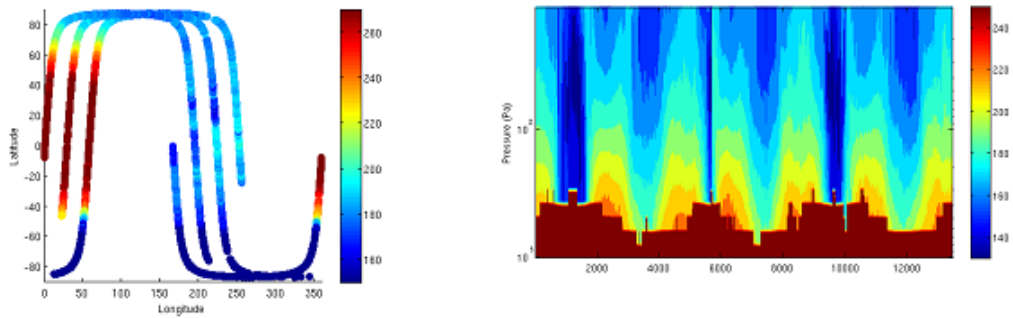
atmosphere are large scale and support the use of a larger localization radius in both the horizontal and vertical directions. An experiment using a 1200km horizontal localization radius at lower levels and expanding to 3600km at the top of the atmosphere produced a lower analysis RMS error in zonal wind after an initial stabilizing period.



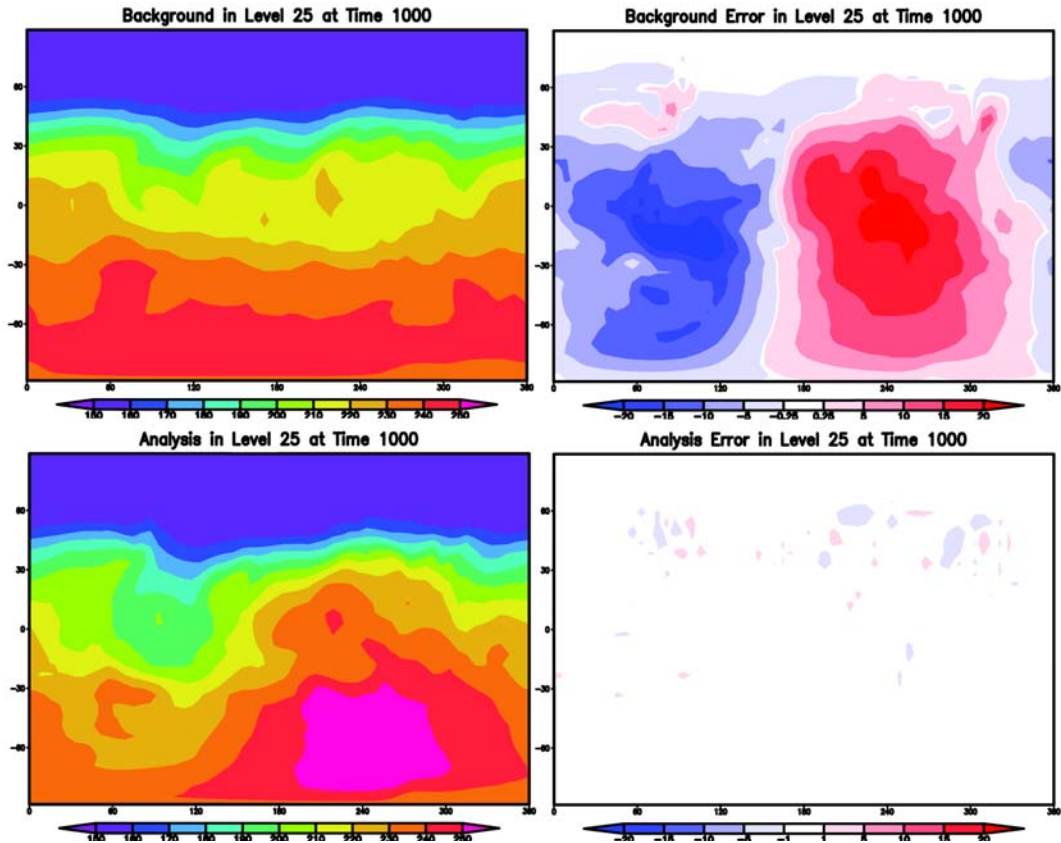
4.1 The diurnal cycle of the MGCM at the surface (Level 28). Temperature [K] is shaded and the contours represent the Martian surface topography. A few of the major features—the Hellas Basin, Olympus Mons (the largest mountain in the solar system), the lowlands of the Vastitas Borealis, and the volcanic Tharsis plateau—are labeled (top right). Courtesy of S. Greybush.



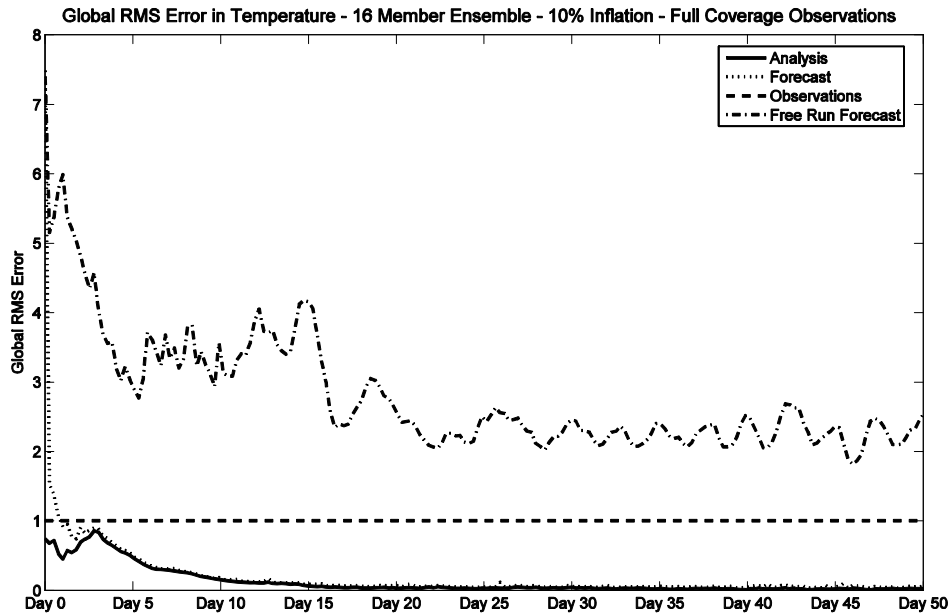
4.2 (a) The northern summer zonal mean of zonal wind shows a strong wind jet in the southern (winter) hemisphere. (b) The northern winter zonal mean of zonal wind shows a strong wind jet in the northern (winter) hemisphere. Courtesy of S. Greybush.



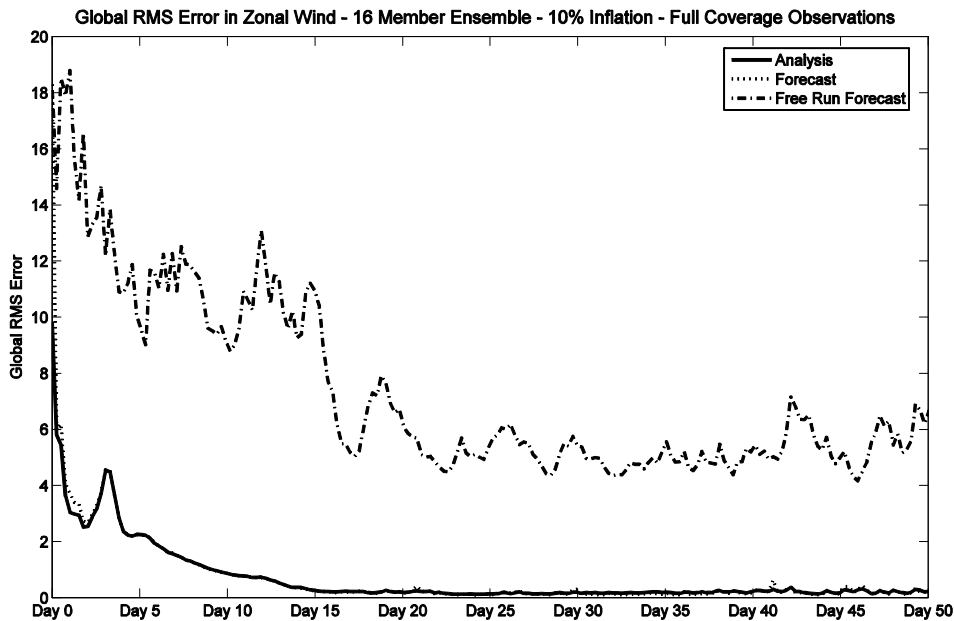
4.3 Left: TES surface temperature retrievals (K) along a few orbits corresponding to 0.25 sols. Right: TES temperature profile retrievals with the horizontal axis representing observation numbers along the orbital path. Deep red areas represent levels that are below the surface. Courtesy of S. Greybush.



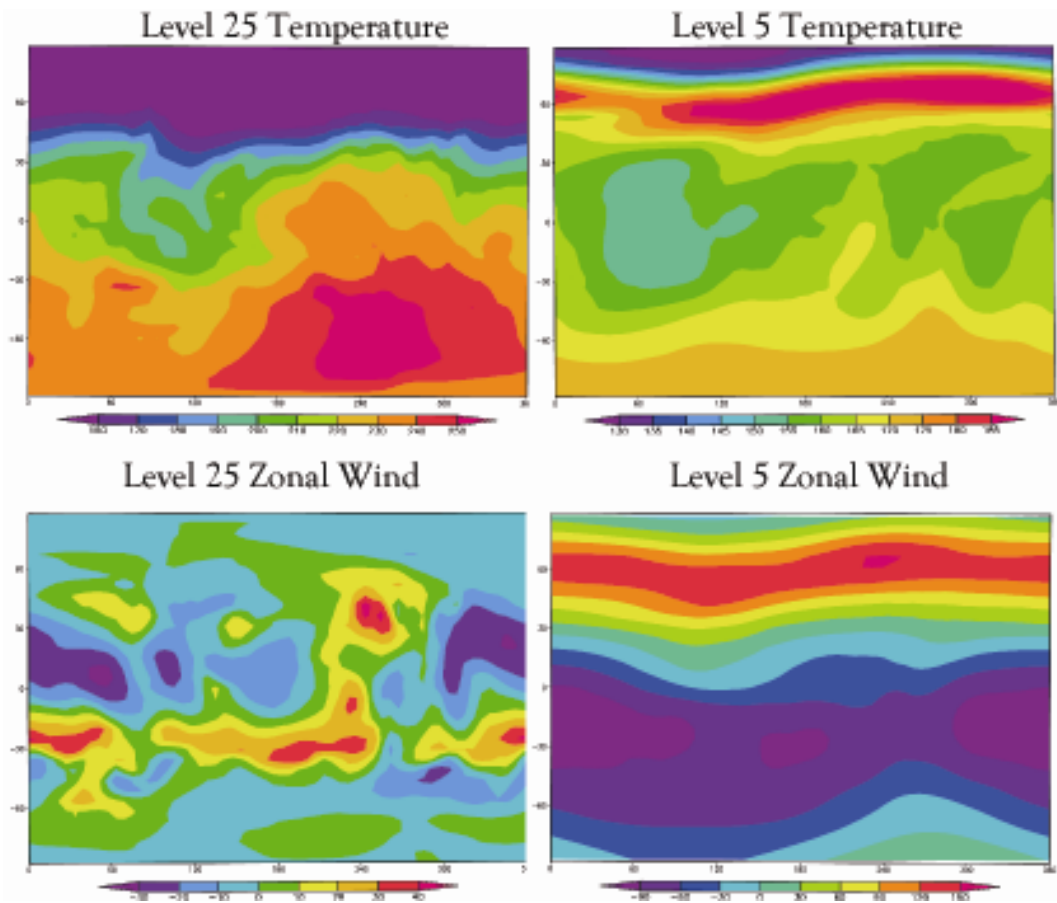
4.4 The mean of the initial ensemble surface temperature forecast (top left) has significant errors (top right), compared to the truth. The analysis ensemble mean after one step (bottom left), however, is very close to the truth and the errors almost do not show up on the same scale (bottom right).



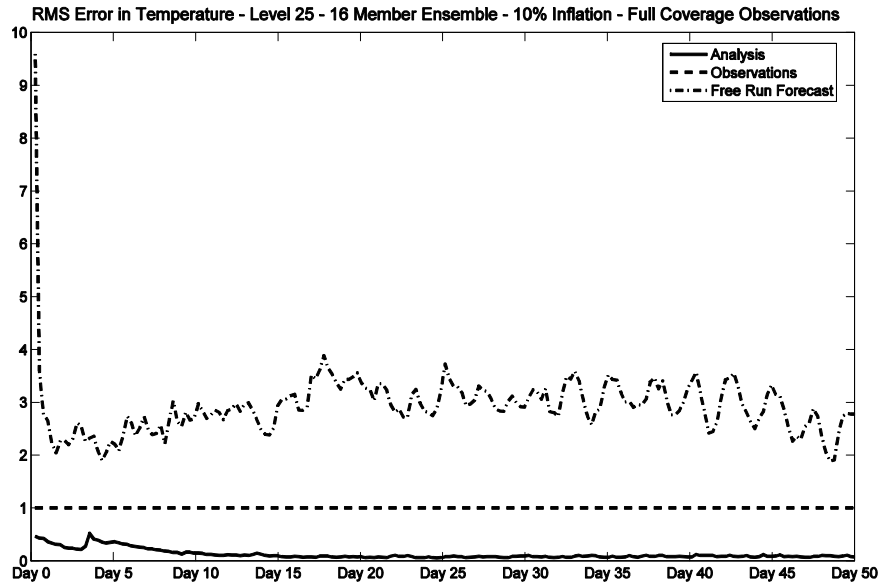
4.5 (a) The global RMS error in temperature from an identical twin experiment using observations at every grid point with observation error of 1K, a 1200km horizontal localization radius, and 10% inflation.



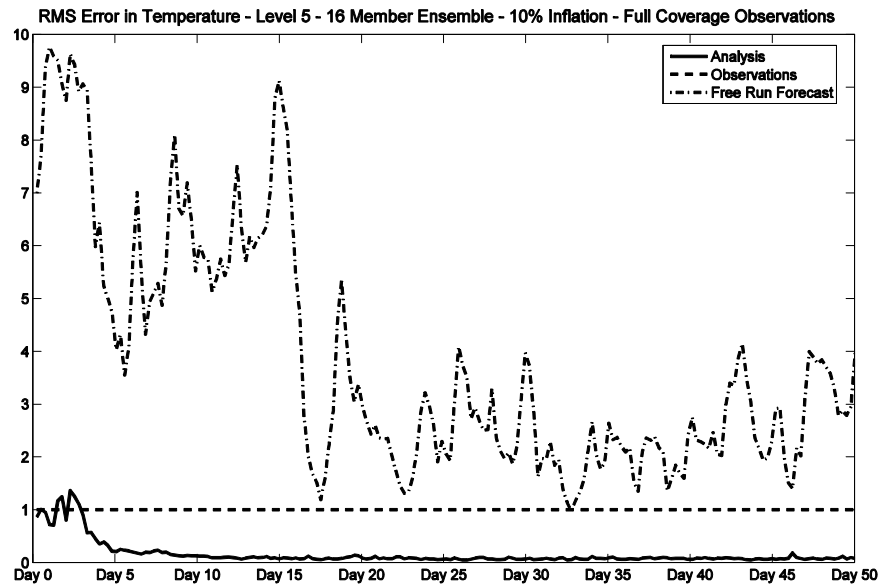
(b) The global RMS error in zonal wind of the same experiment. The analysis and forecast are improved even though no wind observations are assimilated.



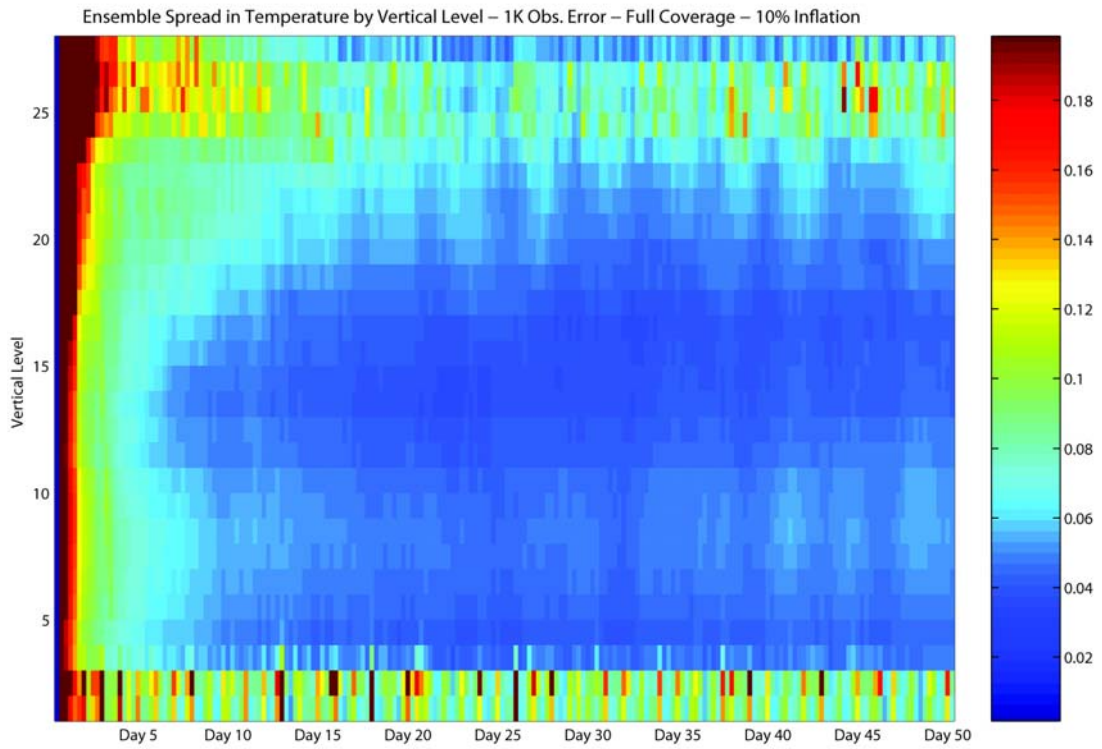
4.6 Left: The temperature and zonal component of the wind vector field at model level 25 [m/s]. Right: The temperature and zonal component of the wind vector field at model level 5 [m/s].



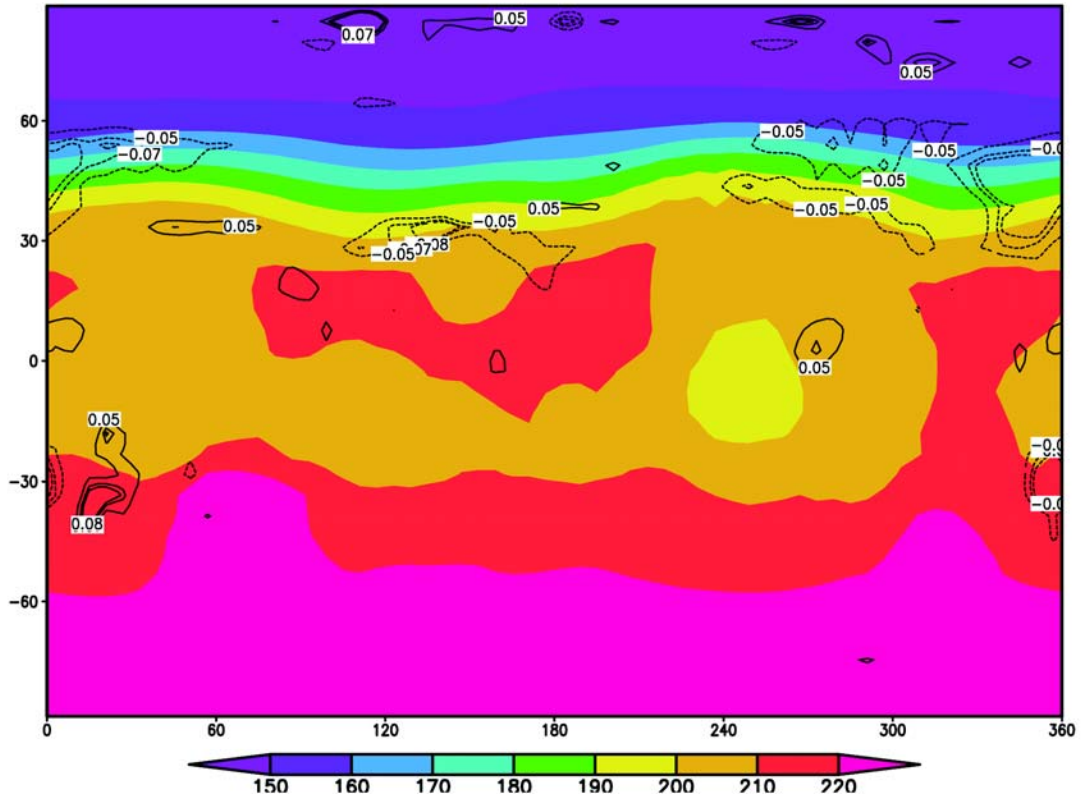
4.7 (a) Time evolution of the root-mean-square error in the estimates of the temperature [K] by the free model run and the cycled data assimilation of temperature observations at model level 25.



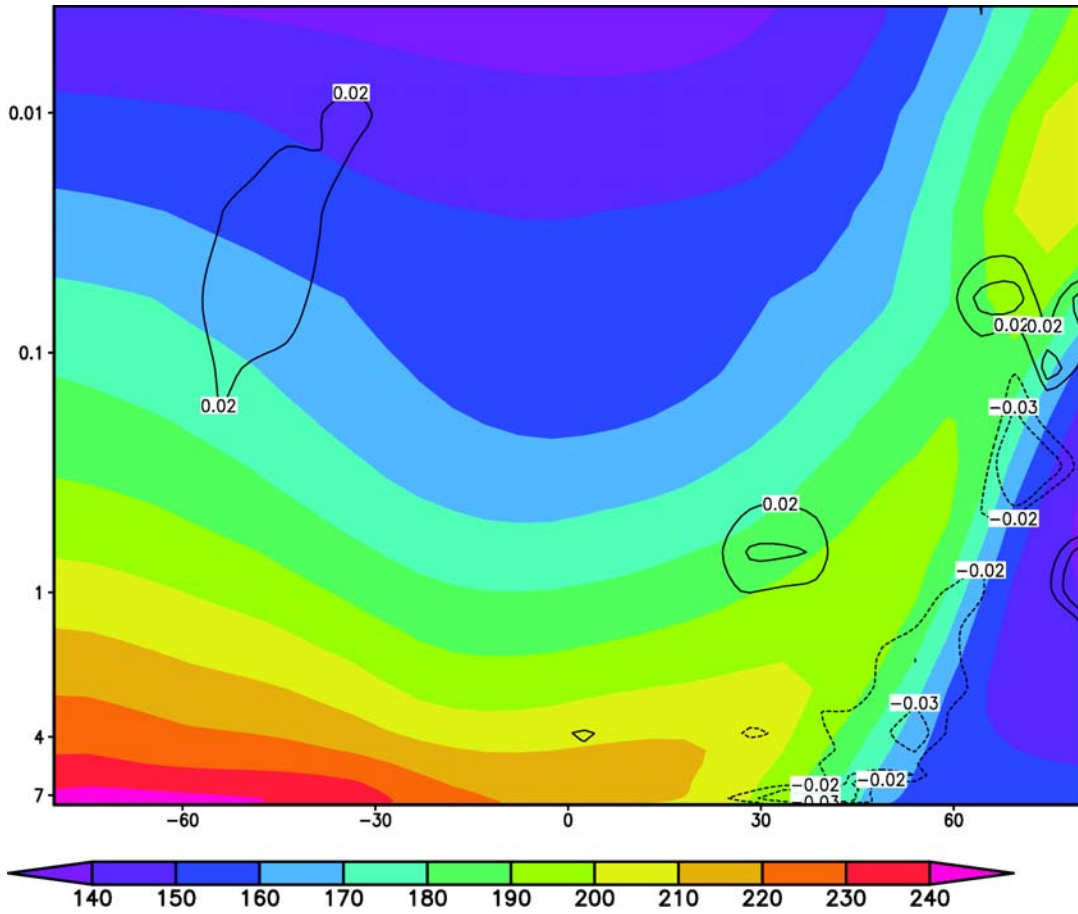
(b) Time evolution of the root-mean-square error in the estimates of the temperature [K] by the free model run and the cycled data assimilation of temperature observations at model level 5.



4.8 The ensemble spread by vertical level over a 50 sol simulation using 1K observation error, 10% inflation, 16 ensemble members, and full coverage observations.

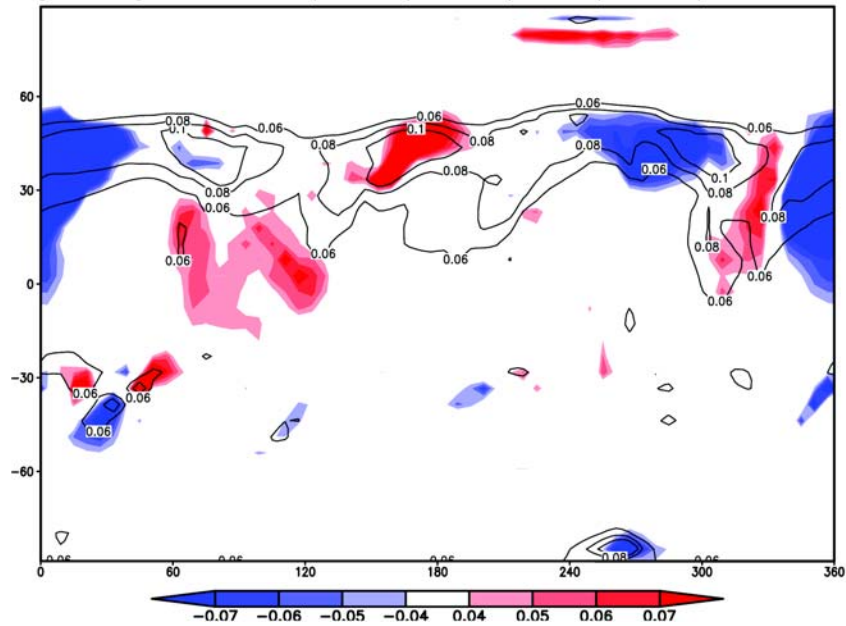


4.9 The time averaged analysis error [K] (contour) and truth temperature field [K] (shaded) at model level 17 using observations at every grid point with 1K observation error, 10% inflation, and 16 ensemble members.



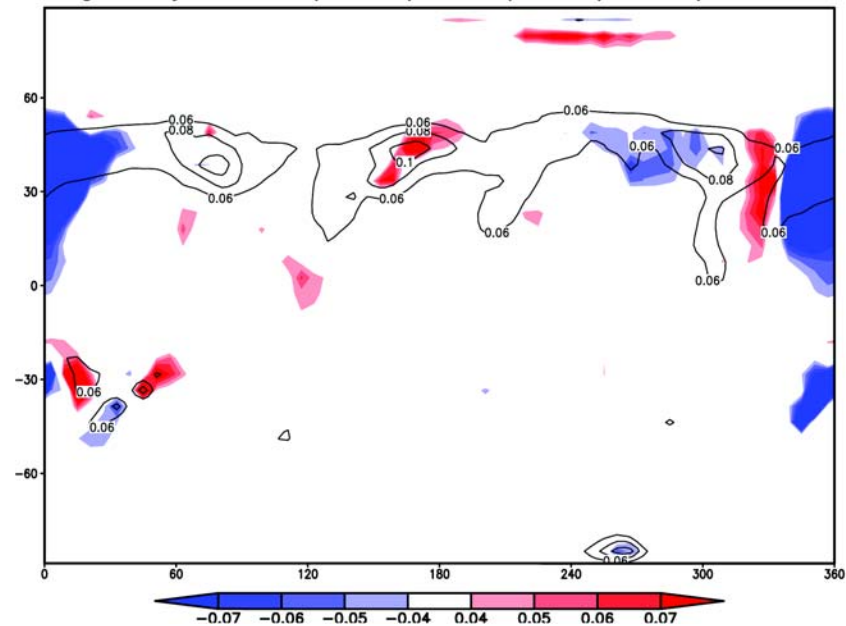
4.10 Vertical profile of the time averaged analysis error [K] (contour) and truth temperature field [K] (shaded) using observations at every grid point with 1K observation error, 10% inflation, and 16 ensemble members. The vertical axis is pressure in mb.

Avg. Background Error (shaded) and Spread (contour) at Level 25

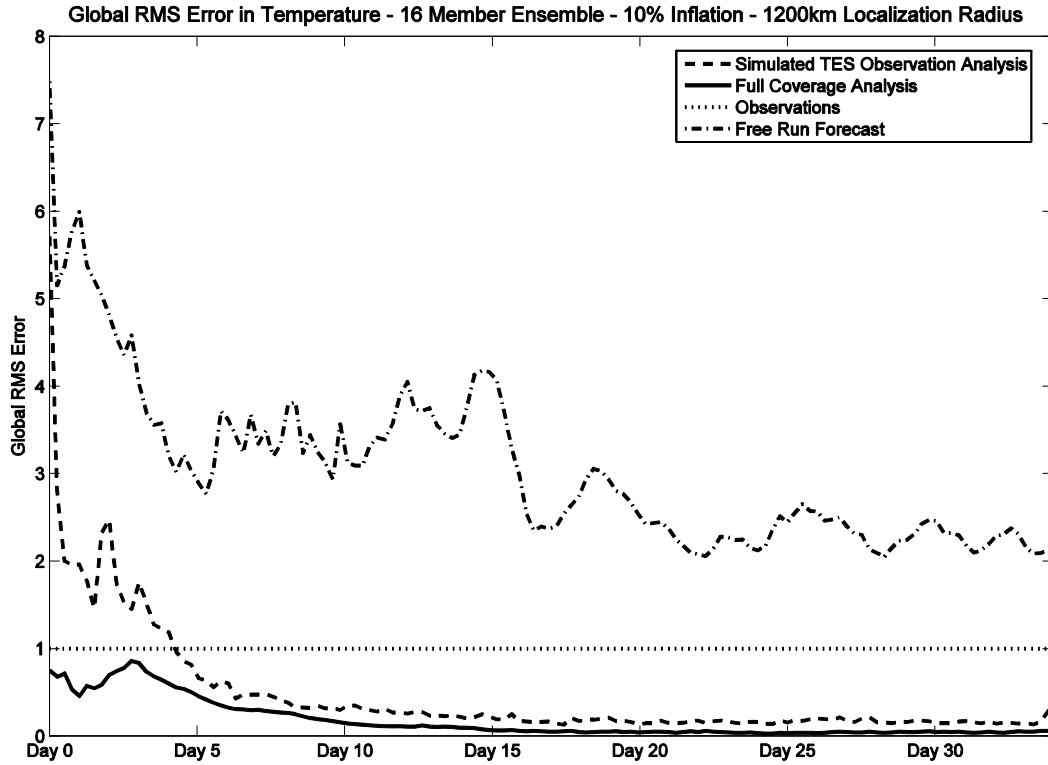


4.11 (a) Background error [K] (shaded) and background spread in temperature [K] (contour) averaged over the period from sol 2 of the simulation to sol 31 at model level 25 using observations at every grid point with 1K observation error, 10% inflation, and 16 ensemble members.

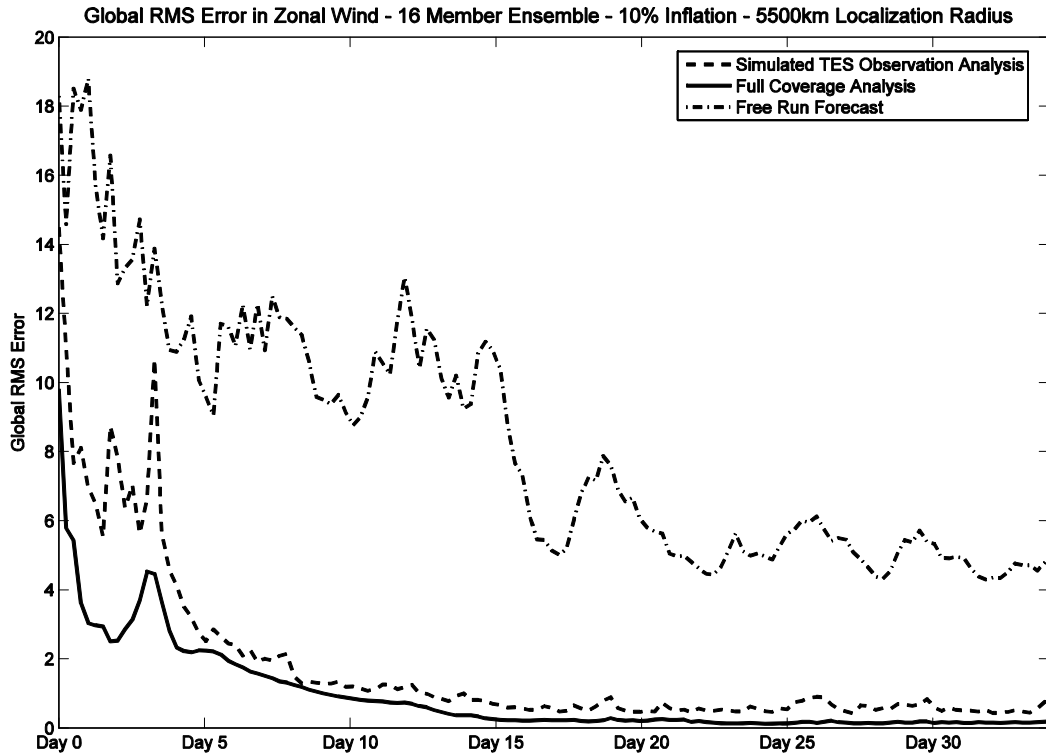
Average Analysis Error (shaded) and Spread (contour) at Level 25



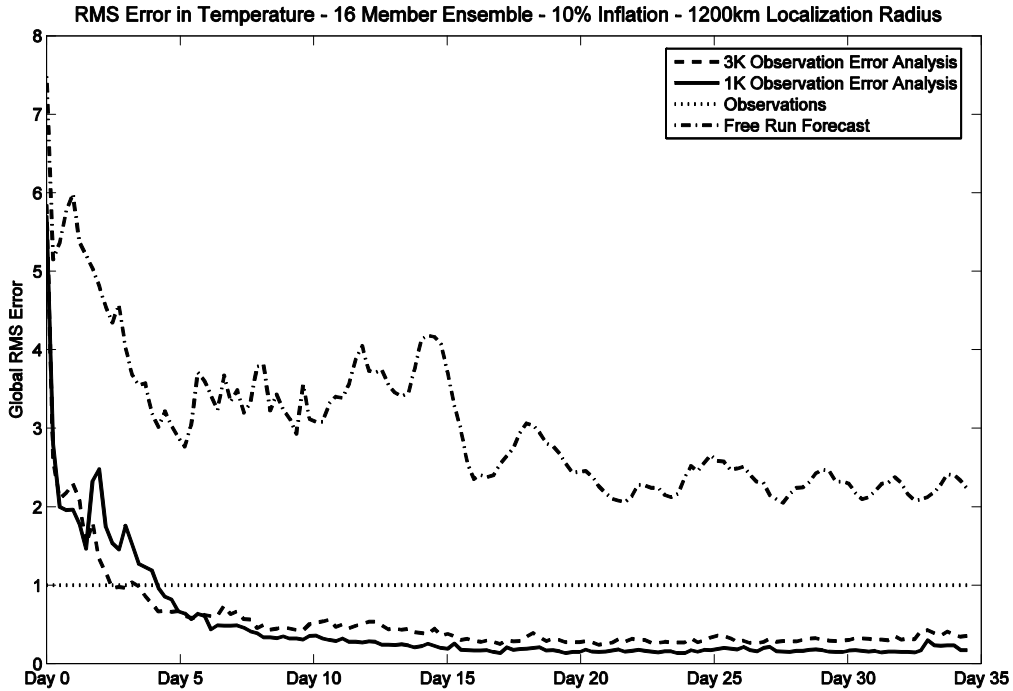
(b) Analysis error (shaded) and analysis spread (contour).



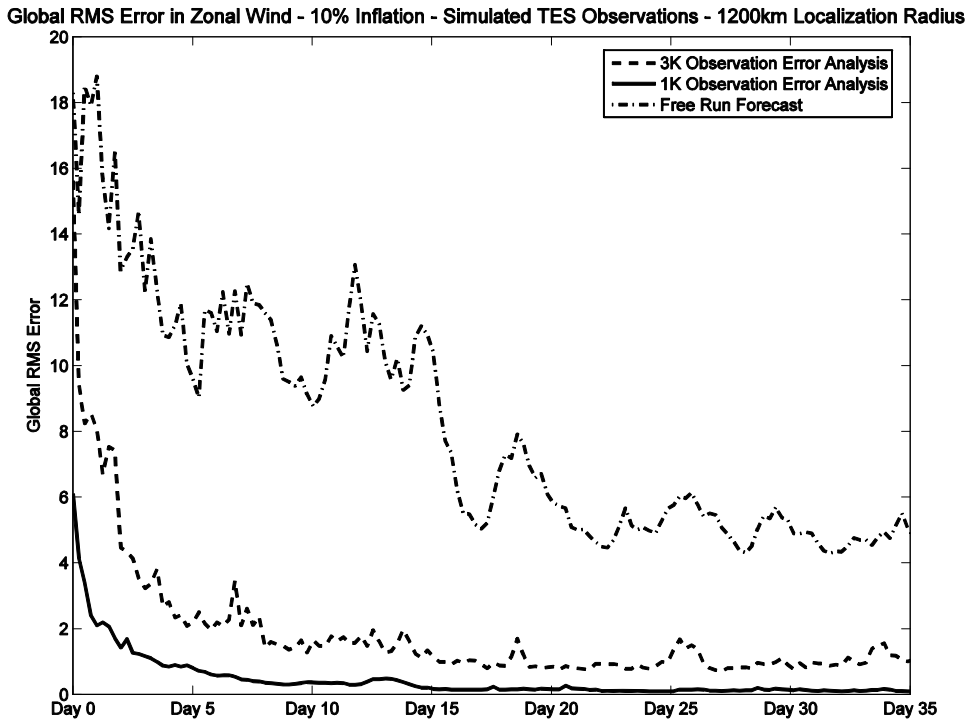
4.12 Comparison of the global RMS error in temperature using observations at every grid point and observations at simulated TES locations both only horizontally and both horizontally and vertically. A 1200km horizontal localization radius is used with an observation error of 1K and 10% inflation.



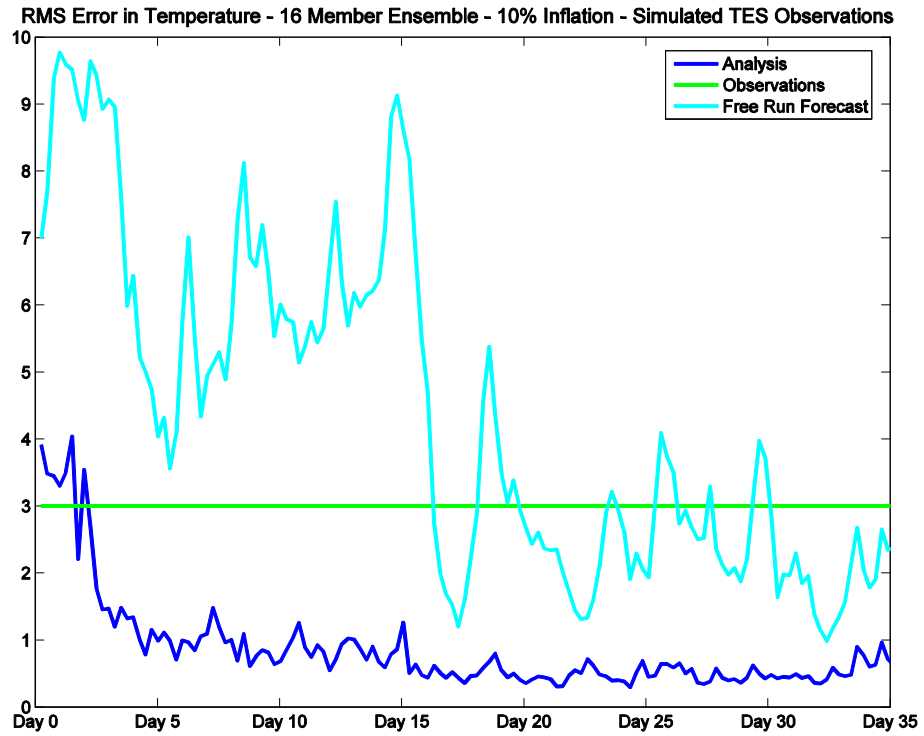
4.13 Comparison of the global RMS error in zonal wind using observations at every grid point and observations at simulated TES locations both only horizontally and both horizontally and vertically. A 1200km horizontal localization radius is used with an observation error of 1K and 10% inflation.



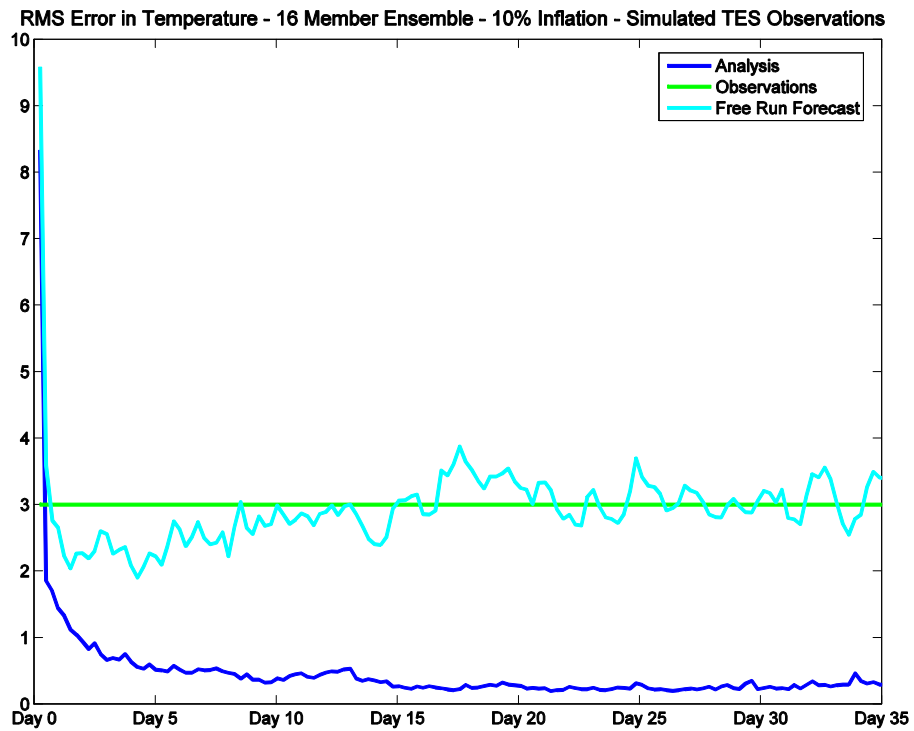
4.14 (a) Comparison of the analysis temperature RMS error from the free run, assimilation using simulated TES observations with 3K error, and assimilation using simulated TES observation with 1K observation error.



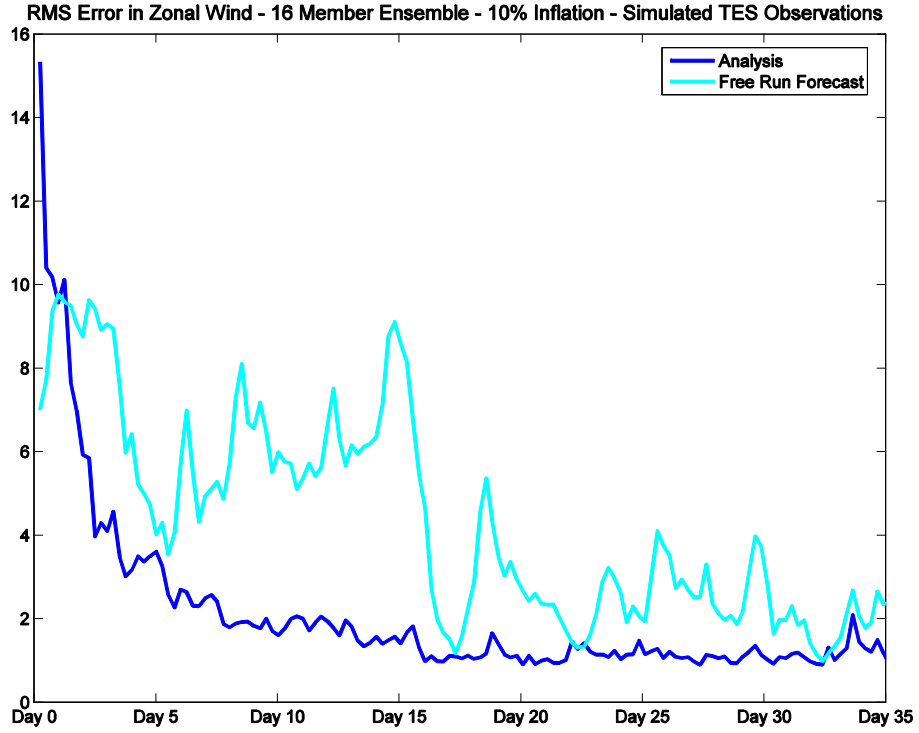
(b) Comparison in zonal wind.



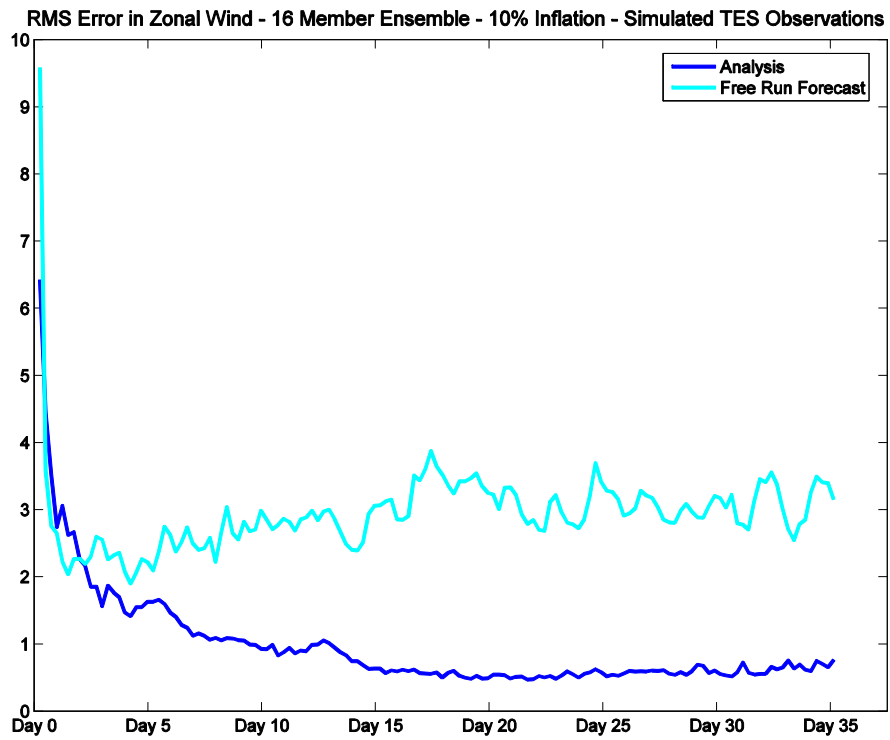
4.15 Temperature RMS error from an experiment using simulated TES observations with 3K error, 10% inflation, and a 16 member ensemble in (a) level 5



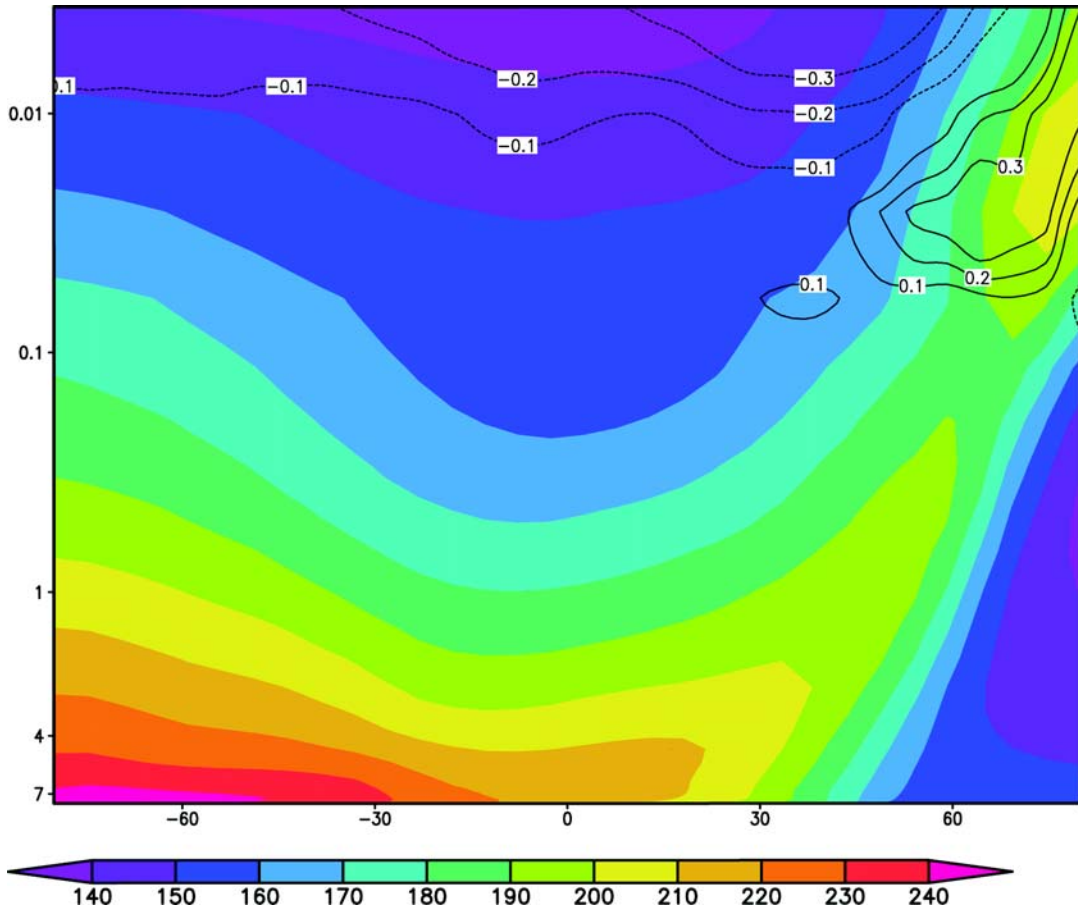
(b) level 25.



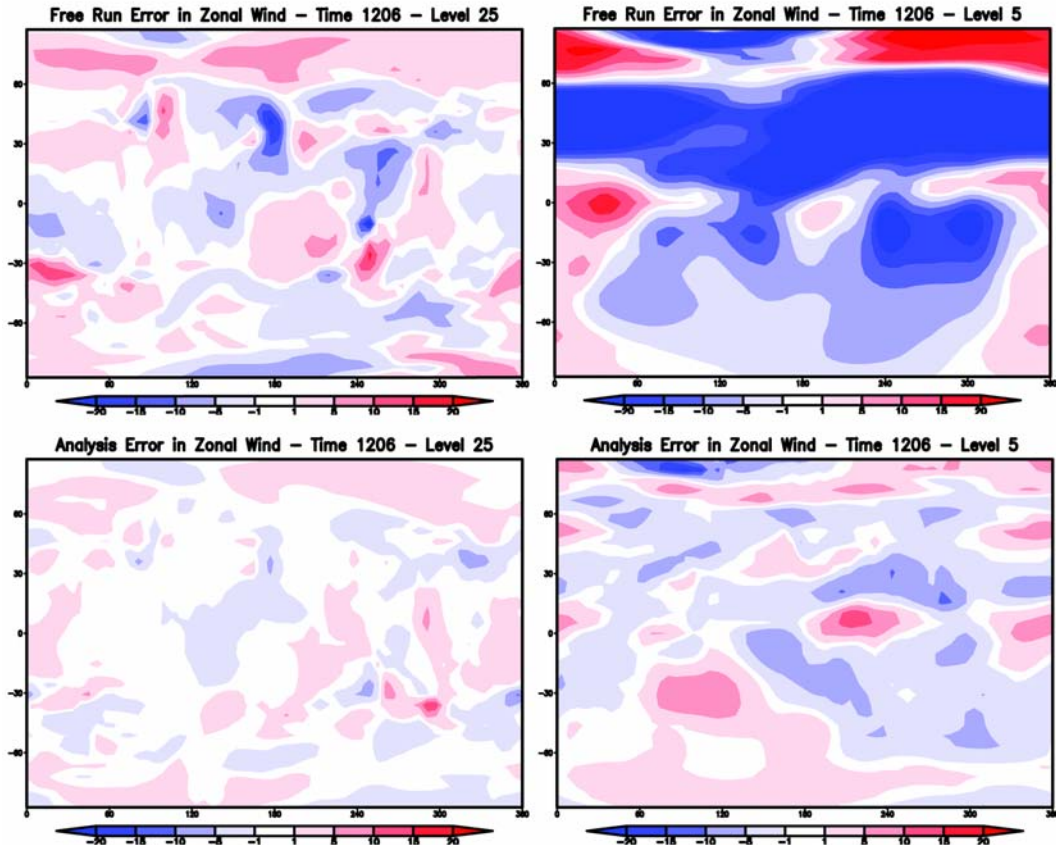
4.16 Zonal wind RMS error from an experiment using simulated TES observations with 3K error, 10% inflation, and a 16 member ensemble in (a) level 5



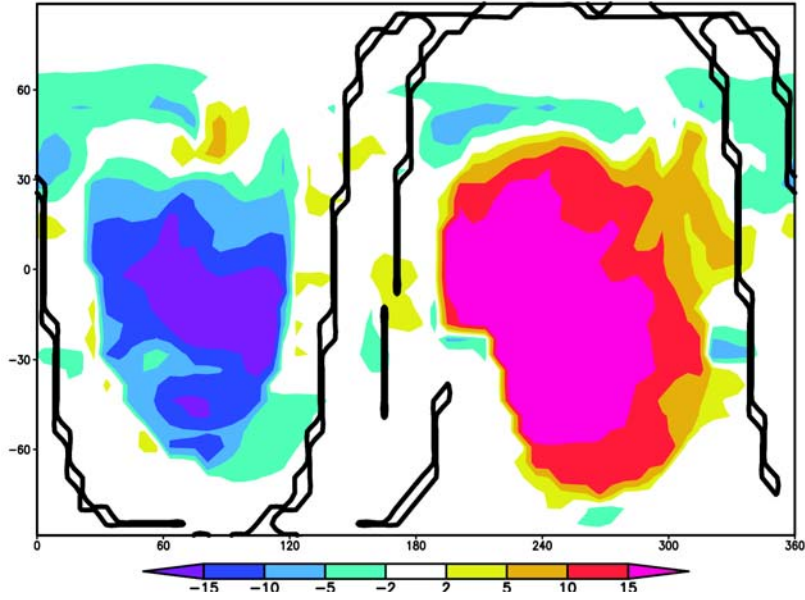
(b) level 25.



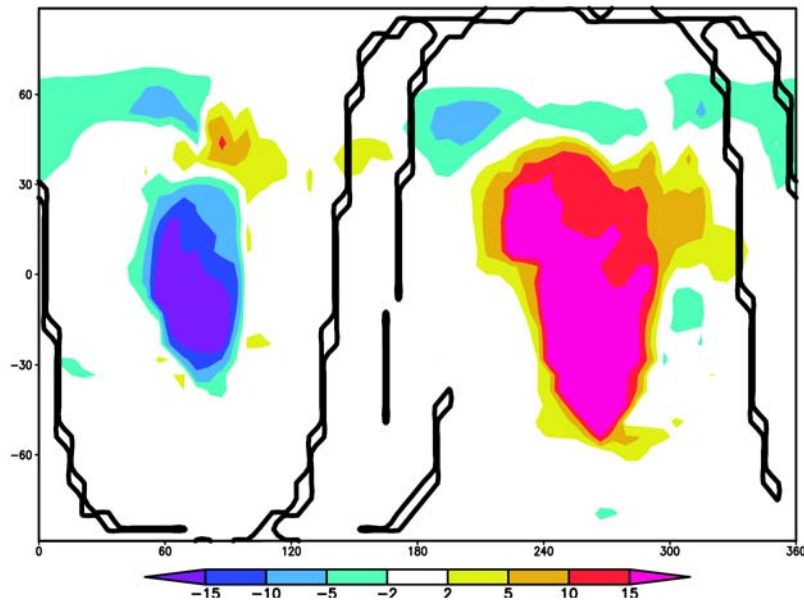
4.17 Vertical profile of the time averaged analysis error [K] (contour) and truth temperature field [K] (shaded) using simulated TES observations with 3K observation error, 10% inflation, and 16 ensemble members. The vertical axis is pressure in mb.



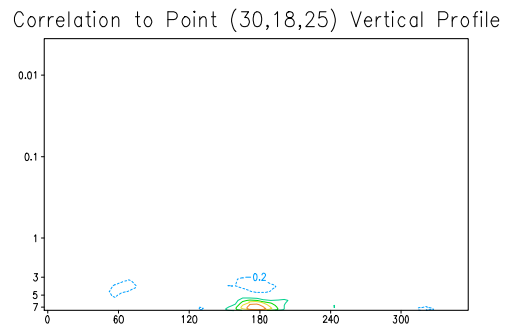
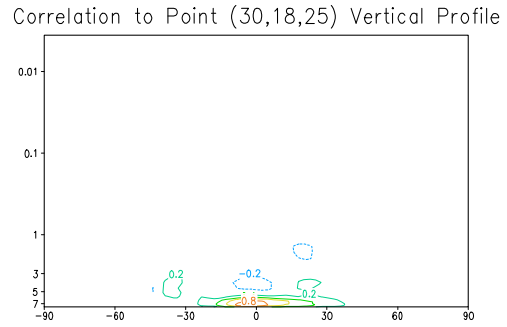
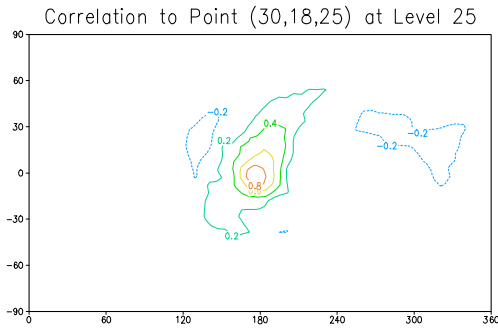
4.18 Error in the free run forecast in level 25 (top left) and level 5 (top right) and the analysis in level 25 (bottom left) and level 5 (bottom right) from sol 2, hour 6 of an experiment using simulated TES observations with error 3K, 16 ensemble members, and 10% inflation.



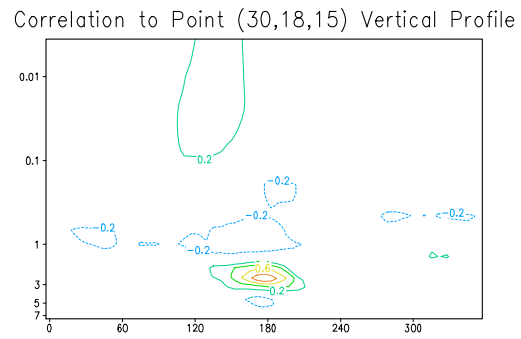
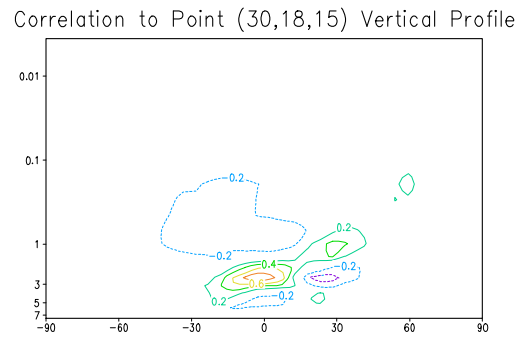
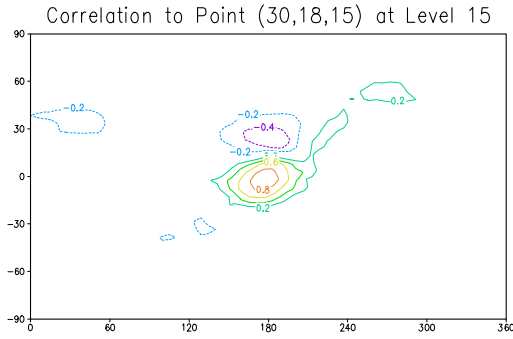
4.19 (a) The analysis error (shaded) in temperature [K] after the first analysis in level 25 of the model using simulated TES observations at all vertical levels and a 1200km localization. The contour shows the observation track.



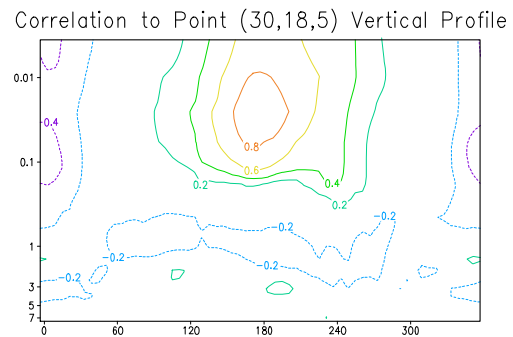
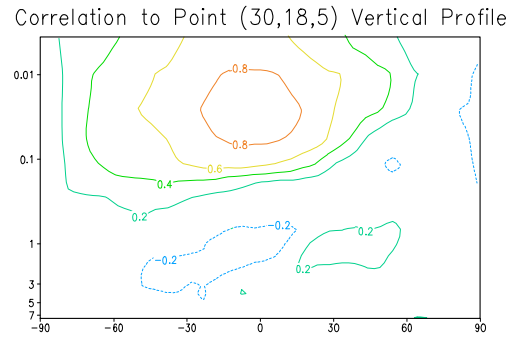
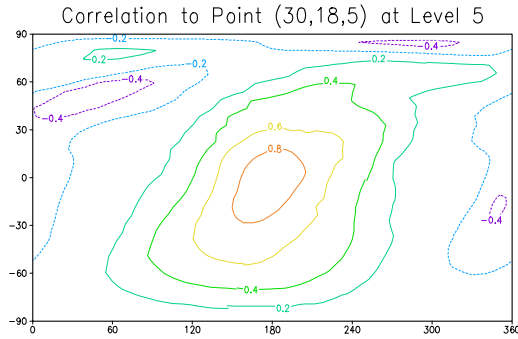
(b) The same figure but with a 2500km localization radius.



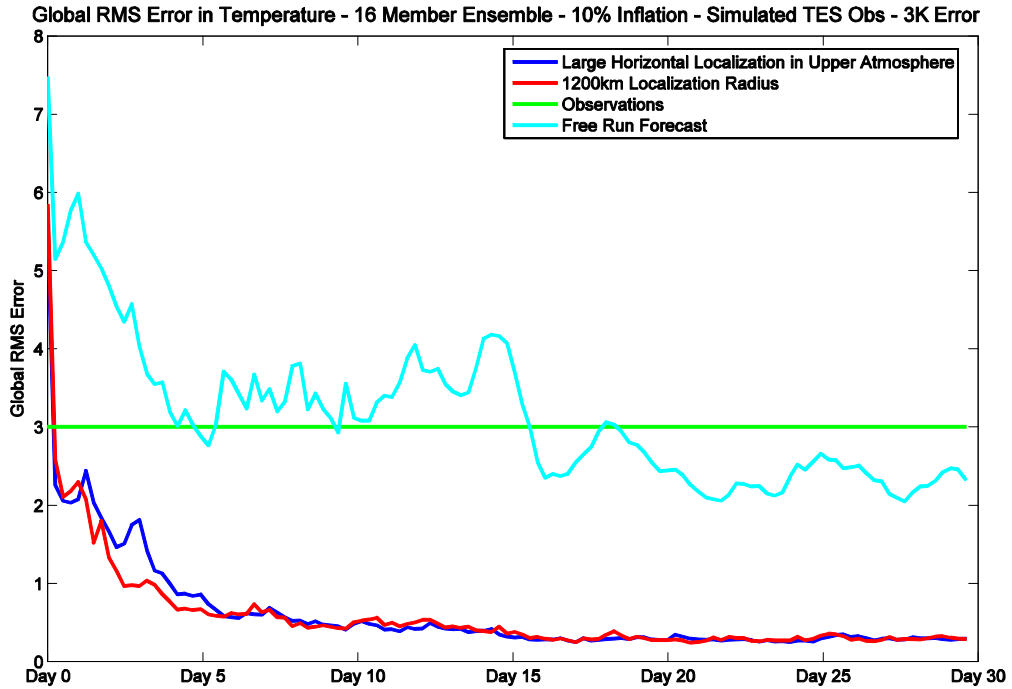
4.20 The ensemble correlation to the point (30,18,25) averaged over the final 48 sols of a 50 sol assimilation run. The correlation at level 25 (7.39mb) is shown at the top left, a cross section along $x=30$ is shown top right, and a cross section along the equator is show bottom right. The vertical axis for the cross section is pressure in mb.



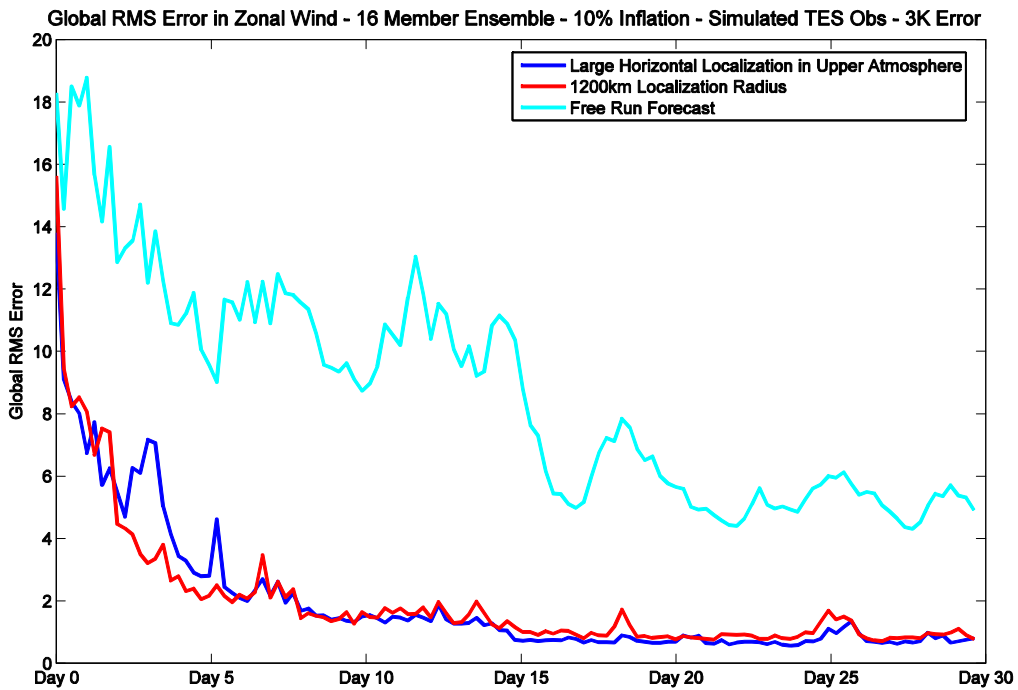
4.21 The ensemble correlation to the point (30,18,15) averaged over the final 48 sols of a 50 sol assimilation run. The correlation at level 15 (2.50mb) is shown at the top left, a cross section along $x=30$ is shown top right, and a cross section along the equator is shown bottom right. The vertical axis for the cross section is pressure in mb.



4.22 The ensemble correlation to the point (30,18,5) averaged over the final 48 sols of a 50 sol assimilation run. The correlation at level 5 (0.026mb) is shown at the top left, a cross section along $x=30$ is shown top right, and a cross section along the equator is shown bottom right. The vertical axis for the cross section is pressure in mb.



4.23 From an experiment using simulated TES observations with 3K error, 10% inflation, a 16 member ensemble, and larger horizontal localization in the upper atmosphere, (a) the global temperature RMS error



(b) Global zonal wind RMS error.

Chapter 5: Conclusion

This dissertation developed a new method of performing energy analysis using bred vectors and explored the application of the Local Ensemble Transform Kalman Filter to oceanic and planetary systems. Bred vectors identify growing instabilities in the global ocean and the bred vector energy equations developed here enable the method to diagnose the dynamical causes of the instabilities. In Chapters 3 and 4, it was demonstrated that the LETKF is an effective assimilation method for a range of complex geophysical systems. Results from the applications of the LETKF are very encouraging and suggest various possible directions for future research. A brief review of some of the main results along with future research questions are discussed here.

The breeding method was applied to a global ocean implementation of the MOM2 model forced by reanalysis winds in Chapter 2. It was demonstrated that the breeding method identifies ocean instabilities of different time scales and the bred vector energy equations were derived to calculate energetics of these instabilities. The primary area of focus in this chapter is the tropical Pacific, although instabilities are found in the tropical Atlantic Ocean and Southern Atlantic Ocean. A more thorough study of the instabilities in the Southern Atlantic, a less studied area than the tropical Pacific, will be conducted. The conversion of the baroclinic term from bred vector kinetic energy to bred vector potential energy at the surface in the western edge of the South Atlantic indicated the potential importance of surface forcing in the region.

The LETKF was interfaced with the ChesROMS model of the Chesapeake Bay in Chapter 3. Identical twin experiments with observations simulated at grid points demonstrated the ability of the LETKF to improve the state estimation in the Chesapeake. The improvement in the analysis is sensitive to the observational coverage, but significant reduction in the error of the analysis state estimate is found using a realistic number of observations. To assimilate observations at real locations, an observation operator was developed based on the interpolation used in ROMS. Assimilating temperature and salinity observations simulated at the real station locations and analysis times improves the analysis state estimate in the Bay. Because there are no observations in the open ocean, the state estimate there has larger errors.

Further exploration is needed with real observation locations and the real observations themselves. Scripts were developed to allow the real observations to be read into the system. Assimilation experiments using simulated observations in real spatial and exact temporal locations are the next step. Currently, observations are assimilated during the correct analysis window, but at the analysis time instead of the true observation time. Assimilating observations at the exact observation time necessitates switching the LETKF to run in 4D mode, as opposed to the 3D mode that it runs in now.

Quality controls will also have to be developed for the real data. Because the observations are extremely sparse, there is the potential for bad observations to cause serious damage to the analysis. The next goal is a comparison between the model and the assimilation system using the real observations. This would allow the exploration of what areas and variables of the Bay receive the most benefit from the assimilation.

The benefit of specific observations and observation systems can also be evaluated. In order judge the effectiveness of the assimilation, validation metrics must be developed. Because there are relatively few observations, one important question is determining to which independent data set the assimilation should be compared.

Assimilating real observations also introduces the need to account for model error. The behavior of the free run forecast underscores that the Chesapeake Bay is a forced system. If the forcing is imperfect, then there is the potential for all of the ensemble members to be driven to the same incorrect state, leaving the LETKF unable to make the necessary correction. The case of incorrect forcing terms will be investigated by adding errors to the forcing fields. Instead of adding random errors to the forcing, which could lead to an extremely unbalanced state, the perturbed forcing will be created by taking a weighted average of the correct forcing field and a forcing field from a randomly selected other time. Bias correction should also be added to the ChesROMS-LETKF system for using real observations.

Another part of the assimilation process that has potential for improvement is the localization. The importance of the localization was emphasized by the fact that the analysis was blowing up using observations in real locations before the localization was corrected. Currently, the localization is set in a file which is read into the assimilation code. Because the LETKF code was originally developed for use with an atmospheric model, the localization is constructed so that it can be varied by latitude and vertical level. In a coastal ocean model, however, different regions are delineated by the complex coastline and rivers systems and have no dependence on latitude nor are they regular in shape. When performing the assimilation at a point

in a river, the most important observations to use are likely those upstream of the assimilation location. In order to define a more accurate localization, a localization map will be created which will specify the localization at each point on the grid. In addition, the use of multiple localizations based on data coverage will be explored. For example, when there are only CBOS observations it may be most helpful to perform a global analysis, whereas when CBP observations become available more local patches may perform better.

Assuming an improvement is found with the assimilation, the system will be used to study the distribution and transport of dissolved oxygen and anoxia in the Chesapeake Bay. The concept of transit-time distributions, which provide a description of the transport in the flow, will be used to evaluate oxygen transport and the roles of advection and mixing in this process. The tracer prediction abilities of ROMS will also be employed to track oxygen transport and produce improved oxygen maps using the improved physical state estimates from the data assimilation. I plan to work with scientists at Johns Hopkins University, in addition to those at the University of Maryland, to complete assimilation experiments using full real observations and to calculate transit-time distributions for the purpose of evaluating the transport of oxygen.

In Chapter 4, the LETKF was coupled with the NASA/NOAA Martian GCM. Assimilation experiments with simulated observations that approximate the real TES observations showed that the LETKF is capable of correcting errors in the Martian atmosphere. The next step for the research is developing the H-operator to allow the

use of real observation locations. This would pave the way for a reanalysis of the MGS period that could be compared to the Oxford reanalysis.

Despite the obvious differences in the systems, similarities were found in the applications of the LETKF to the Chesapeake Bay and the Martian atmosphere. The most prominent similarity is the importance of forcing in both systems, which leads to an improvement in the free run forecast without data assimilation in the presence of perfect forcing. Both systems will require future work on mitigating and correcting errors in the forcing fields. Coastal ocean and planetary atmosphere systems also both have sparse observational data sets which lead to increased errors in regions with few or no observations. In the Chesapeake Bay this manifested itself in the open ocean and in the Martian model errors were largest in the upper levels of the atmosphere.

As discussed in Chapter 4, one of the biggest issues with the Martian assimilation is persistent errors along the temperature front near the surface. In this area, the ensemble spread is extremely small, which prevents adequate corrections from being made. A large percentage of the analysis error occurs in this region, so an effective method of correcting it is needed. Preliminary tests using a large multiplicative inflation coefficient have not yielded promising results, so alternative methods must be explored. One potentially useful method is the adaptive inflation method of Li et al. (2009). In this method, an estimate of the covariance inflation is derived from the ensemble spread. Estimates of the observation errors are derived simultaneously in this method, which is extremely beneficial for Mars because the observation errors in the TES observations are unknown. Unfortunately, preliminary

results using this method did not show a significant improvement in the state estimate of the MGCM. More tests are needed, however, to determine if this method can improve the Martian state estimate. Another possible avenue is the implementation of additive inflation for the LETKF. If the forced nature of the MGCM causes all of the ensemble members to converge to the same basic spatial structure, then the LETKF may not be able to correct errors in certain directions. In this case, additive inflation can restore new dynamical dimensions to the ensemble as opposed to simply artificially increasing the spread as is done in multiplicative inflation.

For the majority of the future Mars research proposed here, Steven Greybush will be the primary investigator and the research will form a significant part of his Ph.D. dissertation. However, I do intend to remain a collaborator in these efforts.

Appendix: Global Ocean Data Assimilation

Introduction

This appendix shows preliminary results achieved by the Center for Weather Forecasts and Climate Studies (CPTEC) Ocean Data Assimilation System - CODAS. This is part 1 of a continuing project at CPTEC in Brazil to develop an operational data assimilation for the global ocean based on the Local Ensemble Transform Kalman Filter method. Results were achieved between March and May 2008. During that time, the LETKF code was first interfaced with CPTEC's existing MOM4 global ocean implementation and a suite of C-Shell scripts were developed to run the system. Next, identical twin experiments were run to test the CODAS. The LETKF is found to quickly reduce the analysis and subsequent forecast error in the global MOM4-LETKF system. In addition to global corrections, the LETKF accurately captures the spatial distribution of ocean regions with very high variability. In particular, the area of the Brazil-Malvinas confluence is investigated. The analyses from the CODAS ensemble experiments using both 8 and 12 members exhibit all of the major oceanic features of the truth state. However, using twelve ensemble members, an excellent analysis, which nearly mirrors the shape of the truth, is achieved.

MOM4 Model

The LETKF framework is applied to a global implementation of the Modular Ocean Model, version 4 (MOM4) developed at GFDL. MOM4 is the newest version of the MOM used for breeding in Chapter 2 of this dissertation. Details of the model

numerics and physics can be found in Griffies et al (2004). The ocean model used here has a horizontal resolution of approximately $1^\circ \times 1^\circ$ and 50 vertical levels, with 30 of them confined to the first 1000 meters. The ocean model was spun-up for 10 years using climatological fluxes of momentum, heat and water to generate the initial restart used. During the spin up, monthly restart files were saved. To initialize the ensemble, the restart files from the months at the end of the spin up run were used.

Identical Twin Experiments

Analyses were performed every day using observations that were simulated in random locations representing a specified percentage of the entire grid. Initially, observations were simulated in all but the bottom layer of the ocean, however it was found that this led to growing errors in the bottom layers along the bottom topography. To correct this issue, observations were only simulated in the upper 35 layers of the model. This is realistic, because essentially no observation exist in the very deep ocean. In experiments using 10% data coverage, the LETKF quickly reduces both the analysis and forecast errors below the specified observational errors, which are 0.5°C , 0.08psu , and 0.04m/s for zonal velocity and 0.02m/s for meridional velocity. This reduction below the observational errors is observed in a few days for a four member ensemble and in one day for a twelve member ensemble. Moreover, the errors remain below the observational errors for the duration of the simulation. At 1% data coverage, the analysis error converges slower than at 10% coverage, but the analysis error still drops below the observational error in couple of days using a twelve member ensemble.

In addition to the global improvement, the LETKF also allows the analysis to reproduce the spatial patterns in local regions. Figures 1 and 2 show the analysis, background, and truth of meridional sea surface currents in the Brazil-Malvinas confluence, which is one of the more unstable regions of the global ocean.

In the first analysis step, the improvement from the LETKF is evident even with only eight ensemble members. The truth shows a strong, narrow tongue of northward velocity around 40°S latitude, while the background shows only weak, more dispersed velocity in the same area. After one LETKF step, the analysis exhibits a narrower area of strong velocity around 40°S that more closely resembles the truth. There is also increased southward velocity right off the coast between 30°S and 40°S which is in agreement with the truth. Moreover, after a few LETKF steps, the analysis very accurately represents the shape of the meridional velocity field in the Brazil-Malvinas confluence. Even using only four ensemble members, the analysis after a few steps shows all of the major features of the truth. Using twelve ensemble members, an excellent analysis, which nearly mirrors the shape of the truth, is achieved. Similar results are seen in all of the analysis fields.

Future work will explore the performance of CODAS using more realistically distributed observations, both spatially and temporally. Experiments exploring the predictability of the global ocean as well as studying specific instabilities will also be undertaken.

Meridional Velocity in the Brazil-Malvinas Confluence

1st Analysis Step - Jan. 1, 1969 - 8 Member Ensemble - 10% Obs. Coverage

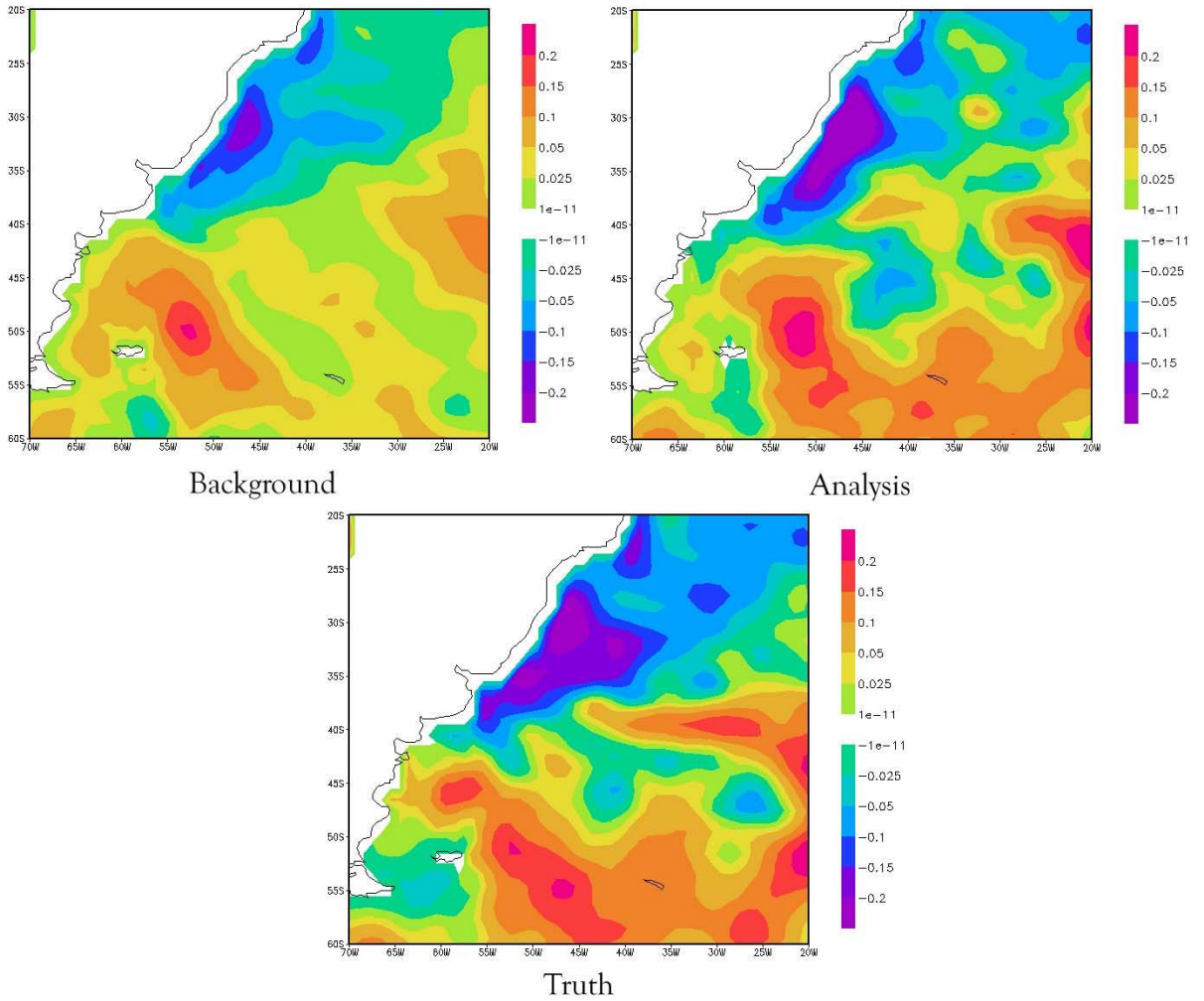


Figure A.1- Meridional velocity at Brazil-Malvinas Confluence. Panels showing the Background state, Analysis and Truth from 8 members simulations. All simulations refer to a climatological January.

Meridional Velocity in the Brazil-Malvinas Confluence 1st Analysis Step - Jan. 1, 1969 - 12 Member Ensemble - 10% Obs. Coverage

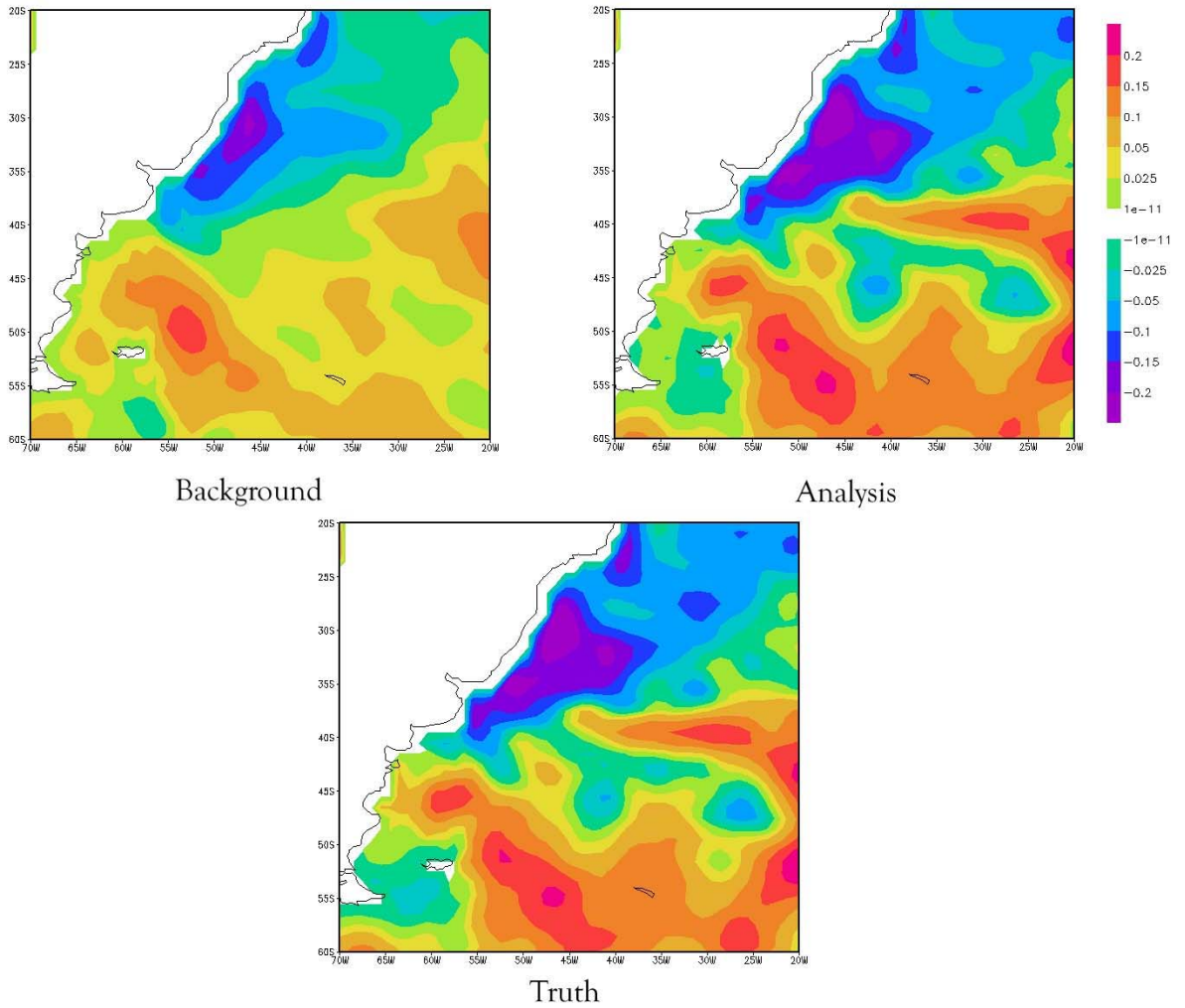


Figure A.2- Meridional velocity at Brazil-Malvinas Confluence. Panels showing the Background state, Analysis and Truth from 12 members simulations. All simulations refer to a climatological January.

Bibliography

- Banfield, D., Ingersoll, A., Keppenne, C., 1995: A steady-state Kalman filter for assimilating data from a single polar-orbiting satellite. *J. Atmos. Sci.*, **52**, 737–75
- Barnes, J. R., 1980: Time spectral analysis of mid-latitude disturbances in the Martian atmosphere. *J. Atmos. Sci.*, **37**, 2002-2015.
- Barnes, J. R., 1981: Midlatitude disturbances in the Martian atmosphere: A second Mars year. *J. Atmos. Sci.*, **38**, 225-234.
- Bishop, C. H., B. J. Etherton, and S. J. Majumdar, 2001: Adaptive Sampling with the Ensemble Transform Kalman Filter. Part I: Theoretical Aspects. *Mon. Wea. Rev.*, **129**, 420-436.
- Bishop, C. H. and D. Hodyss, 2007: Flow-adaptive moderation of spurious ensemble correlations and its use in ensemble-based data assimilation. *Q. J. R. Meteorol. Soc.*, **133**, 2029–2044.
- Bishop, C. H. and D. Hodyss, 2009: Ensemble covariances adaptively localized with ECO-RAP. Part 1: tests on simple error models. *Tellus A*, 61(1), 84-96.
- Blumberg, A. F., 1977a: On the dynamic balance of the Chesapeake Bay waters, *Chesapeake Science*, **18**, 319-323.
- Blumberg, A. F., 1977b: Numerical tidal model of Chesapeake Bay, *Journal of the Hydraulics Division*, **103**, No. HY1, 1-10.
- Carton, J.A., G.A. Chepurin, X. Cao, and B.S. Giese, 2000a: A Simple Ocean Data Assimilation Analysis of the Global Upper Ocean 1950-1995, Part 1: Methodology. *J. Phys. Oceanogr.*, **30**, 294-309.

- Carton, J.A., G.A. Chepurin, and X. Cao, 2000b: A Simple Ocean Data Assimilation Analysis of the Global Upper Ocean 1950-1995 Part 2: Results. *J. Phys. Oceanogr.*, **30**, 311-326.
- Chapman, D.C., 1985: Numerical treatment of cross-shelf open boundaries in a barotropic coastal ocean model. *J. Phys. Oceanogr.*, **15**, 1060-1075.
- Chikamoto, Y., H. Mukougawa, T. Kubota, H. Sato, A. Ito, and S. Maeda, 2007: Evidence of growing bred vector associated with the tropical interseasonal oscillation. *Geophys. Res. Lett.*, **34**, L04806, doi:10.1029/2006GL028450.
- Contreras, R. F., 2002: Long Term Observations of Tropical Instability Waves. *J. Phys. Oceanogr.*, **32**, 2715-2722.
- Cox, M., 1980: Generation and propagation of 30-day waves in a numerical model of the Pacific. *J. Phys. Oceanogr.*, **10**, 1168–1186.
- Ducet N., P.Y. Le Traon, and G. Reverdin (2000), Global high-resolution mapping of ocean circulation from TOPEX/Poseidon and ERS-1 and-2. *J. Geophys. Res.-Oceans*, **105**, 19477-19498.
- Elliott, A. J. D-P. Wang, and D. W. Pritchard, 1978: The circulation near the head of Chesapeake Bay, *J. Mar. Res.*, **36**: 643-655.
- Fana, S., L.-Y. Oeya, and P. Hamilton, 2004: Assimilation of drifter and satellite data in a model of the northeastern gulf of Mexico. *Continental Shelf Research*, **24** (9), 1001–1013.
- Flather, R.A., 1976: A tidal model of the northwest European continental shelf. *Memoires de la Societe Royale des Sciences de Liege*, **6** (10), 141-164.

- Fu, L.-L., B. Cheng, and B. Qiu, 2001: 25-day period large-scale oscillations in the Argentine Basin revealed by the TOPEX/Poseidon altimeter. *J. Phys. Oceanogr.*, **31**, 506-517.
- Fukumori, I., 2002: A partitioned Kalman filter and smoother. *Mon. Wea. Rev.*, **130** (5), 1370–1383.
- Fukumori, I. and P. Malanotte-Rizzoli, 1995: An approximate Kalman filter for ocean data assimilation: An example with an idealized Gulf Stream model. *J. Geophys. Res.*, **100** (C4), 6777–6793.
- Goodrich, D., M., William C. Boicourt, Peter Hamilton, Donald, W. Pritchard, 1987: Wind-induced destratification in Chesapeake Bay, *J. Phys. Oceanogr.*, **17**, 2232-2240.
- Guo, X. and A. Valle-Levinson, 2008: Wind effects on the lateral structure of density-driven circulation in Chesapeake Bay, *Continental Shelf Research*, **28**(17), 2450-2471.
- Guo, X. and A. Valle-Levinson, 2007: Tidal effects on estuarine circulation and outflow plume in the Chesapeake Bay, *Continental Shelf Research*, **27**, 20–42.
- Halpern, D., R. A. Knox, and D. S. Luther, 1988: Observations of 20-Day Period Meridional Current Oscillations in the Upper Ocean along the Pacific Equator. *J. Phys. Oceanogr.*, **18**, 1514-1534.
- Hicks, S. D., 1964: Tidal wave characteristics of Chesapeake Bay, *Chesapeake Science*, **5**, 103-113.
- Hoffman, R. N., R. M. Ponte, E. J. Kostelich, A. Blumberg, and I. Szunyogh, S. V. Vinogradov, J. M. Henderson, 2008: A Simulation Study Using a Local Ensemble

- Transform Kalman Filter for Data Assimilation in New York Harbor, *JAOTO*, Accepted.
- Houben, H., 1999: Assimilation of Mars Global Surveyor meteorological data. *Adv. Space Res.*, **23** (11), 1899–1902.
- Houtekamer, P.L. and H. L. Mitchell, 1998: Data assimilation using an Ensemble Kalman Filter Technique. *Mon. Wea. Rev.*, **126**, 796-811.
- Huck, T., and G.K. Vallis, 2001: Linear stability analysis of the three-dimensional thermally-driven ocean circulation : application to interdecadal oscillations. *Tellus Series A*, **53**, 526-545.
- Hunt, B. R., E. J. Kostelich, and I. Szunyogh, 2007: Efficient Data Assimilation for Spatiotemporal Chaos: a Local Ensemble Transform Kalman Filter. *Physica D*, In press.
- Jochum, M., P. Malanotte-Rizzoli, and A. Busalacchi, 2004a: Tropical instability waves in the Atlantic Ocean. *Ocean Modell.*, **7**, 145–163.
- Kalnay, E. (2004), *Atmospheric Modelling, Data Assimilation and Predictability*, Cambridge University Press, Cambridge, UK.
- Kalnay, E., et al., 1996: The NCEP/NCAR 40-year reanalysis project. *Bull. Am. Meteorol. Soc.*, **77**, 437-471.
- Legeckis, R., 1977: Long waves in eastern equatorial Pacific Ocean-View from a geostationary satellite, *Science*, **197**, 1179-1181.
- Lermusiaux, P. F. J., C.-S. Chiu, G. G. Gawarkiewicz, P. Abbot, A. R. Robinson, R. N. Miller, P. J. Haley, W. G. Leslie, S. J. Majumdar, and A. P. and F. Lekien,

- 2006: Quantifying uncertainties in ocean predictions, *Oceanography*, **19** (1), 90–103.
- Levitus, S and T. Boyer, 1994: *World Ocean Atlas 1994, Vol. 4: Temperature*, NESDIS Atlas series, NOAA, Washington, DC.
- Lewis, S. R., M. Collins, and L. Read, 1997: Data assimilation with a Martian atmospheric GCM: An example using thermal data. *Adv. Space Res.*, **19**, 1267-1270.
- Lewis, S. R., Read, P. L., 1995: An operational data assimilation scheme for the Martian atmosphere. *Adv. Space Res.*, **16**(6), 9–13.
- Lewis, S. R., Read, P. L., Conrath, B. J., Pearl, J. C., and Smith, M. D., 2007: Assimilation of thermal emission spectrometer atmospheric data during the Mars Global Surveyor aerobraking period. *Icarus*, **192**, 327-347.
- Li, M., L. Zhong and W. C. Boicourt, 2005: Simulations of Chesapeake Bay estuary: Sensitivity to turbulence mixing parameterizations and comparison with observations, *J. Geophys. Res.*, **110**, C12004, doi:10.1029/2004JC002585.
- Li, M., L. Zhong, W. C. Boicourt, S. Zhang and D.-L. Zhang, 2006: Hurricane-induced storm surges, currents and destratification in a semi-enclosed bay, *Geophys. Res. Lett.*, **33**, L02604, doi: 10.1029/2005GL024992.
- Li, M., L. Zhong, W. C. Boicourt, S. Zhang and D.-L. Zhang, 2007: Hurricane-induced destratification and restratification in a partially-mixed estuary, *J. Mar. Res.*, **65**, 169-192.

- Li, H., E. Kalnay, and T. Miyoshi, 2009: Simultaneous estimation of covariance inflation and observation errors within ensemble Kalman filter. *Q. J. R. Meteorol. Soc.*, **134**(639), 523-533.
- Liu, J., and E. Kalnay, 2007: Simple Doppler Wind Lidar adaptive observation experiments with 3D-Var and ensemble Kalman filter in a global primitive equations model. *Geophys. Res. Lett.*, **34**, L19808, doi:10.1029/2007GL030707.
- Luther, D. S., and E. S. Johnson, 1990: Eddy energetics in the upper equatorial Pacific during the Hawaii-to-Tahiti shuttle experiment. *J. Phys. Oceanogr.*, **20**, 913-944.
- Martínez-Alvarado, O., I.M. Moroz, P.L. Read, S.R. Lewis, and L. Montabone, 2008: A Diagnosis Of Low-Order Dynamics In The Atmosphere Of Mars. Third International Workshop on The Mars Atmosphere: Modeling and Observations, November 10-13, 2008 in Williamsburg, Virginia. LPI Contribution No. 1447, p.9048.
- Masina, S. and S. G. H. Philander, 1999: An analysis of tropical instability waves in a numerical model of the Pacific Ocean 1. Spatial variability of the waves. *J. Geophys. Res.*, **104**, 29613-29635.
- Masina, S., S. G. H. Philander, and A. B. G. Bush, 1999: An analysis of tropical instability waves in a numerical model of the Pacific Ocean 2. Generation and energetics of the waves. *J. Geophys. Res.*, **104**, 29637-29661.
- McCreary, J.P., and Z. Yu, 1992: Equatorial dynamics in a 2 1/2-layer model. *Prog. Oceanogr.*, **29**, 61-132.

- Mellor, G. L. and T. Ezer, 1991: A Gulf Stream model and an altimetry assimilation scheme. *J. Geophys. Res.*, **96**, 8779–8795.
- Nogués-Paegle, J., and K. C. Mo, 1997: Alternating wet and dry conditions over South America during summer. *Mon. Wea. Rev.*, **125**, 279-291.
- Oczkowski, M., I. Szunyogh, and D.J. Patil, 2005: Mechanisms for the Development of Locally Low Dimensional Atmospheric Dynamics. *J. Atmos. Sci.*, **62**, 1135-1156.
- Orlanski, I., and J. J. Katzfey, 1991: The life cycle of a cyclone wave in the Southern Hemisphere. Part I: Eddy energy budget. *J. Atmos. Sci.*, **48**, 1972-1998.
- Ott, E., B.R. Hunt, I. Szunyogh, A.V. Zimin, E.J. Kostelich, M. Kostelich, M. Corazza, T. Sauer, E. Kalnay, D.J. Patil, and J.A. Yorke, 2004: A Local Ensemble Kalman Filter for Atmospheric Data Assimilation, *Tellus*, Vol. **56A**, 415-428.
- Paraso, M. C., and A. Valle-Levinson, 1992: Meteorological influences on sea level and water temperature in the lower Chesapeake Bay, *Estuaries*, *19*, 548-561, 1996.
- Patil, D. J., B.R. Hunt, E. Kalnay, J.A. Yorke, and E. Ott, 2001: Local Low Dimensionality of Atmospheric Dynamics. *Physical Review Letters*, **86**(26), 5878-5881.
- Peña, M. and E. Kalnay, 2004: Separating fast and slow modes in coupled chaotic systems. *Nonlinear Process. Geophys.*, **11**, 319-327.
- Philander, S., 1976: Instabilities of zonal equatorial currents-Part 1. *J. Geophys. Res.*, **81**, 3725-3735.

- Pinardi, N. and A. R. Robinson, 1986: Quasigeostrophic energetics of open ocean regions. *Dynamics of Atmosphere and Oceans*, Vol. **10**(3), 185-221.
- Pritchard, D. W., 1952: Salinity distribution and circulation in the Chesapeake Bay estuarine system, *J. Mar. Res.*, **15**, 33-42.
- Pritchard, D. W., 1956: The dynamic structure of a coastal plain estuary, *J. Mar. Res.*, **15**, 33-42.
- Pritchard, D. W., 1967: Observations of circulation in coastal plain estuaries. in *Estuaries*, Publ. 83 edited by G. H. Lauff, pp. 37-44, AAAS, Washington, D. C.
- Qiao, L. and R. H. Weisberg, 1998: Tropical Instability Wave Energetics: Observations from the Tropical Instability Wave Experiment. *J. Phys. Oceanogr.*, **28**, 345-360.
- Read, P. L., S.R. Lewis, I.M. Moroz, and O. Martinez-Alvarado, 2006: Atmospheric predictability of the martian atmosphere: from low-dimensional dynamics to operational forecasting?. Second workshop on Mars atmosphere modelling and observations, February 27 - March 3, 2006 Granada, Spain, p.155.
- Shchepetkin, A.F. and J.C. McWilliams, 2005: The Regional Ocean Model System: A split-explicit, free-surface, topography-following coordinate ocean model. *Ocean Modell.*, **9**, 347-404.
- Stammer, D., C. Wunsch, R. Giering, C. Eckert, P. Heimbach, J. Marotzke, A. Adcroft, C. N. Hill, and J. Marshall, 2002: Global ocean circulation during 1992-1997, estimated from ocean observations and a general circulation model. *J. Geophys. Res.*, **107** (C9), 3118, doi:10.1029/2001JC000888.

- Toth, Z., and E. Kalnay, 1993: Ensemble Forecasting at NMC: The Generation of Perturbations. *Bull. Amer. Meteorol. Soc.*, **74**, 2317-2330.
- Toth, Z., and E. Kalnay, 1997: Ensemble Forecasting at NCEP and the Breeding Method. *Mon. Wea. Rev.*, **125**, 3297-3319.
- Valle-Levinson, A., K. Holderied, C. Li, and R. J. Chant, 2007: Subtidal flow structure at the turning region of a wide outflow plume, *J. Geophys. Res.*, **112**, C04004, doi:10.1029/2006JC003746.
- Valle-Levinson, A., C. Li, T. C. Royer, and L. P. Atkinson, 1998: Flow patterns at the Chesapeake Bay entrance, *Continental Shelf Research*, **18**(10), 1157-1177.
- Vikhliav, Y., B. Kirtman, and P. Schopf, 2007: Decadal North Pacific Bred Vectors in a Coupled GCM. *J. Clim.*, **20**, 5744–5764.
- Wang, D. P. 1978:, Non-tidal variability in the Chesapeake Bay and Potomac River: Evidence for non-local forcing, *J. Phys. Oceanogr.*, **8**, 255-232.
- Wang, D. P., 1979: Subtidal Sea Level Variations in the Chesapeake Bay and Relation to Atmospheric Forcing, *J. Phys. Oceanogr.*, **9**, 413-421.
- Wang, D. P., 1979: Wind-driven circulation in the Chesapeake Bay, Winter 1975, *J. Phys. Oceanogr.*, **9**, 564-572.
- Wang, D. P. and D. W. Kravitz: 1980, A semi-implicit two-dimensional model of estuarine circulation, *J. Phys. Oceanogr.*, **10**, 441-454.
- Wang, H. V., B. H. Johnson, 2000: Validation and application of the second generation three dimensional hydrodynamic model of Chesapeake Bay, *Water Qual. Ecosyst. Model.*, **1**, 51-90.

- Weisberg, R. H., 1984: Instability Waves Observed on the Equator in the Atlantic Ocean During 1983. *Geophys. Res. Lett.*, **11**(8), 753–756.
- Whitaker, J. S. and T. M. Hamill, 2002: Ensemble data assimilation without perturbed observations. *Mon. Wea. Rev.*, **130**, 1913-1924.
- Wunsch, C. and P. Heimbach, 2007: Practical global ocean state estimation. *Physica D*, **230**, 197–208, doi:10.1016/j.physd.2006.09.040.
- Weisberg, R. H. and T. Weingartner, 1988: Instability waves in the equatorial Atlantic Ocean. *J. Phys. Oceanogr.*, **18**, 1641–1657.
- Xu, J., W. Long, L. Lanerolle, R. R. Hood, J. D. Wiggert, T. F. Gross, R. Murtugudde, and C.W. Brown, 2009: Climate Forcing and Salinity Variability in the Chesapeake Bay, USA. *In preparation*.
- Xu, J., S.-Y. Chao, R. R. Hood, H. V. Wang, and W. C. Boicourt, 2002: Assimilating high-resolution salinity data into a model of a partially mixed estuary. *J. Geophys. Res.*, **107**(C7), 3074, doi: 10.1029/2000JC000626.
- Yang, S.-C., M. Cai, E. Kalnay, M. Rienecker, G. Yuan, and Z. Toth, 2006: ENSO bred vectors in coupled ocean-atmosphere general circulation models. *J. Clim.*, **19**, 1422-1436.
- Yang S.-C., C. Keppenne, E. Kalnay, 2008: Applications of coupled bred vectors to seasonal-to-interannual forecasting and ocean data assimilation. Submitted to *J. Clim.*
- Yu, J.-Y., and W. T. Liu, 2003: A linear relationship between ENSO intensity and tropical instability wave activity in the eastern Pacific Ocean. *Geophys. Res. Lett.*, **30**(14), 1735, doi:10.1029/2003GL017176.